Department of Precision and Microsystems Engineering

Manipulating post-buckled compliant mechanisms

Buckling mode interaction as a novel method of stiffness compensation

Armin Numić

Report no : 2021.003
Coach : T.W.A. Blad
Professor : F. van Keulen
Specialisation : MSD
Type of report : M.Sc. Thesis
Date : 22 January 2021

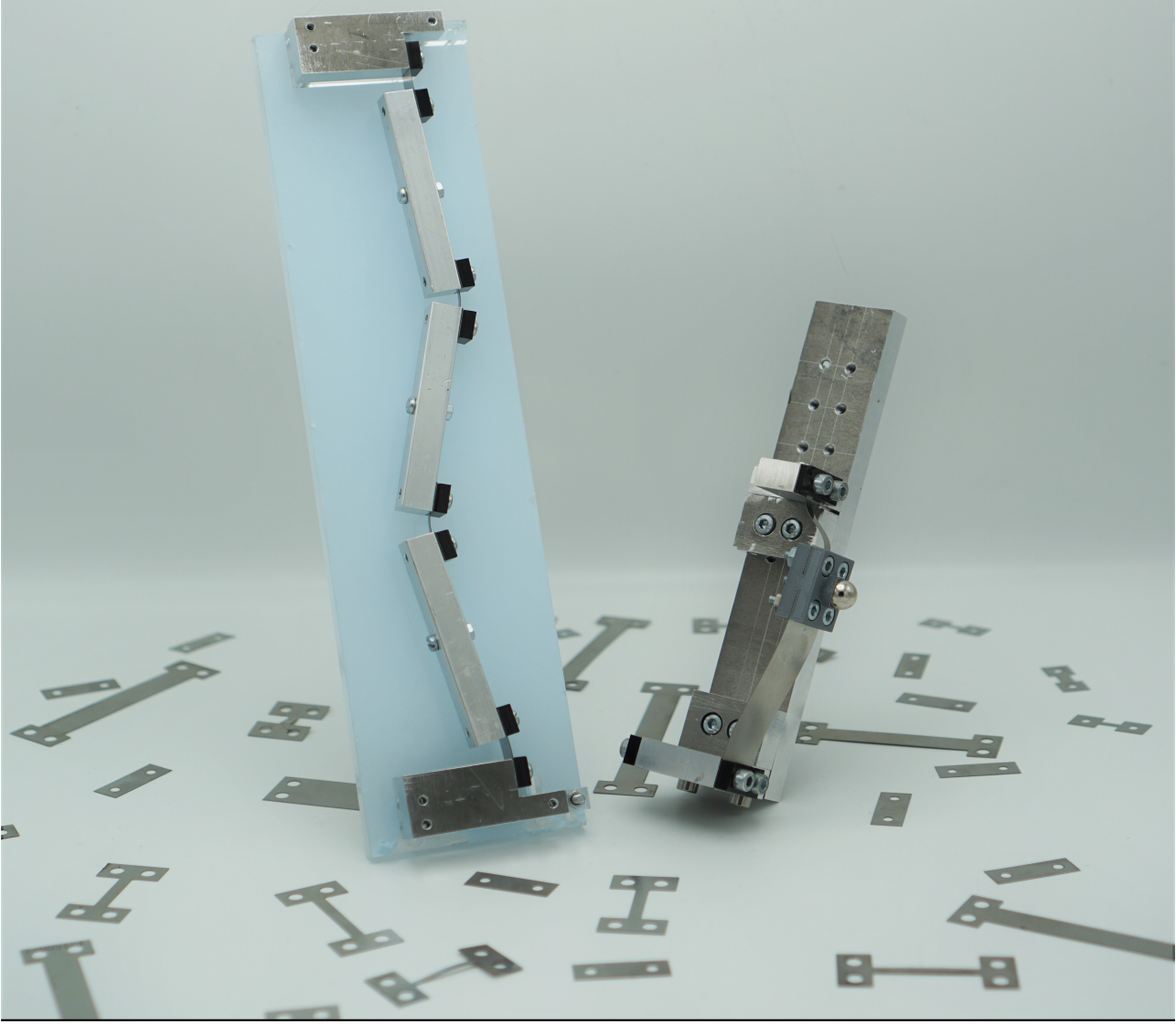

TU Delft Delft University of Technology

Challenge the future

Manipulating post-buckled compliant mechanisms

Buckling mode interaction as a novel method of stiffness compensation

M.Sc. Thesis

In partial fulfillment of the requirements for the degree of
Master of Science in Mechanical Engineering.
Department of Precision and Microsystems Engineering.
Delft University of Technology, Delft, The Netherlands.
To be defended on Friday January 22nd, 2020 at 9:00.

by

Armin Numić

born in Purmerend, The Netherlands.

Report no.	2021.003
Coach	T.W.A. Blad
Professor	F. van Keulen
Specialization	MSD
Type of report	M.Sc. Thesis
January 22,	2021

This thesis was approved by the thesis committee:

Prof. dr. ir. A. van Keulen	Chairman SOM,PME, 3mE, TU Delft
Dr. ir. R.A.J. van Ostayen	MSD, PME, 3mE, TU Delft
Ir. T.W.A. Blad	MSD, PME, 3mE, TU Delft
Dr. ir. Wu, J.	MM, SDE, IO, TU Delft

Keywords: Stiffness compensation, compliant mechanisms, buckling, vibration energy harvesting

Printed by: Repro van de Kamp

Front & Back: Stefan Molenaar

Preface

If I remember correctly, I have always wanted to be a lawyer and drive around in a big Mercedes. Yet here I am, writing the final words to my thesis in mechanical engineering. Who could have thought? Engineering has always been an obvious choice though; with two civil engineers at home, I eventually figured that the Mercedes lies perhaps a lot closer to mechanical engineering. During my bachelor graduation project, I came in touch with the concept of bistability, which has fascinated me ever since, and this only grew over time after being introduced to buckling phenomena. The thought of being able to combine this topic with development in sustainability through energy harvesting made the decision for this thesis oh-so easy.

Although I have a specific chapter to express my gratitude to everyone involved in this thesis, I would like to use this preface to focus on those most important in my life. My parents and my brother. As you will see, there is summary specially written for them in Serbo-Croatian, my native language. I would like to use that once more in this preface for a message to them. Mama, tata, Haris, mada nemam riječi za to, vama se zahvaljujem naj više na svijetu. Vi ste mi bili podrška za sve ove godine i posvećujem ovaj rad vama. Bez vas ne bih mogao ostvarit što sam do sada. Volim vas.

Armin Numić
Purmerend, December 2020

Summary

Bistable vibration energy harvesters are an interesting alternative to their linear counterparts. They allow for large amplitude oscillations between their stable equilibria, from which much energy can be generated. However, the stable equilibria are separated by a potential energy barrier that has to be overcome. Therefore, we cannot guarantee these oscillations, and the performance advantage diminishes. As a solution to this, a novel method of stiffness compensation in compliant bistable mechanisms is explored to lower the potential barrier. This method makes use of interaction between the buckling modes. Whereas this phenomenon is most undesired in structures due to their increasing proneness to catastrophic failure, we cleverly use it to our advantage. During the deflection required for the large amplitude oscillations, a transition between these buckling modes occurs, causing the increase in potential energy. By bringing the corresponding buckling loads closer together, the transition is eased and the potential barrier is lowered. An analytical framework was set up as a fundamental test of this method. Using a discrete analytical model of a bistable buckled four-bar linkage with torsion springs, it was shown that the potential barrier can be flattened upon matching the first two critical buckling loads, resulting in static balancing. This was achieved by making two torsion springs three times stiffer with respect to the other two springs. To put theory into practice, three compliant mechanisms were designed using the ratio between the first two buckling loads. Their force-deflection characteristics were experimentally determined and it was shown that the stiffness may be tuned according to the ratio between the buckling loads. Furthermore, it was shown that in designs having the first two buckling loads equal to each other, near zero stiffness is achieved. Hence, this method is proven a successful addition to the arsenal of methods in stiffness compensation and static balancing of compliant mechanisms.

Sažetak

Transformacija energije vibracija u električnu energiju predstavlja značajan korak za budućnost u svim segmentima društva. Njena je široka dostupnost čini pogodnom zamjenom za trenutne izvore energije, odnosno baterijama, za napajanje bežičnih senzora i mobilnih uređaja. Postoji nekoliko metoda za povećanje efikasnosti i primjenljivosti vibracionih transformatora energije. Jedna od njih je i upotreba bistabilnih mehanizama. Bistalibni mehanizmi su zanimljiva alternativa linearnim mehanizmima. Bistabilni mehanizmi omogućavaju velike amplitudne oscilacije između njihovih stabilnih ravnoteža, iz kojih se može proizvesti mnogo energije. Međutim, stabilne ravnoteže odvojene su potencijalnom energetskom barijerom koja sprečava ove oscilacije, i koju dakle treba prevladati. Dakle, ne možemo garantirati ove oscilacije, što rezultira u smanjenje proizvodene energije. Kao rješenje za to, tj. da se smanji potencijalna barijera, se u ovom projektu istraživa nova metoda kompenzacije krutosti u gipkim bistabilnim mehanizmima. Ova metoda koristi interakciju između načina izvijanja u bistabilnim mehanizmima. Iako je ovaj fenomen najnepoželjniji u građevini, mi ga koristimo u svoju korist. Tokom potrebnog otklona za velike amplitudne oscilacije, događa se prijelaz između ova dva načina izvijanja što rezultira u povećanje potencijalne energije. Približavanjem odgovarajućih izvijajućih opterećenja, ova se tranzicija olakšava i spušta se potencijalna barijera. Kao osnovni test ove metode postavljeni su analitički postupci. Korištenjem diskretnog analitičkog modela bistabilnog izvijenog klasičnog polužnog mehanizma sa četiri člana i torzijskim oprugama, pokazano je da se potencijalna barijera može izravnati nakon podudaranja prva dva kritična opterećenja izvijanja, što rezultira statičkim balansiranjem. To je postignuto postavljanjem krutosti vanjskih torzijskih opruga na tri puta veću krutost unutarnjih opruga. Da bi se ova teorija primijenila u praksi dizanjirana su tri modela bistabilhin gipkih mehanizama. Pri tome je korišten omjer između prva dva izvijajuća opterećenja. Eksperimentalno su utvrđene njihove karakteristike sile otklona i pokazano je da se krutost može promjeniti u skladu sa omjerom kritičnih opterećenja. Nadalje je pokazano da u mehanizmima u kojima se podudaraju prva dva izvijajuća opterećenja dobivaju konstantne sile otklona sa vrijednošću blizu nule. Ova se metoda pokazala uspješnim dodatkom arsenalu metoda u kompenzaciji krutosti gipkih mehanizama.

Contents

Chapter 1
Introduction

In this chapter, an introduction to the overarching subject of this thesis, energy harvesting, is given. Starting from energy harvesting in general and giving several examples, the text narrows down to the scope of this research. An overview of performance enhancing techniques in vibration energy harvesting is presented as an introduction to the problem statement and the research goal. Finally, the structure of this thesis is given, with an elaboration of the contents of each chapter.

1

1.1 Energy harvesting

For our society to function every single day, energy, especially electrical, is a fundamental requirement. At present, the majority of this energy is obtained through the combustion of fossil fuels. However, significant steps in the direction of renewable energy - for instance, hydro, wind and solar - have been made. This process of deriving energy from ambient sources and converting to electrical energy is named energy harvesting. Other examples are geothermal plants, which use the earth's heat to heat a working fluid powering a generator, or the combustion of biomass. Although numerous energy harvesting applications exist, the majority of portable devices still rely on batteries as an energy source. Using batteries has two great downsides.

- **Economical impact**: the lifetime of battery-powered devices exceeds that of the batteries, resulting in required maintenance/replacement. Apart from the downtime, maintenance costs are the most contributing factor [1].

- **Environmental impact**: from 2012 to 2018, the collection percentage of sold batteries has risen from 35.2% to 47.6% in the European Union. Although significant, the recycling efficiency of the collected batteries is not 100%. Hence, a staggering number of trashed batteries ends up decomposing on landfills, resulting in pollution of the environment due to the toxic materials in batteries [2].

1.1.1 Applications and relevance

The main advantage of energy harvesting is that ambient sources are virtually undepletable. Additionally, they need not be sought actively, i.e. they are everywhere around us. As a result, energy harvesting lends itself as a possible alternative to batteries, to prolong their lifetime or entirely replace them. Energy harvesting has a great potential in application to wireless sensor networks. Examples are monitoring of structural health, air quality and calamities. These sensors usually have to be operational over a long span of time. On top of that, depending on the application, they are placed in remote locations. Powering using batteries is a limiting factor, as the maintenance costs are great.

Other applications may be wearable devices. A classic example is the mechanical movement in a wrist watch, which uses the swinging motion of the arm as a power source. Jogging lights may be equipped with an energy harvester to convert the runner's motion to light for visibility during night runs. In the context of wireless sensors, powering medical wearable devices with energy harvesters renders them as "plug and forget", which is favorable for devices aiding or monitoring bodily functions.

Finally, in the present steps to a more sustainable society, energy harvesters are an interesting solution. The use of energy harvesters combats the depletion of fossil fuels, and in the long run the emission of green house gases. Moreover, the unnecessary disposal of batteries and devices can be reduced.

1.1.2 Vibration energy harvesting

There is a catch to the term undepletable though. Solar energy for instance, is available with significant sunlight. However, during overcast days or inside, solar energy strongly declines. The same flaws apply to wind energy. The choice of a suitable power source

needs to be considered based on the application. However, vibration energy has proven to excel in power density and availability [3–6]. Figure 1.1 shows a schematic representation of vibration energy harvesting.

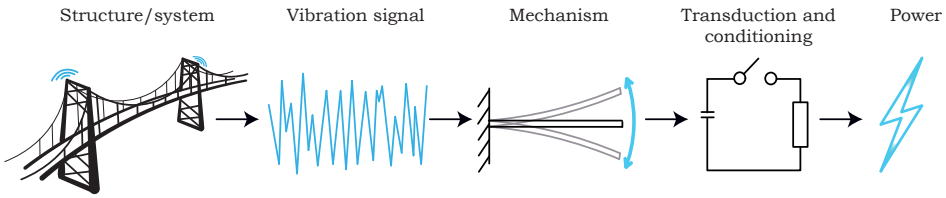

Figure 1.1: Depiction of vibration energy harvesting. A vibration signal can be obtained from any vibrating system or structure. This vibration signal is captured using an oscillating mechanism, the vibration energy harvester. For the conversion to electrical power, transduction and conditioning of the mechanism output are required.

In this case, a bridge is subjected to wind, passing traffic and possible flowing water at the pillars. The bridge stores these interactions in the form of vibrations. Reminiscing the collapse of the Tacoma Narrows Bridge, vibrations are undesired and are therefore dampened out. However, instead of dampening, vibration energy may be captured using an oscillating mechanism: the vibration energy harvester. The conversion from mechanical energy to electrical energy requires a transduction step. This transduction may be done by means of piezoelectricity, magneto- or electrostriction and electromagnetism.

1.2 Capturing energy from vibrations

In this thesis, the focus lies on the capturing of vibrations with an oscillating mechanism. Figure 1.1 presents a trivial example of a cantilever beam as the mechanism. The vibration signal is captured in the form of kinetic energy, as the mass of the cantilever is accelerated. Note the use of 'trivial' here; the cantilever can be seen as a linear mass-spring-damper system, with the resonant frequency determined by (1.1).

$$\omega = \sqrt{\frac{k}{m}} \tag{1.1}$$

Linear systems are designed such that the resonance frequency matches the frequency of the vibration signal, as this induces resonance and hence the largest oscillation amplitude. The larger the oscillation amplitude, the greater the electrical power output of the energy harvester. The oscillation amplitude strongly diminishes with a small deviation from the resonance frequency; thus, linear systems have a narrow operation bandwidth. Unfortunately, real-world vibrations rarely exhibit behavior at a single frequency, rendering linear systems ineffective in practical applications. To work with real-world vibrations, the bandwidth of energy harvesters needs to be increased. An overview of methods used for bandwidth increase is presented in Table 1.1.

Table 1.1: Selection of methods used for the increase of the energy harvester bandwidth

Method	Working principle
Duffing non-linearities	The resonance peak is bent along the frequency domain to create a broader resonance region
Bi- and multi-stability	Negative stiffness is used to create a multi-well potential and enable frequency-independent large amplitude interwell hopping
Stochastic resonance	A periodic modulating signal is applied to a double-well potential, so that interwell hopping is induced by noise
Frequency conversion	A low-frequency oscillator susceptible to broadband vibrations is coupled to a high-frequency oscillator which oscillates at the resonance frequency due to the transmission of the vibration
End-stops	End-stops limit the oscillation amplitude and increase the stiffness, shifting the resonance frequency
Multiple modes	Multiple elements with different resonance frequencies are combined in one structure to create a broader region of combined resonance peaks

Linear systems have an upright resonance peak, as seen in Figure 1.2a. By introducing a Duffing non-linearity, the resonance peak is bent along the frequency domain, creating a broader region in which resonance is obtainable. Unfortunately, this bent peak is not instantaneously accessible, as it depends on the direction of increasing or decreasing frequency. Duffing non-linearities may be introduced with the use of, for instance, magnets, axial pre-stress or coupling between material layers in the mechanism.

In Figure 1.2b, the potential curves of a linear and bistable system are presented. The linear system has a single minimum, or " potential well", rendering it monostable, while the bistable system has two wells. The two wells are separated by a peak called the potential barrier. With sufficient excitation, a large amplitude oscillation between (and beyond) the two potential wells can be obtained. This oscillation may be obtained irrespective of the vibration frequency, which means that the bandwidth is increased.

In stochastic resonance, noisy vibrations are used to induce hopping between wells in a bistable system. However, noise alone is usually not strong enough to trigger this. Therefore, an actuator is added to a bistable system, to alter the depths of the wells periodically. The combination of noise and periodic forcing can result in continuous motion between wells, and therewith harvesting broadband noise.

Frequency conversion, particularly frequency-up conversion, is used in miniaturization of vibration energy harvesters. As the scale of the system decreases, the resonance frequency increases. To be able to harvest energy at the resonance frequency, a low- and high-frequency oscillator (LFO and HFO) are coupled. The LFO, which is susceptible to broadband or low frequency vibrations, transmits the vibration to the HFO. The HFO oscillates at the resonance frequency, returning a large power output.

End-stops are used as limiters to the oscillation amplitude. This is beneficial in miniaturization and damage prevention. Additionally, upon impact of an oscillator with an end-stop, the effective length of the oscillator changes. This results in a change in stiffness and therefore a shift in eigenfrequency. This shift in frequency results in an expansion of the bandwidth.

Achieving resonance returns a large oscillation amplitude, and ultimately a large power output. The resonance region can be expanded by combining several elements with different resonance frequencies. As a result, if the vibration frequency deviates from

one resonance frequency, there are others as backup, ensuring that there still is a significant power output [7].

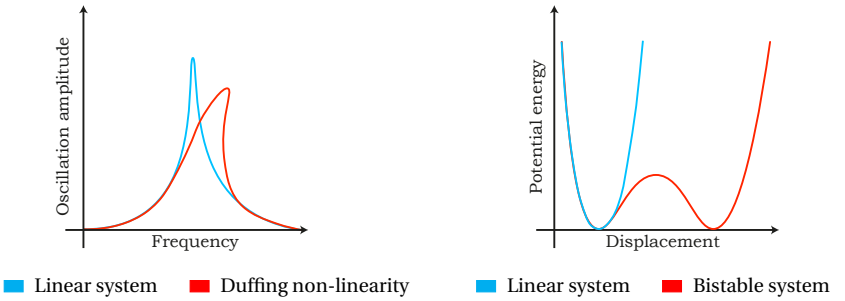

(a) Resonance peaks of linear system and system with Duffing non-linearity. The resonance peak of the Duffing system is bent along the frequency domain, creating a larger resonance region

(b) Potential energy curves of a monostable system and a bistable system. The bistable system has one unstable equilibrium at the top of the potential barrier, and two stable equilibria on either side of this barrier

Figure 1.2: Depiction of Duffing non-linearity and bistability compared to a linear system

1.3 Bistable energy harvesting

These techniques for increasing the bandwidth each have advantages and disadvantages. For a bistable system, the advantage lies in the large oscillation amplitude that can be obtained irrespective of the frequency. We need to be careful with the term 'irrespective' here though. The main contributing factor to the large amplitude oscillations is the amplitude of the vibration; nevertheless, resonance can still occur and induce this large amplitude oscillation.

1.3.1 Problem statement

Bistable harvesters can deal with real-world vibrations due to the reduced dependency on frequency. However, as much as we have a fluctuation in the frequency, the amplitude in real-world vibrations also varies. Bistable energy harvesters excel when exhibiting continuous large amplitude oscillations. To this end, we require sufficient acceleration (vibration amplitude) to overcome the potential barrier. However, as the vibration amplitude varies, continuous large amplitude oscillations cannot be guaranteed. This results in unpredictable and discontinuous large amplitude oscillations, diminishing the performance advantage of bistable systems in the process.

1

1.3.2 Research goal

The potential barrier height determines the threshold in vibration amplitude to achieve large amplitude oscillations. In stochastic resonance, the potential barrier height is relatively lowered periodically; however, this requires extra actuation. Hence arises the question: how do we passively lower the potential barrier to aid large amplitude oscillations? Taking a large leap forward, this question can be formulated as the research goal:

"***Stiffness compensation*** *in* ***compliant*** *oscillators.*"

This goal can be elaborated with the underlined terms.

Stiffness compensation

The potential barrier stems from the non-linear stiffness characteristic of bistable mechanisms. By taking the derivative of the potential energy with respect to e.g. a displacement, the force-deflection characteristic (Figure 1.3b) is obtained; its slope represents the stiffness. By comparing the potential curve (Figure 1.3a) with the corresponding force-deflection characteristic, we see that the potential barrier is the equivalent of the negative slope. Hence, by decreasing the slope, or compensating the stiffness, the height of the potential barrier also decreases. This process of "stiffness compensation" can also lead to static balancing. Statically balanced, neutrally stable, constant potential energy or zero-stiffness, all refer to mechanisms that are in a continuous state of equilibrium over a range of motion [8]. This suggests that the equilibrium spans between the two wells (Figure 1.3a); hence, the force-deflection characteristic has zero slope over the range of motion. To obtain such characteristics, we can introduce a positive stiffness (Figure 1.3b), exactly equal to the negative stiffness in the force-deflection characteristic, creating a zero slope in the process [9].

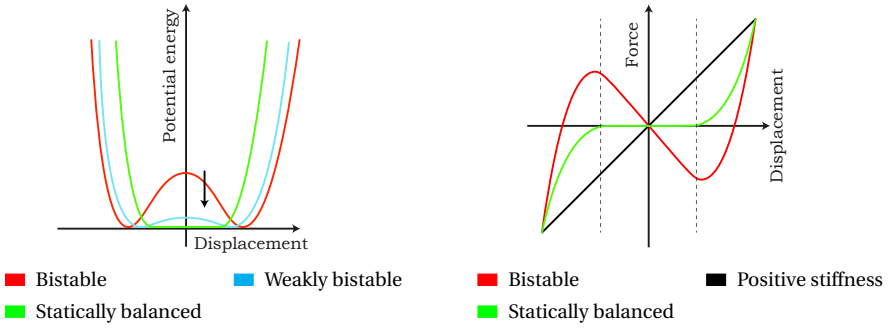

(a) Lowering of the potential barrier: from bistable, to weakly bistable to statically balanced. In the statically balanced curve, the equilibrium spans the motion range between the two wells of the bistable curve; however, it also suffers from loss of motion range

(b) Force deflection curves of a bistable system, linear positive stiffness and a statically balanced mechanism. The linear positive stiffness exactly matches the negative stiffness of the bistable system; however, with opposite sign, leading to cancellation of stiffness and the statically balanced system

Figure 1.3: Process of static balancing depicted with potential energy and force-deflection characteristics

As a result of the continuous equilibrium, the mechanism theoretically has no stiffness. This lack of stiffness presents itself as an opportunity to energy harvesting, as there is no resistance to an excitation, irrespective of the frequency or acceleration. Hence, a stiffness compensated energy harvester would be applicable to any kind of vibration and therefore in any kind of environment.

Compliant

A great deal of energy harvesting systems in literature is constructed through the assembly of several parts. The focus lies greatly on the application to real-world vibrations. However, for an energy harvester to have a real-world application, its production should also be easy. Assembly is a very time-consuming and therefore costly step in the production process. Additionally, for micro-scale devices, assembly is near impossible. In compliant mechanisms, several parts are substituted by elastic elements that fulfill the same function, reducing the number of parts greatly and requiring less assembly steps. To continue on manufacturability, a method for stiffness compensation with the focus on applicability to orthoplanar mechanisms is investigated. Planar mechanisms are constructed in one plane, not requiring any connection between parts in different planes. On a large scale, using laser cutting, or on a small scale using etching, this simplifies the production of prototypes greatly. The prefix "ortho" refers to the oscillation direction, which is out of plane: orthogonal to the planar surface of the mechanism (Figure 1.4).

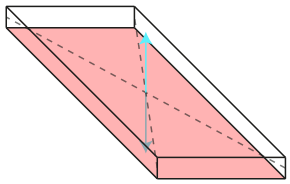

Figure 1.4: Schematic representation of orthoplanar. The mechanism is built from the red plane up and the oscillation direction is orthogonal to it

1.4 Thesis structure

The focus of this thesis lies on investigation of a stiffness compensation method for compliant mechanisms, which can be used to increase vibration energy harvester performance. Several topics are addressed: motion in bistable energy harvesters, buckling of structures, analytical and finite element modeling of post-buckled compliant structures.

The second Chapter of this work presents the resulting research paper of the literature phase on the topic of bistable energy harvesters. In particular, a classification of motion in bistable energy harvesters based on displacement time-series is presented. Additionally, an evaluation of performance of different motion types is conducted. This research paper resulted in the problem statement described above.

The third Chapter touches upon the topics of (bi)stability and buckling, acting as an introduction to the research hypothesis. This chapter presents a hypothesis in stiffness compensation in compliant mechanisms and the tools used to test this hypothesis.

In Chapters 4 and 5, two research papers on stiffness compensation in compliant mechanisms are presented. Chapter 4 tests the hypothesis analytically, numerically and experimentally using a simple post-buckled four-bar linkage model. It results in an analytical framework of stiffness compensation in four-bar linkages, and a designed mechanism that exhibits the hypothesized behavior. Chapter 5 acts as an application of the tested hypothesis on two existing compliant mechanism architectures, continuing on prior art in this field.

In the final Chapter, a critical reflection on the conducted work is given, together with conclusions, recommendations and direction for further research using the insights gained.

Background information to the papers can be found in the included appendices. Appendix A includes an elaborate presentation of the analytical model used in Chapter 4 as well as the prototyping phase and preliminary measurements to the final experiments. All analysis steps applied to the analytical model are presented in Appendix B. Analogously, Appendix C presents the modeling and prototyping phase for Chapter 5. Technical drawings for both final designs are given in Appendices D and E. The references used in all chapters, including the research papers, are taken up in a complete bibliography at the end of this thesis. Hence, it may seem as if the papers are incomplete, but the readability is significantly improved.

Chapter 2
A classification and performance evaluation of motion in bistable energy harvesters based on displacement time-series

In this chapter, the research paper created during the literature review phase on the topic of motion in bistable energy harvesters is presented. The paper starts with an overview of motions which a bistable energy harvesting may exhibit; this overview is accompanied by displacement time-series representations of each motion. The overview is further extended methods to distinguish the presented motions. Finally, the classification is used in the evaluation of performance of different motions found in the relevant literature.

A classification and performance evaluation of motion in bistable energy harvesters based on displacement time-series

A. Numić and T.W.A. Blad

2

Abstract

Bistable systems are widely used in the field of motion energy harvesting. This review presents a classification of the motions a bistable energy harvester may exhibit, by means of displacement time-series analysis. To this end, periodic and chaotic behavior are distinguished and the distribution of the motion is determined. The resulting classification presents intrawell, interwell and intermittent crosswell (multi-period, sporadic switching, recurring combination) as periodic bistable motions and chaotic intrawell and crosswell as chaotic motions. Finally, a comparison in performance between different motion regions is given. It was found that interwell overall performs best, followed by chaotic crosswell motion. The amplitude of the exhibited motion is of significant influence to the performance of the harvester.

Keywords

Bistable energy harvesting, time-series analysis, motion classification, performance

2.1 Introduction

Bistable mechanisms have been vastly studied in vibration energy harvesting applications, due to better performance and robustness as compared to linear resonant harvesters [10–14]. Linear resonant harvesters return a large energy output upon excitation in the resonant frequency and a narrow frequency band around it. However, real-world signals tend to have time-varying frequency over a broad range, and manufacturing tolerances induce deviation from the desired resonant frequency, rendering linear harvesters ineffective for practical applications [11, 12, 14, 15]. For bistable harvesters to outperform linear ones, the greater oscillation amplitude by virtue of the double-well potential, known as interwell motion that is obtainable over a broad frequency range and at low frequencies, is required continually [11–14, 16]. However, obtaining interwell motion is not straightforward, as there are more possible motions that may coexist [11].

In several works, a classification of possible bistable motions with explanation of the corresponding motion is given. A global overview of the possible motions is presented by Harne and Wang [12, 17] and Daqaq e.a. [11], including intrawell (i.e. the motion around in a single potential well), interwell (i.e. the motion over the double-well potential) and chaotic interwell motion. Harne and Wang [12] expand the intra- and interwell motion with a low- and high-amplitude variant. The existence of chaotic interwell motion in forced non-linear oscillators was experimentally investigated by Holmes [18] and analytically by Szemplińska-Stupnicka [19], whom also mentions the existence of chaotic intrawell motion. In the works of Arrieta e.a. [20] and Pan e.a. [21], intermittent interwell motion for bistable plate harvesters is investigated in addition to intra-, interwell and chaotic motion. Intermittent motion here is shown as continuous interwell motion interrupted by intrawell motion, or as intrawell motion switching between potentials due to interwell motion. Syta e.a. [22] and Betts e.a. [23] on the other hand present intermittent motion for bistable plates as a periodic recurrence of intra- and interwell motion. Kovacic and Brennan [24] present this periodic intermittency as the combination of interwell motion with different oscillation periods. In the work of Guo e.a. [25], a

classification is presented with intrawell and interwell motion, with interwell containing three groups: large amplitude limit cycle oscillations; chaotic motion; and large amplitude multiple periodic motions containing intrawell oscillation.

The types of motion can be distinguished by means of displacement time-series. This notion is used in the quantification of motion introduced by Heymanns e.a. [26, 27]. The analysis distinguishes intra- and interwell motion based on the so called 'large amplitude ratio', Ψ, determined by counting the number of jumps between wells, i.e. the number of times the distance between two peaks is greater than that between the equilibrium position, and dividing it by the total number of oscillations. $\Psi = 0$, $\Psi = 1$ and $0 < \Psi < 1$ indicate intrawell, interwell, and both intermittent and chaotic motion, respectively.

However, to date, no complete classification of distinct bistable motions exists in literature. It is necessary to have an unambiguous classification in order to compare future bistable harvesters. The objective of this research paper is to create a classification of the motion a bistable mechanism may exhibit. Such a classification enables a uniform terminology to be used in comparison of harvesters and motion types.

In Section 2.3, the methods used for classification are elaborated. Section 2.2 presents an overview of the existing bistable motions with graphical depiction and explanation. Additionally, the classification is applied to several harvesters, and the performance of different motion regions is compared. Section 2.5 the results and classification are discussed, and recommendations are given. Finally, Section 2.6 finishes with the conclusions that can be drawn.

2.2 Classification of bistable motion

2.2.1 Literature search method

The scientific literature used in this research was sought in the database of Scopus and Google Scholar. For the classification of different motions, only publications containing an explanation of a certain motion, as well as corresponding graphical representation were used. For instance, the characteristics of a certain motion were explained with reference to a time-series of the motion and a frequency spectrum. In Figure 2.1, a complete overview of bistable motions is given. Based on the information found in the form

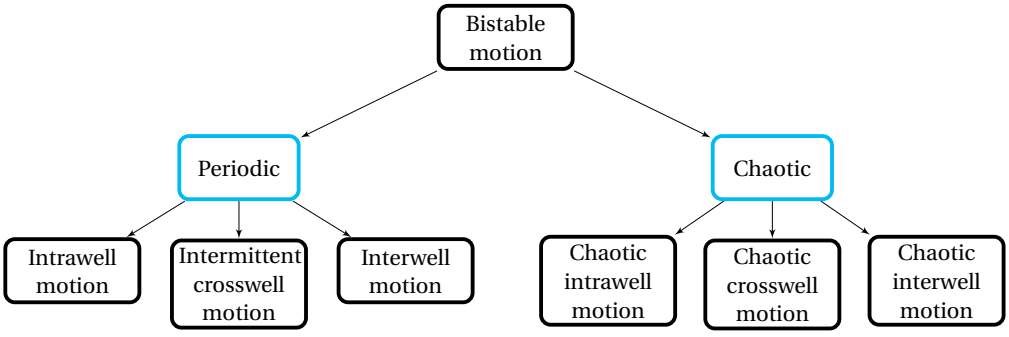

Figure 2.1: Tree-structure classification of bistable motion

of definitions and time-response data, each bistable motion is elaborated below, provided with an explanation of the motion and a time-response.

2.2.2 Intrawell motion

Intrawell or single-well motion, is the motion around one of the two equilibria in the double-well potential. It may exist in a low- and high-amplitude variant [12]. Intrawell motion may exist in periodic or chaotic form, depending on the excitation parameters and initial conditions. Periodic and chaotic intrawell motion are depicted in Figures 2.2a and 2.2b respectively. Chaotic intrawell motion may act as the onset of motion across the potential barrier [11, 28, 29].

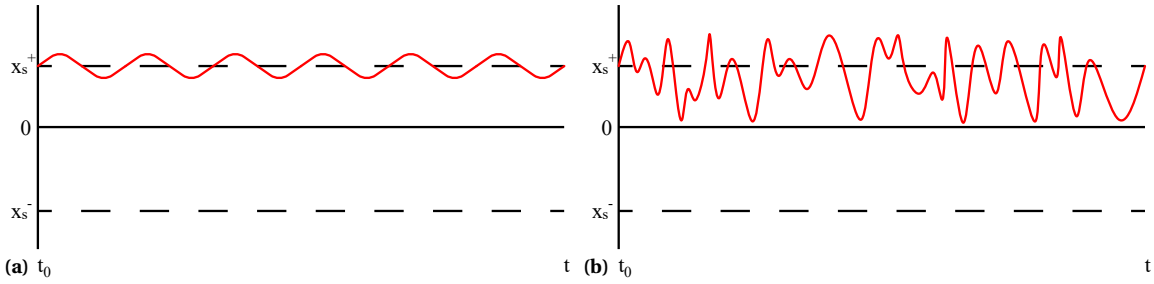

Figure 2.2: Displacement time-response of **(a)** periodic intrawell motion, **(b)** chaotic intrawell motion

2.2.3 Interwell motion

Interwell or double-well motion, is the periodic motion around the unstable equilibrium traversing the two potential wells, as depicted in Figure 2.3a [11, 12, 17, 22, 23, 27]. As intrawell motion, interwell motion has a low- and high-amplitude variant [12]. Depending on the excitation, interwell motion may occur at the fundamental excitation frequency, or exhibit sub- and super-harmonic interwell oscillations as well, leading to a multi-periodic interwell response [30]. As chaotic intrawell motion, a chaotic form of interwell motion exists, depicted in Figure 2.3b; however, chaotic interwell motion is mainly denoted as chaotic crosswell motion in literature.

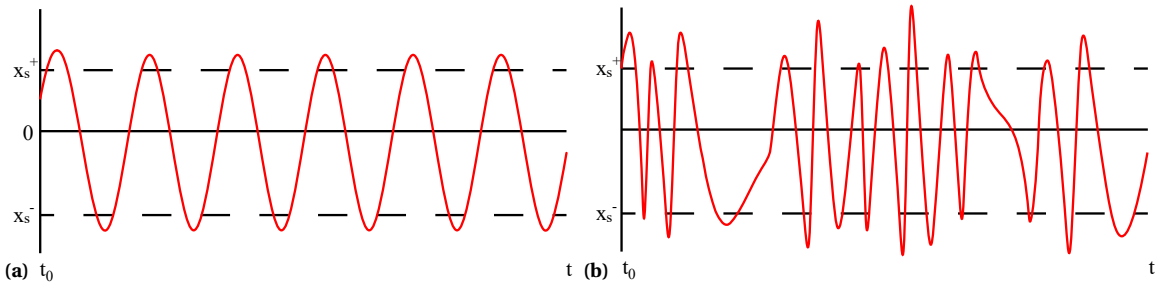

Figure 2.3: Displacement time-response of **(a)** periodic interwell motion, **(b)** chaotic interwell motion

2.2.4 Crosswell motion

Crosswell motion is a combination of intra- and interwell motion, containing intermittent and chaotic motion [11, 12, 17, 22, 23, 27].

Intermittent crosswell motion

Intermittent motion is continuous interwell motion interrupted by intrawell motion, or vice versa. It is mainly found as a result of period-doublings, leading to sub-harmonics, and is depicted in Figure 2.4a. Depending on the m number of sub-harmonics, this form of intermittency leads to period-m-motion; however, as m increases, the motion approaches chaos. In the relevant literature, mostly period-3 to period-5 motion is found [11, 24, 25].

Translating the form of motion in Figure 2.4a to predominantly interwell motion interrupted by intrawell dwells, returns intermittent motion as the sporadic switching between interwell and intrawell motion; an interpretation is displayed in Figure 2.4b. This switching does not necessarily have to be periodic [20, 31]. Intermittency can also be found as periodically recurring blocks of combined intra- and interwell motion [22, 32], as seen in Figure 2.4c.

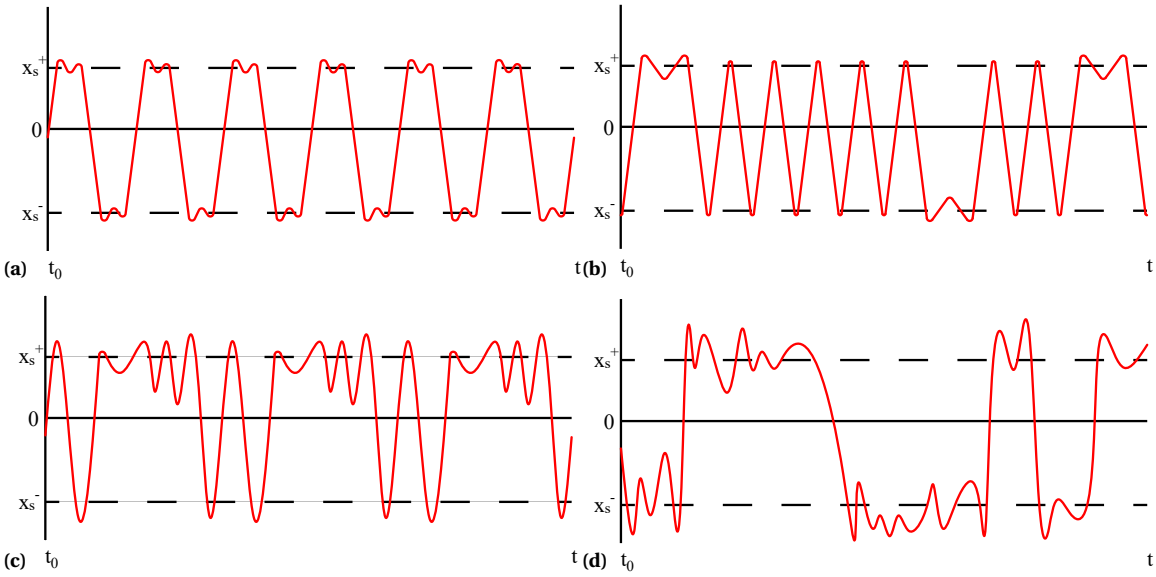

Figure 2.4: Displacement time-response of **(a)** multi-period intermittent motion, **(b)** intermittent motion with sporadic switching between single- and double-well motion, **(c)** intermittent motion with recurring combined single- and double-well motion pattern, **(d)** chaotic crosswell motion time-response

Chaotic crosswell motion

In chaotic crosswell motion, there is no recurring pattern between intra- and interwell motion [11, 12, 17, 23, 27]. For the same system exhibiting chaotic behavior, a slight change in initial conditions will result in a different response. In Figure 2.4d, a chaotic time-response is depicted.

2.3 Evaluating performance of motion types

The goal in designing a bistable harvester is to obtain interwell motion over a broad frequency range. However, as other motion types coexist, the relative performance of different motion types should be evaluated. To this end, a quantifiable distinction, in terms of periodicity, chaos, and motion nature is required.

2.3.1 Distinguishing chaotic from periodic motion

Chaotic motion is stated to be undesirable in energy harvesting applications, due to the need for conditioning and filtering [13, 17, 25]. For the sake of performance comparison, it is therefore necessary to distinguish chaotic from periodic motion. From the relevant publications, a time-series $X(i)$ at discrete sampling points $i = 1, 2, ..., N$ can be obtained and interpolated with a time-step Δt, in which periodic or chaotic characteristics can be identified using several techniques for time-series analysis. Frequency spectrum analysis using Fourier transform creates distinct peaks and a broadband cluster of peaks in the frequency spectrum for periodic and chaotic motion respectively. However, this clear distinction is not as trivial in practice [22, 27, 33]. Upon comparing intermittent (Figure 2.5a) and chaotic motion (Figure 2.5b) for instance, the frequency spectra show significant resemblance, leaving room for subjectivity.

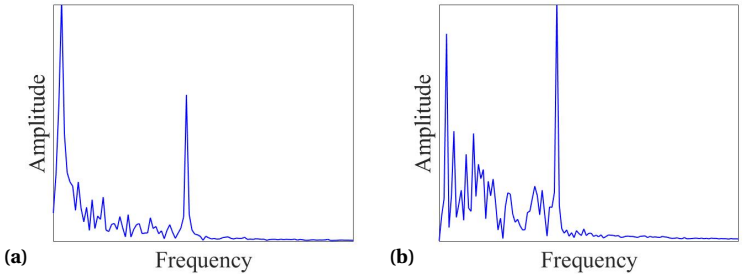

Figure 2.5: Frequency spectra of bistable motion. **(a)** intermittent motion, **(b)** chaotic motion

A more objective alternative is the estimation of the Largest Lyapunov Exponent, which is widely used in the case of known governing equations. The Largest Lyapunov Exponent returns the presence of chaotic of periodic behavior in a single parameter [34, 35]. In the case of only having a time-series X, i.e. no knowledge on the governing equations, the Lyapunov exponent can be estimated using algorithms by Wolf e.a. [36] or Rosenstein e.a. [37]. However, this firstly requires reconstruction of the phase-space and implementation of the algorithms is not straightforward [38]. Similar to the Largest Lyapunov Exponent, the 0-1 test for chaos by Gottwald and Melbourne [39], returns the presence of chaos or periodic behavior in a single parameter. The 0-1 test works directly with a given time series, requiring no phase-space reconstruction [32, 40, 41]. However, the 0-1 test showed difficulties in distinguishing recurring patterns from chaotic behavior [40].

Motion matching

The methods described above demonstrated difficulties in distinguishing periodic motion identified in literature from chaotic motion; therefore, a new method named "motion matching" is presented in this research to satisfy the goal of classification. Motion matching distinguishes periodic from chaotic behavior in a time-series X by determining the recurrence of a certain portion of the motion throughout the time-series, as depicted in Figure 2.6. Initially, a random portion of the time-series is taken by selecting a random point $X(t)$ and a subsequent point $X(t+\tau)$. τ denotes the time-delay, whose optimal value is obtained from the first minimum of the average mutual information between $X(t)$ and its time-shifted variant $X(t+\tau)$, as proposed by Fraser and Swinney [42]; if no minimum is found, the τ of the crossing with $1/e$ is taken [43]. The mutual information can be interpreted as the reduction of uncertainty on $X(t)$ with knowledge on $X(t+\tau)$. The first minimum therefore returns τ for which $X(t)$ and $X(t+\tau)$ are most independent. For recurring periodic behavior τ will be relatively small, since reduction of uncertainty will increase again (i.e. $X(t)$ and $X(t+\tau)$ become less independent) if $X(t)$ and $X(t+\tau)$ start overlapping as τ increases [35, 43]. Thus, for periodic behavior a small portion of the motion is taken, which will highly likely recur in the time-series. Contrariwise, τ will be relatively big for chaotic behavior, giving a greater portion of the motion that will less likely recur.

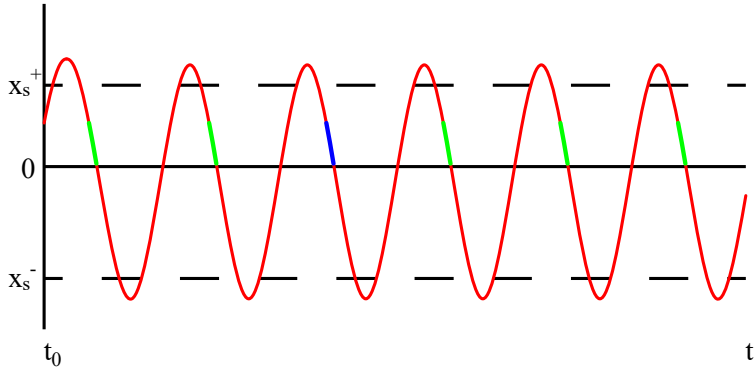

Figure 2.6: Depiction of motion matching on periodic double-well oscillation case. The portion used is indicated in blue and iterated throughout the time-series (red). The green sections depict the sections in X matching with the blue portion

The portion is iterated along the entire time-series in order to find sections of $X(t)$ that match with the portion. The process is repeated with a new random portion and the mean number of recurrences $\bar{R}$ is used as the indicator for periodicity or chaos. In Figure 2.7, the mean number of recurrences to the number of iterations (newly generated random portions) is displayed. While no exact steady state value is obtained, it is clear that from even under 50 iterations the mean number of recurrences for chaotic motion will tend to 1, while for periodic motion this rises above 1 depending on the nature of motion.

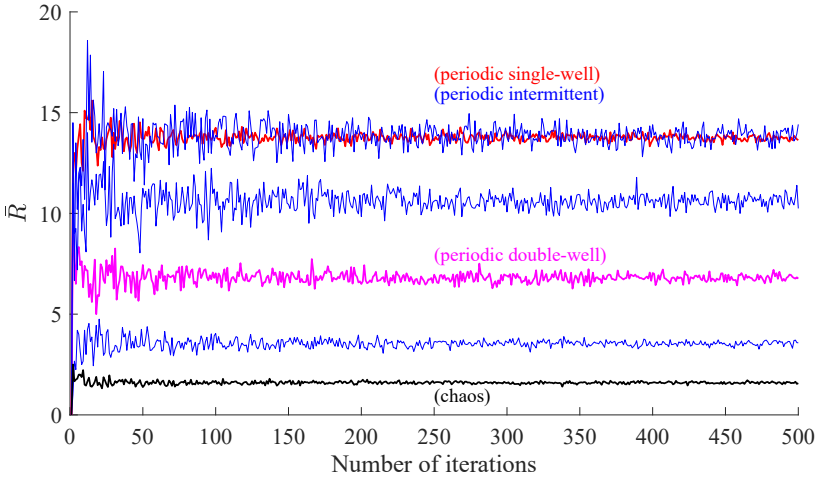

Figure 2.7: Plot of mean number of recurrences $\bar{R}$ to number of iterations used in motion matching. Chaotic motion (black) tends to 1, while the periodic motion (red, blue and magenta) tend to a value greater than 1 depending on the nature of motion

2.3.2 Distribution of motion

As interwell oscillations are desirable for greater performance, it is necessary to take the distribution of motion, i.e. the share of single- and double-well oscillations, into account. To this end, the method Heymanns and Hagedorn [26] introduced, lends itself as suitable. Figure 2.8 displays a time-series X with the equilibrium positions of the double-well potential indicated by the dashed lines and peaks by the blue dots. The displacement $|x_p - x_{p+1}|$ between each consecutive peak is determined and compared to the distance $|x_{s^+} - x_{s^-}|$ between the two equilibrium positions of the double-well potential. Parameter J_p can be found in (2.1); this keeps track of whether or not a jump between the two wells has occurred. The number of times a jump has and has not occurred is counted, as well as the total number of oscillations in the time-series. By dividing the first two by the latter, P_{intra} and P_{inter}, the percentage of intra- and interwell motion in the time-series respectively, are obtained.

$$J_p = \begin{cases} 1, & |x_p - x_{p+1}| \geq |x_{s^+} - x_{s^-}| \quad \text{(jump occurred)} \\ -1, & \text{otherwise} \quad \text{(no jump occurred)} \end{cases} \quad \text{for } p = 1, \ldots, N_p - 1 \tag{2.1}$$

2.3.3 Performance metric

The performance of an energy harvester, in terms of power output, fluctuates with the exhibited motion. As a metric relating the power output to the excitation, the volume figure of merit FoM_V, as found in (2.2), introduced by Mitcheson e.a. [44], is used. This metric is designed to compare harvesters; however, in the case of comparing motions for the same harvester, the dimensions and mass (L_z and $\rho_\text{M} V$) remain unchanged and are left out, resulting in the modified Equation (2.3). P_{avg} denotes the reported power output, Y_0 and ω the excitation amplitude and frequency respectively; in the case of

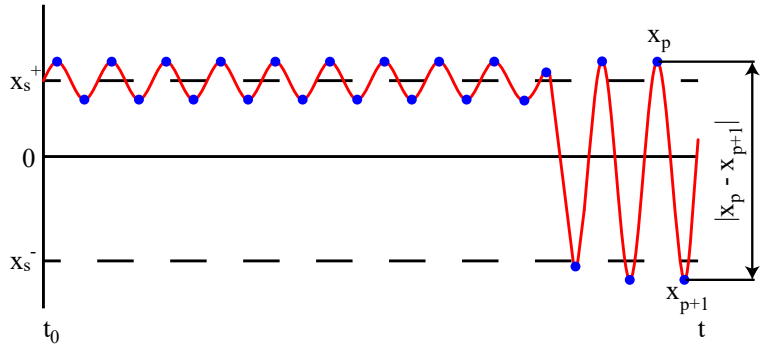

Figure 2.8: Example of displacement time-series. Equilibrium positions are indicated by the dashed lines at x_{s^+} and x_{s^-}; peaks are indicated with blue dots; the distance $|x_p - x_{p+1}|$ between two peaks is depicted

Y_0 given as acceleration, the denominator changes to $Y_0\omega$. Strictly, the FoM* is not a proper figure of merit, as it is not dimensionless and does not return a value between zero and one. However, its value tells clearly what the output power is with respect to the excitation. Finally, for each used reference in the results, the FoM* is normalised to the greatest value found in the corresponding work, resulting in a normalised power metric.

$$\mathrm{FoM_G} = \frac{P_{\mathrm{avg}}}{\frac{1}{16} Y_0 \rho_{\mathrm{M}} V L_z \omega^3} \cdot 100\% \tag{2.2}$$

$$\mathrm{FoM}^* = \frac{P_{\mathrm{avg}}}{Y_0 \omega^3} \tag{2.3}$$

2.4 Results

A bistable energy harvester may exhibit any of the motion discussed in Section 2.2, depending on the excitation case. In Figure 2.9, a selection of harmonically excited energy harvesters from literature, which had the displacement time-series and power output available, is presented. The displacement time-series are analyzed using the motion matching method and the $\bar{R}$-parameter is determined. Additionally, the intra- and interwell shares P_{intra} and P_{inter} are determined. For performance, the normalized power is included as well as the rms displacement of each motion, normalized to the greatest rms displacement in the corresponding work. Solely works that include several exhibited motions are taken up. For the work of Litak e.a. [45], the mass is included in the denominator of (2.3), as this parameter is changed to obtain different motions.

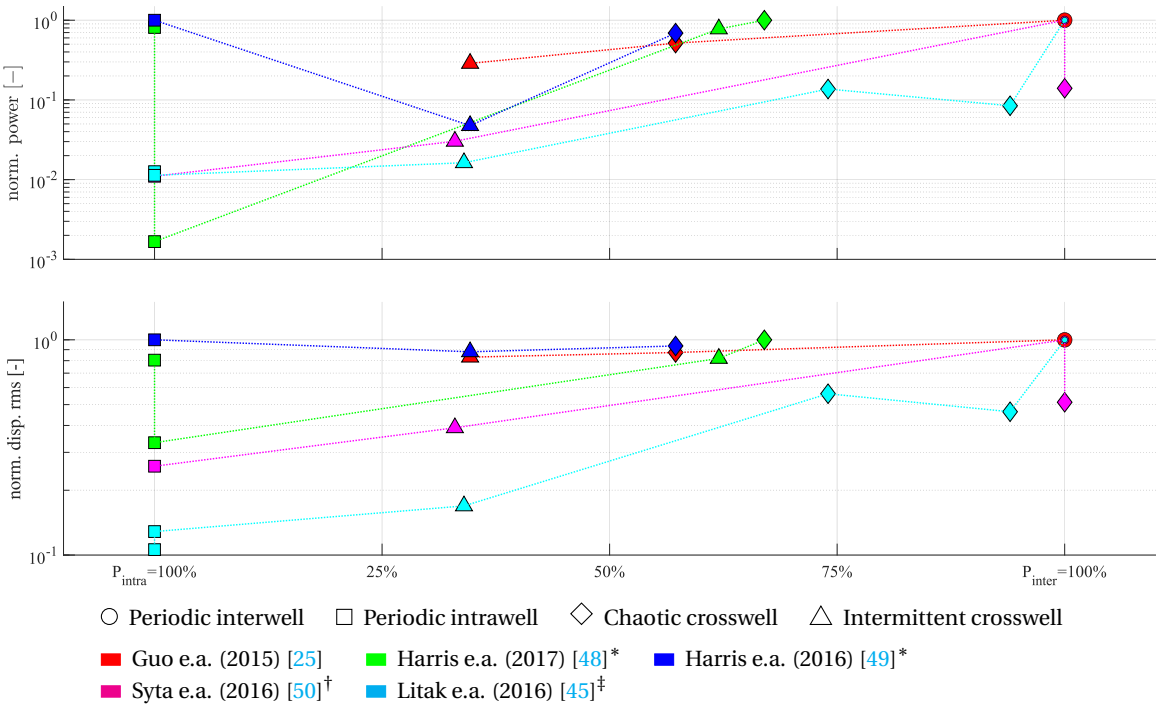

* Experimentally obtained data

† Different motions are obtained through modification of the simulation initial conditions (position and velocity)

‡ Different motions are obtained through modification of the oscillating mass in the model

Figure 2.9: Normalized power and normalized RMS displacement of harmonically excited bistable energy harvesters, versus distribution of motion (P_{intra} and P_{inter}) Motion types are indicated using different shapes. Different references are indicated using different colors; motions corresponding to one reference are connected with a dotted colored line

2.4.1 Motion distribution in literature

Periodic intrawell motion in the relevant literature is mainly found with a $P_{\text{intra}} = 100\%$ share. However, interestingly in the works of Holmes [18] and Nakano e.a. [46], chaotic motion with 93% and 92% intrawell share are still denoted as chaotic intrawell motion, even though there are interwell oscillations present. Analogous to periodic intrawell motion, periodic interwell motion is found with a $P_{\text{inter}} = 100\%$ share. Intermittent motion in the form of multi-period motion is found with roughly a $P_{\text{inter}} : P_{\text{intra}} = 1/3 : 2/3$ distribution. In the work Radice e.a. [47], the boundary between intra- and interwell on the one hand, and intermittent crosswell motion on the other hand is addressed. It is argued that provided that single-well oscillations are short compared to double-well oscillations, the motion is taken as interwell motion, and vice versa. However, this notion is not elaborated with a threshold regarding the motion distribution.

2.5 Discussion

The first notable result is that interwell motion returns the greatest performance for the evaluated energy harvesters. This is in accordance to that found in previous literature [11–14, 16]. Periodic interwell motion returns a continuous great voltage response, resulting in a greater power output. The share of interwell motion however, does not entirely contribute to a greater power output, as can be seen in Harris e.a. [49]. Intrawell returns the greatest normalized power as a result of the greater root mean square displacement; additionally, the excitation amplitude is lower for intrawell motion, increasing the normalized power. Even though chaotic and intermittent crosswell motion include an interwell share $P_{\text{inter}} > 0\,\%$, the root mean square displacement is smaller due to smaller amplitude intrawell oscillations. The increase in excitation amplitude is at the expense of performance in this case. The same is seen in Litak e.a. [45] for the two chaotic crosswell motion cases (equivalent excitation) with $P_{\text{inter}} = 74\,\%$ and $P_{\text{inter}} = 94\,\%$, of which the first (with lower P_{inter}) performs better, due to the greater root mean square displacement.

Chaotic motion is stated to be undesirable in energy harvesting applications, due to the need for conditioning circuits as the power output is chaotic as well [13, 17, 25]. However, as mentioned by Daqaq e.a. [11] and Harne and Wang [12], the capabilities of chaotic motion in energy harvesting have still not been researched thoroughly. As can be seen in Figure 2.9, chaotic crosswell motion returns normalized power exceeding that of intermittent crosswell motion in all the treated works. Hence, chaotic crosswell motion may be useful in applications that only require a sufficient power supply, and impose no demands on the regularity of this power supply.

2.5.1 Limitations of classification

In Section 2.2, a classification of the possible motion for bistable energy harvesters in literature is presented. This classification was made to create a complete overview of the possible motions in the field under one terminology. While various methods exist for differentiating periodic and chaotic motion, less information is available for creating a clear boundary between intra- and interwell motion and intermittency. Where multi-period intermittent motion can be identified using its frequency spectrum, recurring patterns and sporadic switching are not that recognizable. The latter imposes the greatest difficulty, as, to the author's knowledge, this has only been addressed by Radice e.a. [47] without quantification. Therefore, no quantification criteria are included for classifying the actual motions.

As mentioned in Section 2.2, low- and high-amplitude variants of intra- and interwell motion exist. These are not included as separate groups in the classification as they do not impose a significant difference in the motion. The result is solely visible upon examining the power output.

The work of Wu e.a. [51] presents the conditions required for excitation-induced stability in a bistable duffing oscillator. The resulting motion occurs between the two stable equilibria, which would be classified as intrawell motion, while it is in fact a considerable difference. However, the required excitation conditions are unique and the motion is not further encountered in practical applications. Therefore, it is chosen not to include it in the classification.

2.5.2 Recommendations

To expand this classification, a quantification of intermittency is required as to set the boundaries between the motion groups. A 'motion rate of change', determining the rate of change from intra- to interwell and/or vice versa over the time-series would enable such a goal. Using this motion rate of change, it would be possible to differentiate predominantly intrawell motion with a concentrated interwell part in the time-series, from intrawell motion continuously interrupted by interwell motion (and vice versa).

Using a quantification of motions, it would be interesting to create charts indicating the motion regions for a combination of excitation amplitude and frequency. Such charts could aid in experimental work to find the desired motion, or to assess the performance of harvesters in terms of obtainable motion.

2.6 Conclusion

Bistable energy harvesters are widely studied due to the increased performance and robustness as compared to linear systems. These traits require bistable harvesters to exhibit continuous interwell motion, which coexists with several other types of motion. In this research, a general classification of the possible types of motion is presented, creating a uniform terminology that is applicable to the field of bistable energy harvesting systems, enabling the comparison of performance of certain motion types, or harvesting systems exhibiting the same motion. The classification is created based on displacement time-series. Firstly, periodic and chaotic behavior are distinguished by means of 'motion matching'. This method records the recurrence of random portions of the time-series throughout the data; the mean number of recurrences ($\bar{R}$) will tend to 1 for chaotic motion. For periodic motion, $\bar{R}$ will tend to a number greater than 1; however, no distinct steady-state value exists for a certain motion type. Secondly, the percentage of intra- and interwell motion, P_{intra} and P_{inter}, are determined. The resulting classification presents intrawell, interwell and intermittent crosswell (multi-period, sporadic switching, recurring combination) as periodic bistable motions and chaotic intrawell and crosswell as chaotic motions. Trivially, intra- and interwell motion are distinguishable by $P_{\text{intra}} = 100\%$ and $P_{\text{inter}} = 100\%$, respectively. The common intermittent crosswell motion, resulting from sub- and super-harmonics, roughly returns a $P_{\text{inter}} : P_{\text{intra}} = 1/3 : 2/3$ distribution. However, the onset of intermittent motion from intra- or interwell motion remains undefined. The performance of different motions is evaluated using normalized power, relating the power output to the excitation, and the normalized rms displacement. In terms of performance, interwell motion returns the greatest normalized power and rms displacement, followed by chaotic crosswell motion. It was found that the share of interwell motion does not contribute to the power output as much as the overall amplitude does.

Chapter 3
Research hypothesis

In Chapter 1 we have touched upon the use of bistability as a means of broadening the bandwidth of energy harvesters. Moreover, it was stated that bistabilty is a starting point in methods for stiffness compensation. This chapter continues on the concept of bistability, with a more elaborate explanation using a beam model. This functions as an introduction to the research hypothesis. The hypothesis concerns a novel method for stiffness compensation in compliant mechanisms. Additionally, the tools required for testing this hypothesis are discussed in this chapter.

3.1 Bistability

In Chapter 1, it is said that in a bistable mechanism a large amplitude oscillation between the two wells, or equilibria, may occur. To understand this better, let us first look at the concept of stability of equilibria. In Figure 3.1a, a ball on a convex surface is displayed. If we were to push it up the convex hill, it would roll down, oscillate and come to rest at its original position. Since a perturbation does not change the equilibrium position, the ball is said to be in stable equilibrium. A perturbation would cause the ball in Figure 3.1b to start rolling downhill, away from the initial position; hence this represents an unstable equilibrium. In Figure 3.1c, a perturbation would neither make the ball return to its initial position, nor make it continuously move away. In this case, the ball is said to be in a neutral equilibrium.

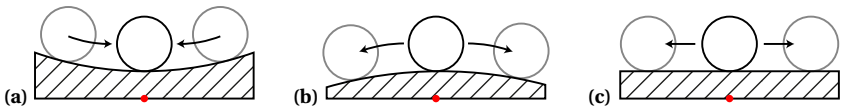

Figure 3.1: Stability of equilibria: stable (a), unstable (b) and neutrally stable (c) equilibria depicted with ball analogy. Perturbation of the ball is depicted with the grey balls on either side. The red dot indicates the datum for the ball's vertical displacement

Stability can also be assessed by means of the potential energy Φ of the system. The potential energy of the ball is proportional to the ball's vertical displacement with respect to a datum, which in this case is the red dot. In any equilibrium, the potential energy takes a stationary value; for the equilibrium to be stable, the potential energy has to be a local minimum [52, 53]. In the stable equilibrium, a perturbation would only increase the potential energy of the ball with respect to the initial position. In the unstable equilibrium, the potential energy is at a maximum, meaning that a perturbation will make the ball roll away and seek a minimum. In the neutrally stable equilibrium, a perturbation does not change the potential energy, so there is no tendency to seek a minimum; hence, the ball is in equilibrium at every position [54]. Figure 3.2 uses this analogy to relate bistability and neutral stability. Three equilibria, I, II and III are depicted together with their height with respect to the datum. In a bistable system (Figure 3.2a), to achieve a large amplitude oscillation between I and III, the potential energy has to increase with $h_{\mathrm{II}} - h_{\mathrm{I}}$. This increase in potential energy has to be provided as input energy, in the form of e.g. acceleration of the ball's mass in the case of dynamics, or force in the case of statics. In the neutrally stable system (Figure 3.2b), the three equilibria are located at the same height, and hence the ball has the same potential energy in all three. Therefore, we do not depend on an increase in potential energy when moving from I to III, of course assuming there is no friction, and it can be said that the movement between I and III becomes easier as the barrier height is reduced. The ball's potential energy can be mapped on the displacement δ to obtain the potential energy curves in Figure 3.2c. Blue and magenta dots indicate the stable equilibria; a black dot indicates the unstable equilibrium for the bistable case.

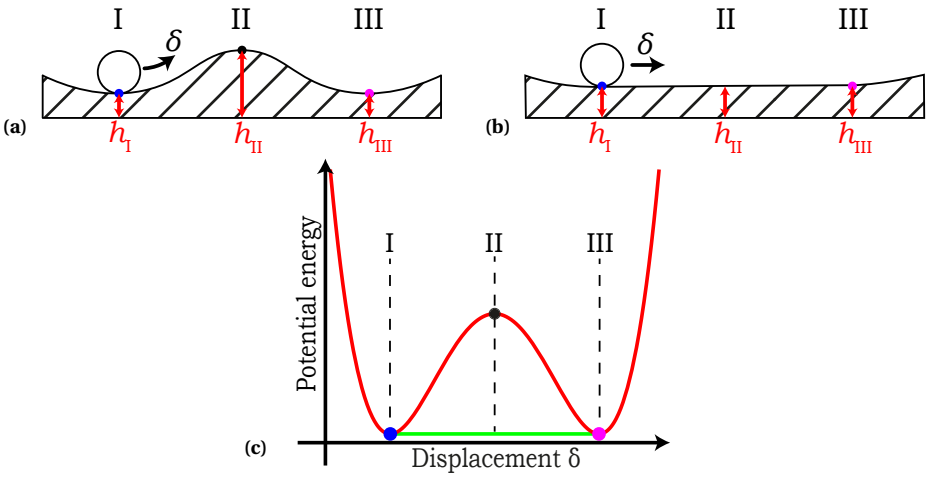

Figure 3.2: Comparison of movement between states I and II for bistable (a) and neutrally stable (b) system. For the bistable system ( ), I and III are separated by a barrier of height h_{II}, which results in an increase in potential energy for horizontal displacement δ (c), which has to be overcome with input energy. For the neutrally stable system ( ), the potential energy is constant between I, II and III

3.2 Buckling

Whereas the ball analogy is very insightful for bistability, it lacks a relation to stiffness compensation. Therefore, we need to turn to a mechanical element that can exhibit the same behavior. In this case, bistability requires two main ingredients: a deformable element. e.g. a slender beam, and a pre-load of some sort. Pre-load can be introduced by means of a force, displacement or stress. Let us start from a simply supported slender beam in a flat unloaded state, as displayed in Figure 3.3. By applying an axial load P on the right side, the beam will initially act as a spring: it will compress as a result of the applied load. However, once load P reaches a certain threshold value, the beam will lose the ability to carry the load and it will deflect drastically in transversal direction. The resulting deformed beam is displayed in Figure 3.3 in gray.

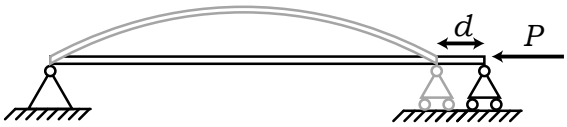

Figure 3.3: Depiction of an undeformed simply supported slender beam. As a result of an axial load P reaching the critical load P_{cr}, the beam will displace a distance d in axial direction and buckle into its first buckling mode from the flat state

This phenomenon of abruptly changing from axial compression to large transversal deflection is called buckling, or strictly bifurcation buckling. The load at which this happens is called the critical buckling load P_{cr}, and the obtained shape is the corresponding buckling mode/shape. In theory, multiple buckling modes exist, each with their own

corresponding buckling load. The first buckling mode corresponds to the lowest buckling load, the second buckling mode to the second lowest load, etc. In practice however, a beam will buckle in its first mode as this requires the least loading; this is the mode in gray displayed in Figure 3.3. The beam is now said to be in its post-buckled state [53, 55]. As a quick excursion, let us address the slenderness of the beam. The word 'slender' is key; it has to hold that our beam is significantly thin with respect to its length $\left(h^2/L^2 \ll 1\right)$ for buckling to occur instead of plastic deformation.

Buckling can be related to stability by looking at the potential energy Φ of the beam. This potential energy consist of two contributions: the elastic potential $\mathscr{E}$ and load potential $\mathscr{B}$. The elastic potential accounts for the energy governed by deflection of the beam, i.e. strain and bending energy. The load potential accounts for the work done by displacement of imposed loads. The total potential is given by Expression (3.1).

$$\Phi = \mathscr{E} + \mathscr{B} \tag{3.1}$$

Suppose we introduce a perturbation of the beam's flat state in Figure 3.3 by imposing a small transversal displacement. This will result in a small variation of the total potential: the beam deflects, giving $\Delta\mathscr{E}$, and the load is displaced, giving $\Delta\mathscr{B}$. For the equilibrium to remain stable, we require a positive variation in potential energy, i.e. the potential energy increases due to the perturbation, which holds if

$$\Delta\mathscr{E} > \Delta\mathscr{B}$$

Contrariwise, if the variation in potential energy is negative, stability is lost. Hence, the equilibrium is unstable if

$$\Delta\mathscr{E} < \Delta\mathscr{B}$$

This means that the onset of buckling is found in the critical point given by

$$\Delta\mathscr{E} = \Delta\mathscr{B}$$

The variation of potential energy is not changing in this case, which is equivalent to a neutrally stable equilibrium [54].

3.3 Hypothesis

The beam in post-buckling will have attained the first buckling shape. This may be a bridge in positive y-direction, hence called the B-mode, or the mirrored shape in negative y-direction, which we define as the -B-mode. Let us assume that the B-configuration is the obtained shape after bifurcation buckling. The transversal post-buckling behavior of the beam can be analyzed by actuating the middle of the beam with an incremental displacement δ as in Figure 3.4a and recording the force required to do so. The force-deflection characteristic that is obtained and the corresponding potential energy curve are displayed in Figures 3.4b and 3.4c respectively. Following the force-deflection characteristic, we reach a limit point in the load (green dot). It is crucial that there is a prescribed displacement instead of a force. By imposing a force, the beam would snap-through abruptly after the limit point, which is called limit load buckling [55]. An insightful example for this force-displacement characteristic would be a light switch. When

moving a switch from on to off, the required force to do so increases gradually as we approach the middle. Releasing the force just before the limit point makes the switch jump back into its original state. After the limit point however, the required force decreases, meaning that there is no displacement corresponding to an increase in force nearby. The actual displacement is on the other side of the force-displacement characteristic. This sudden jump in displacement is called snap-through, and is also observed in flicking a switch: it pulls itself into the other state when pushed adequately [52]. However, by controlling the displacement of the beam, snap-through is prevented, allowing us to see what happens when moving from B to -B. By increasing δ further, the beam gradually attains an S-shape, until a perfect S-shape is obtained when the middle point is exactly on the horizontal axis. We define this shape as the S-mode, which is the second buckling mode of the beam. Note that this mode is not obtained by increasing P but by deflecting the beam transversally.

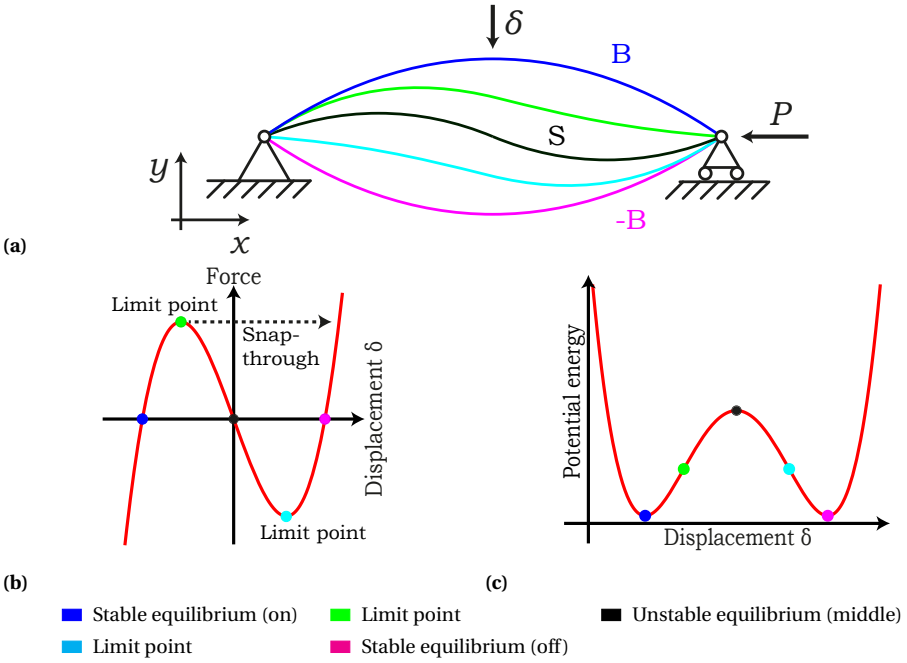

Figure 3.4: Displacement controlled deflection of bistable buckled beam (a). The colors correspond to the dots in the potential curve (b) and force-deflection characteristic (c). The black dot on top of the potential barrier corresponds to the S-shape of the beam, which is the second buckling mode

Hence, during deflection, the beam transitions from the first buckling mode to the second mode and back to the first mode. When looking at the potential energy curve in Figure 3.4c, this second buckling mode complies with the top of the potential barrier, meaning that the transition into the second mode is equivalent to moving up the potential barrier.

This observation gives rise to the thought that if it is easier to transition between the first two buckling modes, the potential barrier is lower, which means that the stiffness in the mechanism is reduced and eventually canceled out. In this case, the first two buckling loads should be close to one another, bringing the buckling modes closer together, which is phenomenon is called buckling mode interaction. This can be formulated as the following hypothesis:

"*Buckling mode interaction can be used as a method for stiffness compensation*"

3

3.4 Tools

To test this hypothesis, a few tools are required. Firstly, a model that describes the problem has to be proposed. This model has to be simple enough to be insightful, but still describe the problem well. Of course, a solution method to analyze this model is required. To this end, literature on buckling analysis is used to find a suitable method.

3.4.1 Description of problem

In the hypothesis, we are interested in interaction of the first two buckling modes, meaning that a model describing two buckling modes is required. The most accurate description would be using a continuous beam model, which captures the two buckling modes perfectly. However, a continuous model also introduces immense complexity. Therefore, a rudimentary description of the buckling modes is required. With a combination of links and rotational joints, a basic description of the buckling modes can be established:

- **B buckling mode**: the B buckling mode is half a sine wave. The most rudimentary description is a triangle consisting of two links and three hinges, as in Figure 3.5a.
- **S buckling mode**: the S buckling mode is a sine wave. The most rudimentary description is two consecutive triangles consisting of three links and four hinges, as in Figure 3.5b.

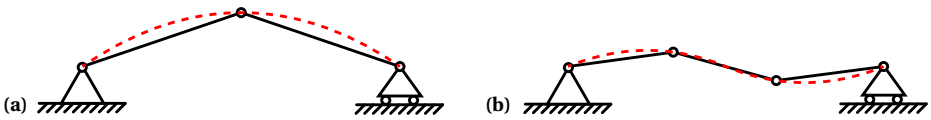

Figure 3.5: Rudimentary descriptions of (a) B and (b) S buckling modes using linkages

Hence, a four-bar linkage with four joints and one slider joint will suffice to describe the two buckling modes. This discrete model allows for simple solution of the mechanics behind buckling mode interaction.

3.4.2 Buckling problem

In order for us to look into buckling mode interaction, the buckling modes and corresponding loads have to be determined. To this end, several methods exist and are

grouped in two main approaches. The first is the vector approach, which uses Newton's second law to find the governing equations of the system of interest. The second approach is establishing these governing equations by minimizing the potential energy of the system, given that it is conservative. The resulting governing equations are in the form of an eigenvalue problem, in which the eigenvalues and eigenvectors represent the buckling loads and corresponding modes respectively [55]. The energy approach lends itself as a simple method for systems in which solution of the governing equations becomes complex [54]. While this is not to be expected from the linkage in Section 3.4.1, this method is quick way to obtain an estimation of the buckling loads and modes. Recall the critical condition given to find the buckling loads: an equilibrium in which the variation of the total potential does not change. This is equivalent to finding a stationary value of the potential energy that does not change, i.e. a point in the potential energy with zero slope and no change of the slope. The work of Budiansky [56] gives an elaborate overview of the energy approach, following the principle of virtual work, to find the buckling loads and modes. This approach will be explained and discretized here without delving into the mathematics behind it, as these are not crucial for the problem to be solved.

The potential energy is a functional of the degrees of freedom $\mathbf{u}$ and the scaling of the applied load λ. First, it is required that the system is in equilibrium, i.e. the potential energy is to be stationary, which is defined in (3.2). This expression states that Φ is stationary with respect to a variation of the degrees of freedom $\delta\mathbf{u}$. However, for the principle of virtual work to hold, $\delta\mathbf{u}$ has to be kinematically admissible and it has to hold that $\delta\mathbf{u} \neq 0$.

$$\delta\Phi\left[\mathbf{u};\lambda\right] = \Phi'\left[\mathbf{u};\lambda\right]\delta\mathbf{u} = 0 \tag{3.2}$$

Expression (3.2) returns the equilibrium equations of the system, which are solved to obtain the pre-buckling solution, $\mathbf{u}_0$, that describes the degrees of freedom in the equilibrium prior to buckling. With the pre-buckling solution established, we need to assess the stability of this solution following Section 3.2. As finding the equilibrium is equivalent to setting the first derivative of the potential energy with respect to the degrees of freedom equal to zero, finding a neutral equilibrium is equivalent to setting the second derivative equal to zero. This is found in Expression (3.3), which is called the buckling condition. Here λ_c denotes the critical buckling load and $\boldsymbol{\theta}$ denotes the vector describing the buckling modes. The buckling condition tells us to load the beam from its pre-buckling solution up to the critical load and evaluate the stability of that equilibrium for a small perturbation of the degrees of freedom.

$$\delta\Phi''\left[\mathbf{u}_0(\lambda_c);\lambda_c\right]\boldsymbol{\theta}\,\delta\mathbf{u} = \Phi_c''\boldsymbol{\theta}\,\delta\mathbf{u} = 0 \tag{3.3}$$

The buckling condition returns an eigenvalue problem from which the buckling loads and modes are obtained, which will only follow from a non-trivial solution. Since it holds that $\delta\mathbf{u} \neq 0$, a trivial solution returns $\boldsymbol{\theta} = \mathbf{0}$. However, this would mean no buckling is occurring. Therefore, a non-trivial solution follows from a singular Φ_c''. Expressions (3.2) and (3.3) are given as functional expressions; however, for a discrete system as the linkage model with degrees of freedom u_i, both Expressions simplify greatly to (3.4a) and (3.4b) for n degrees of freedom. The buckling loads and modes are then obtained from

$\det\left(\left.\frac{\partial^2\Phi}{\partial u_i \partial u_j}\right|_{\mathbf{u}_0[\lambda_c]}\right) = 0$ [53]. Finally, we can identify what parameters govern the values of the buckling loads and establish the conditions for buckling mode interaction. Eventually, the effect on the force-deflection characteristic in transversal deflection can be evaluated as depicted in Figure 3.4.

$$\sum_i^n \frac{\partial \Phi}{\partial u_i}\delta u_i = 0 \tag{3.4a}$$

$$\sum_j^n \left.\frac{\partial^2 \Phi}{\partial u_i \partial u_j}\right|_{\mathbf{u}_0[\lambda_c]} \theta_j \delta u_i = 0 \tag{3.4b}$$

3.4.3 Buckling modal basis

The potential energy Φ is a function of the degrees of freedom $\mathbf{u}$. These degrees of freedom describe the any configuration of the system in question. Hence, the deformation as well as the buckling modes are entirely described in terms of $\mathbf{u}$. The choice of $\mathbf{u}$ is free: we may arbitrarily choose a set of degrees of freedom. A usual choice for instance, is the nodal displacements of the system, or rotations of bodies in for example linkages. Since we are interested in the buckling modes, another option arises. If the degrees of freedom $\mathbf{u}$ describe the buckling modes $\boldsymbol{\theta}$, then $\boldsymbol{\theta}$ may be used to describe $\mathbf{u}$. This can be formulated as (3.5).

$$\mathbf{u} = \boldsymbol{\theta}\mathbf{m} \tag{3.5}$$

Here $\mathbf{m}$ denotes the modal amplitudes, which describe the scaling of the modes in the current configuration. What we are essentially doing here is mapping $\mathbf{u}$ onto a basis described by the buckling modes. These buckling modes are eigenvectors, or simply said shapes, that we can arbitrarily scale with an amplitude and hence obtain combined shapes that e.g. describe the displacement field as in Figure 3.4a. This is similar to modal analysis in dynamics, in which the vibration response of a system may be expressed as a linear combination of the vibration modes [57]. As a result, we may for instance describe the potential energy in terms of the buckling modes and decompose it in each of their contributions, which allows for an interesting analysis regarding the effect of mode interaction [58].

The tools here are solely a brief introduction for the reader to get acquainted to what will be used further in this thesis. Chapter 4 presents the actual application of these tools in the form of a research paper. Appendices A and B provide an in depth step-by-step elaboration of the linkage buckling problem and modal analysis respectively.

Chapter 4
Stiffness compensation through matching buckling loads in a compliant four-bar mechanism

This chapter presents the research paper on a novel method of stiffness compensation, or static balancing. The work is a fundamental test of the hypothesis in Chapter 3, and presents an analytical framework, mechanism design and experimental verification. An analytical four-bar linkage model provided with four torsion springs in the joints is proposed and defined as the torsion spring linkage. It is analytically shown that by making the outer torsion springs three times stiffer than the inner two, static balancing is achieved. This analytical model is translated into a lumped-compliant four-bar mechanism and it is experimentally shown that the behavior in the analytical model occurs in practice as well, verifying the hypothesis. Modal analysis is used to establish an explanation of the observed behavior. Furthermore, upon comparison to literature, it is observed that the analytical model describes the behavior found in continuous bistable buckled beams.

Stiffness compensation through matching buckling loads in a compliant four-bar mechanism

A. Numić, T.W.A. Blad and F. van Keulen

Abstract

In this paper a novel alternative method of stiffness compensation in buckled mechanisms is investigated. This method involves the use of critical load matching, i.e. matching the first two buckling loads of a mechanism. An analytical simply supported four-bar linkage model consisting of three rigid links, four torsion springs in the joints is proposed for the analysis of this method. It is found that the first two buckling loads are exactly equal when the two outer springs are three times stiffer than the two inner springs. The force-deflection characteristic of this linkage architecture showed statically balanced behavior in both symmetric and asymmetric actuation. Using modal analysis, it was shown that the sum of the decomposed strain energy per buckling mode is constant throughout the motion range for this architecture. An equivalent lumped-compliant four-bar mechanism is designed; finite element and experimental analysis showed near zero actuation forces, verifying that critical load matching may be used to achieve significant stiffness compensation in buckled mechanisms.

Keywords

Stiffness compensation, static balancing, buckling, compliant mechanisms

4.1 Introduction

A statically balanced mechanism is in static equilibrium in every point over a finite range of motion. In this case, the total potential energy of the mechanism is constant [8]. Static balancing may for instance be used to compensate for the gravity load of a mechanism. Not only gravity loads, but also elastic energy stored during deformation such as in compliant mechanisms (CMs) can be balanced. As a result, the force required for this deformation is zero [59].

A frequently used method to achieve static balancing in for example linkages, is an intricate synthesis of ideal springs and auxiliary rigid bodies [60–63]. The springs are responsible for counteracting undesired forces occurring during deflection. In CMs, strain energy accumulates in the elastic elements due to their inherent positive stiffness [64]. Static balancing in CMs is achieved through stiffness compensation, i.e. cancellation of the positive stiffness using equal but negative stiffness [65]. This negative stiffness is introduced through pre-loading of elastic elements. Accumulated strain energy is compensated by the energy stored in the pre-loaded elements during the deformation [66]. As a result, the net change in energy is small; hence, the required input force reduces [67].

Current methods of stiffness compensation require an iterative process of finding the correct negative stiffness and force-deflection characteristics [68, 69], or geometrical optimization [59, 70–72]. Kuppens e.a. [73] introduced a novel notion on using pre-loading in stiffness compensation of CMs. In this work, the stiffness of a mechanism was minimized by matching the first two critical buckling loads. Blad e.a. [74] defined the ratio between these buckling loads as the critical load ratio (CLR), which is used to identify the variation of potential energy between the equilibria of the buckled mechanism in question. The CLR was applied as a strategy to balance several orthoplanar CMs and the effect of geometrical parameters on the mechanical behavior was investigated. It was

shown that by maximizing this ratio, i.e. matching the two buckling loads, a minimal actuation force is obtained in transversal deflection. This method may be a simple alternative for stiffness compensation in designing statically balanced CMs. However, the working of this method has yet to be applied to lumped-compliant mechanism, for e.g. stiffness compensation in linkages.

In this research, the use of the CLR as a means of stiffness compensation is investigated. The goal of this paper is to present an analytical approach to stiffness compensation using the CLR, as to establish it as a new method.

In Section 4.2, the concept of stiffness compensation using the CLR is presented. Subsequently, an analytical framework using a four-bar linkage with torsion springs is formed. The buckling problem for this analytical model is solved, the CLR is established, and modal analysis of the deformation is discussed. Additionally, the mechanical design of the lumped-compliant four-bar mechanism, finite element modeling and the experimental setup are discussed. In Section 4.3 the results obtained from the analytical, finite element and experimental analyses are presented. Section 4.4 discusses upon these results and concluding remarks are given in Section 4.5.

4.2 Methods

4.2.1 Buckling of four-bar linkage

Buckling is feared in engineering due to the danger of catastrophic failure of structures [53]. When several buckling loads are close together, a phenomenon defined as buckling mode interaction, this danger grows significantly larger [75]. In this research however, exactly this phenomenon is used for stiffness compensation in a four-bar linkage. Figure 4.1a displays a schematic representation of this four-bar linkage. Its flat configuration in Figure 4.1a is a stable equilibrium which is defined as the pre-buckling state [56]. The slider joint allows for axial pre-loading by means of e.g. an axial load P. During pre-loading, the axial load P is gradually increased while the linkage preserves its flat configuration, up to the point that it holds $P = P_{cr,1}$. Eventually, the linkage deflects transversally in e.g. the gray buckled configuration. Its force-deflection (FD) behavior may now be evaluated by imposing an external load F in an arbitrary location, and deflecting the linkage in y-direction.

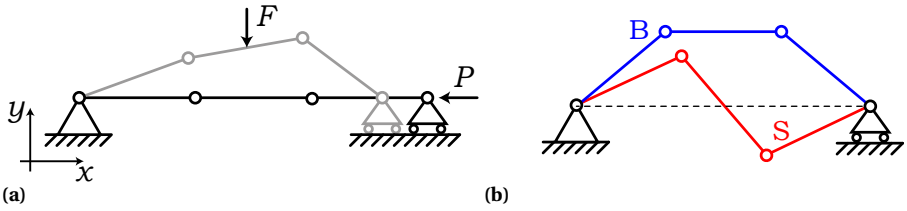

Figure 4.1: Schematic representation of four-bar linkage in flat and buckled state (a) and its two buckling modes (b). As a result of axial load P, the linkage buckles from the flat into the deformed (gray) configuration from which it may be transversally deflected using an external load F. The linkage has two buckling modes: the B-mode ● and the S-mode ●

$P_{cr,1}$ is the first critical buckling load, i.e. the lowest axial load at which the pre-buckling state loses stability, and bifurcates into a new equilibrium that is called the post-buckling state [55]. Figure 4.1b displays the possible post-buckling equilibria of the linkage, which are the two buckling modes. These are defined as the B and S-modes, as the linkage forms a bridge and S-shape, with their corresponding critical buckling loads P_{B} and P_{S} respectively. The CLR, i.e. the ratio of these two buckling loads, describes the variation of potential energy between the equilibrium states of a buckled mechanism [74]. During transversal deflection, the linkage will transition between these equilibrium states. By achieving a unity CLR, the two buckling loads, and thus the potential energies in the equilibria, are equal. As a result, constant potential energy between the equilibria, and hence static balancing, is obtained. This effect is visualized with the strain energy contributions of the B and S-modes under transversal deflection using modal analysis in Section 4.2.2. A more practical visualization is by means of the force-deflection (FD) characteristic of the linkage under transversal deflection, as described in Section 4.2.2.

4.2.2 Analytical framework

To use the CLR as a method for stiffness compensation, the buckling loads and modes of the linkage have to be obtained. Figure 4.2 displays the proposed model of the torsion spring linkage (TSL) used in this analysis. The TSL consists of three rigid links of length L; and torsion springs in the joints with stiffness k_a, k_b, k_c, and k_d, which capture the elastic properties of the linkage. Additionally, a spring with stiffness k in axial direction functions as the pre-loading mechanism: by displacing the frame connection a distance d in $-x$ direction, the linkage is loaded axially and brought into post-buckling. The four-bar linkage allows for one degree of freedom (DoF) as a description of the kinematics. A second DoF, required to prevent singularities in the kinematics, is obtained by relaxing the axial displacement in one end by means of a slider joint. The two DoFs are chosen as $\mathbf{u} = [\varphi_1, \varphi_2]^T$; additionally, moderate rotations ($\varphi^2 \ll 1$) are assumed. The resulting stiffness compensation is evaluated by means of the FD characteristic of the TSL under deflection in y-direction. To this end, two external loads, an asymmetric load F_a and symmetric load F_s, are imposed in O_a and O_s respectively.

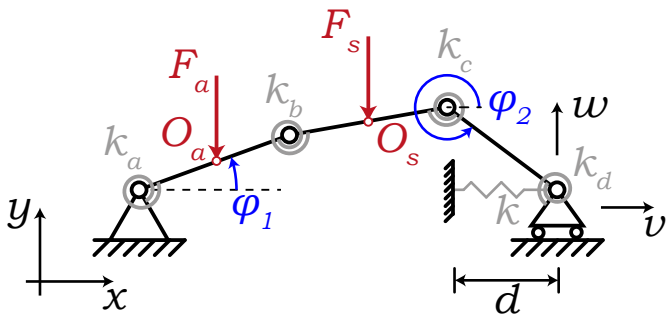

Figure 4.2: Schematic representation of torsion spring linkage. By applying a pre-loading displacement d to the rigid connection of spring k, the linkage is brought into a buckled state in which an asymmetric load F_a and symmetric load F_s are imposed in O_a and O_s respectively

Buckling problem

First, the buckling problem is solved using the energy approach [54], which will return the bifurcation buckling loads and corresponding modes. To this end, the potential energy Φ of the TSL is can be found in (4.1).

$$\begin{aligned}\Phi[\mathbf{u};d;F_a;F_s] = &\frac{1}{2}k_a\varphi_1^2 + \frac{1}{2}k_b\left(2\varphi_1+\varphi_2\right)^2 + \frac{1}{2}k_c\left(\varphi_1+2\varphi_2\right)^2 + \frac{1}{2}k_d\varphi_2^2 \\ &+ \frac{1}{2}k\left[d + L\left(\varphi_1^2+\varphi_1\varphi_2+\varphi_2^2\right)\right]^2 + \left(\frac{1}{2}F_aL + \frac{1}{2}F_sL\right)\varphi_1 - \frac{1}{2}F_sL\varphi_2\end{aligned} \tag{4.1}$$

The first step in solving the buckling problem is obtaining the equilibrium equations, by finding a stationary value of the potential energy with respect to a kinematically admissible perturbation of the DoF $\delta\mathbf{u}$ using (4.2) [53, 56]. The obtained equilibrium equations are subsequently made dimensionless and can be found in (4.3). $\bar{\Phi}$ denotes the dimensionless potential energy; parameters $\alpha = (k_a+3k_b)/(k_b+k_c)$ and $\beta = (k_d+3k_c)/(k_b+k_c)$ describe the stiffness ratios between the torsion springs in the linkage; $\omega = kL^2/(k_b+k_c)$ governs the dimensionless axial stiffness; $\lambda = d/L$ denotes the dimensionless pre-loading that is imposed; and $f = F/(kL)$ denotes the dimensionless imposed external load.

$$\delta\Phi = \Phi'\delta\mathbf{u} = \frac{\partial\Phi}{\partial\varphi_1}\delta\varphi_1 + \frac{\partial\Phi}{\partial\varphi_2}\delta\varphi_2 = 0 \tag{4.2}$$

$$\begin{cases}\dfrac{\partial\bar{\Phi}}{\partial\varphi_1} = \varphi_1(1+\alpha) + 2\varphi_2 + \omega\left[\lambda + \left\{\varphi_1^2+\varphi_1\varphi_2+\varphi_2^2\right\}\right](2\varphi_1+\varphi_2) + \dfrac{1}{2}f_a\omega + \dfrac{1}{2}f_s\omega = 0 \\ \dfrac{\partial\bar{\Phi}}{\partial\varphi_2} = 2\varphi_1 + \varphi_2(1+\beta) + \omega\left[\lambda + \left\{\varphi_1^2+\varphi_1\varphi_2+\varphi_2^2\right\}\right](\varphi_1+2\varphi_2) - \dfrac{1}{2}f_s\omega = 0\end{cases} \tag{4.3}$$

By solving the equilibrium equations in (4.3), the pre-buckling solution $\mathbf{u}_0 = [0,0]^T$ for $\lambda \neq 0$ is obtained. This is a stable solution describing the state of the system prior to buckling for a pre-load λ increasing from zero, or the flat state from Figure 4.1a in short. The critical buckling loads and corresponding modes are obtained by evaluating the stability of $\mathbf{u}_0$ using the buckling condition in (4.4) [56]. $\bar{\Phi}_c''$ denotes the second derivatives of the dimensionless potential energy evaluated at the pre-buckling solution and the critical pre-load $\lambda = \lambda_c$, $\boldsymbol{\theta}$ denotes the buckling modes of the system. The buckling condition returns the generalized non-dimensional eigenvalue problem in (4.5). A trivial solution would be that $\boldsymbol{\theta} = \mathbf{0}$; however, this means that no buckling is occurring. Therefore, a non-trivial solution can only be found for a singular $\bar{\Phi}_c''$.

$$\bar{\Phi}''[\mathbf{u}_0(\lambda_c);\lambda_c] = \bar{\Phi}_c''\boldsymbol{\theta}\delta\mathbf{u} = 0 \tag{4.4}$$

$$\bar{\Phi}_c''\boldsymbol{\theta} = \left\{\begin{bmatrix}\alpha+1 & 2\\ 2 & \beta+1\end{bmatrix} + \mu\begin{bmatrix}2 & 1\\ 1 & 2\end{bmatrix}\right\}\begin{bmatrix}\theta_1\\ \theta_2\end{bmatrix} = \{A+\mu B\}\boldsymbol{\theta} = \mathbf{0} \tag{4.5}$$

Critical load matching

Solving (4.5) by setting $C = B^{-1}A$ returns the eigenvalues $\mu_i = \lambda_i\omega$ and eigenvectors $\boldsymbol{\theta}_i$, which represent the dimensionless critical buckling loads and corresponding modes respectively for $i = 1, 2$. The lowest value of μ_i is the first critical buckling load μ_1; the

second lowest is the second critical buckling load μ_2. The CLR for the TSL is defined as the ratio μ_1/μ_2 and can be found in (4.6). It is found that the CLR becomes unity for $\alpha = \beta = 3$, which means that the two buckling loads are exactly equal.

$$\frac{\mu_1}{\mu_2} = \frac{\alpha+\beta-\sqrt{\alpha^2-\alpha\beta+\beta^2-3(\alpha+\beta)+9}}{\alpha+\beta+\sqrt{\alpha^2-\alpha\beta+\beta^2-3(\alpha+\beta)+9}} \tag{4.6}$$

The CLR governs the values of the stiffness ratios α and β, and thus physically the relative stiffness of the torsion springs in the TSL. Hence, by varying the CLR, different linkage architectures are obtained. According to a unity CLR, α and β are constrained to $\alpha = \beta = \kappa$. Assuming symmetry in the TSL as $k_a = k_d = c^*$ and $k_b = k_c = c$, returns $k_a = k_d = 3c$ for $\kappa = 3$. Therefore, a unity CLR is obtained when the two outer springs are three times stiffer relative to the two inner springs. This architecture will be denoted as 3c-c-c-3c, in which c denotes the stiffness of the torsion springs and the hyphens denote the links between the springs. Four additional architectures $\kappa = \{2, 2.5, 3.5, 4\}$ are denoted as, c-c-c-c, 2c-c-c-2c, 4c-c-c-4c, 5c-c-c-5c respectively. By solving (4.3) for f_a and f_s respectively for a given displacement field, the symmetric and asymmetric FD characteristics of these five architectures are determined to analyze the effect of the CLR on the mechanical behavior.

Modal analysis

The TSL has two DoFs describing the deflection and its two buckling modes B and S. Expressed in the DoFs, it holds that $\varphi_1 = -\varphi_2$ for the B-mode, and $\varphi_1 = \varphi_2$ for the S-mode [52]. Inversely, it holds that any configuration of the linkage may be decomposed in buckling modes B and S (4.7). Here, the DoFs $\mathbf{u}$ are projected on a modal basis $\boldsymbol{\theta}$ spanned by the buckling modes B and S. For a given linkage configuration, the modes are scaled with their modal amplitudes m_B and m_S. Modal amplitudes are linked to the displacement using the mode participation χ. As opposed to the modal amplitude, which is solely the scaling of the mode, the participation represents the measure of contribution, e.g. $\chi_i = 1$ means that the linkage configuration is fully described by mode i, and it holds that $\sum_i^N \chi_i = 1$ [58].

$$\mathbf{u} = \begin{bmatrix}\varphi_1\\ \varphi_2\end{bmatrix} = \boldsymbol{\theta}\mathbf{m} = \begin{bmatrix}1 & 1\\ -1 & 1\end{bmatrix}\begin{bmatrix}m_\mathrm{B}\\ m_\mathrm{S}\end{bmatrix} \wedge \chi_i = \frac{|m_i|}{|m_\mathrm{B}+m_\mathrm{S}|} \tag{4.7}$$

Using this decomposition, the potential energy of the linkage under transversal deflection can be decomposed in strain energy contributions of the B and S-modes. The dimensionless strain energy $\bar{E}$ expressed in the modal basis can be found in (4.8). The strain energy contribution of each mode can be evaluated by scaling the modes separately and evaluating (4.8), which is schematically represented in Figure 4.3.

$$\bar{E}[\mathbf{m};\alpha;\beta] = \frac{1}{2}m_\mathrm{B}^2(\alpha+\beta-2) + \frac{1}{2}m_\mathrm{S}^2(\alpha+\beta+6) + m_\mathrm{B}m_\mathrm{S}(\alpha-\beta) \tag{4.8}$$

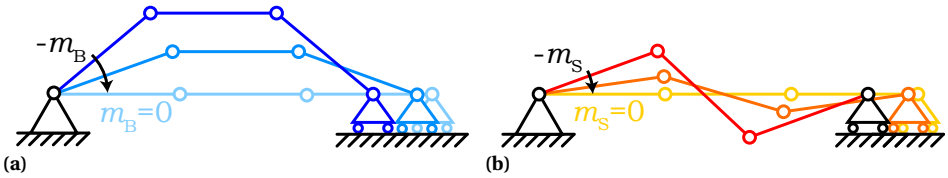

Figure 4.3: Schematic representation of linkage deformation using the buckling modes B (a) and S (b). From the buckled configuration, the modal amplitude is decreased until it reaches zero in the flat configuration

4.2.3 Mechanical design and manufacturing

The TSL in Figure 4.2 is converted into a lumped-compliant four-bar mechanism (CFBM) by replacing the torsion springs with flexures. In Figure 4.4a, the designed CFBM is depicted with the corresponding dimensions. It comprises three rigid links (1) of length B, width W and thickness H and two clamping blocks (2). Two flexures (3), representing the outer springs, of width w and thickness t connect the two outermost links to the clamping blocks, while two flexures (4), representing the inner springs, of width w_f and thickness t interconnect the links. The flexures are clamped to the links using a bolt connection and a cap (5), creating a fixed-fixed boundary and a flexure length l. The assembly is mounted on a base plate (6) provided with two slots (7) allowing for a variable pre-loading displacement d. The links and the clamping blocks are milled from aluminum. The flexures are manufactured from 0.20 mm thick AISI 301 spring steel using a Spectra Physics Talon 355-15 diode pumped solid-state (DPSS) UV laser cutter with a wavelength of 355 nm and a maximum power of 15 Watts at 50 kHz. The stiffness ratios κ from the five linkage architectures (Section 4.2.2) are achieved by varying the flexural rigidities of the inner flexures relative to the outer flexures. The flexural rigidity is determined as the product of torsion stiffness k_a, k_b, k_c, k_d and the flexure length [76]. For a constant flexure length and outer flexure width, the rigidities for the inner flexures (displayed in Figure 4.4a) are governed by w_f. The post-buckled state, e.g. the S-mode displayed in Figure 4.4b, is obtained by inducing a pre-loading displacement $d = 5$ mm. All parameters are summarized in Table 4.1.

Table 4.1: Relevant parameters of the manufactured lumped-compliant four-bar mechanisms

Fixed parameter	Symbol	Value [mm]
Link length	B	70
Link width	W	10
Link thickness	H	10
Outer flexure width	w	10
Flexure thickness	t	0.20
Flexure length	l	7
Pre-load displacement	d	5

CFBM architecture	Inner flexure width w_f [mm]
c-c-c-c	10
2c-c-c-2c	5
3c-c-c-3c	3.33
4c-c-c-4c	2.50
5c-c-c-5c	2

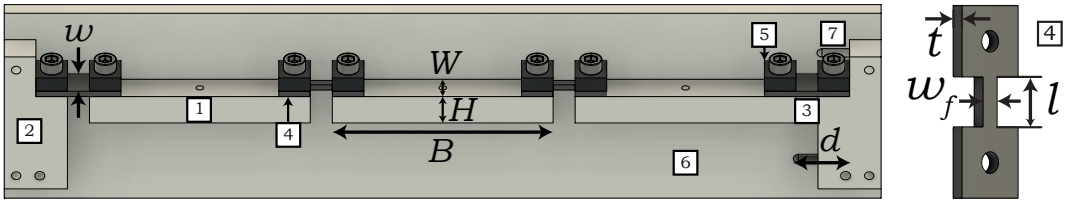

(a)

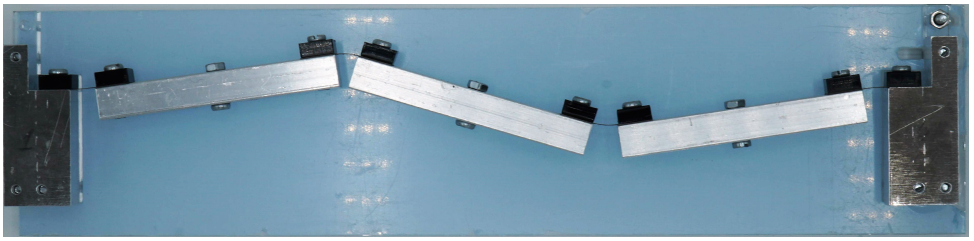

(b)

Figure 4.4: Designed lumped-compliant four-bar mechanism: (a) schematic showing the design of the unloaded mechanism and inner flexures with the dimensions indicated. The design comprises: rigid links (1), clamping blocks (2), outer flexures (3), inner flexures with variable width (4), PMMA caps (5), mounting base plate (6), pre-loading slots (7). By applying a pre-load the manufactured mechanism may buckle into the S-mode (b)

4.2.4 Finite element modeling

To simulate the mechanical behavior of the post-buckled CFBM architectures, a finite element model was constructed in ANSYS Mechanical APDL. The flexures are modeled as linear elastic ($E = 190\,\text{GPa}$, $\nu = 0.34$, $\rho = 7890\,\text{kg}\cdot\text{m}^{-3}$) two-node Timoshenko beam elements (BEAM188). A linear buckling analysis is performed to determine the first two buckling loads and the corresponding modes of the CFBM. To prevent crashing in the pre-loading phase due to singularities, an initial imperfection is added. The pre-loading displacement d is applied, and subsequently an incremental displacement is applied in either O_a or O_s, while recording the reaction force to obtain the FD characteristics for asymmetric and symmetric actuation.

4.2.5 Experimental setup

The FD characteristics of the mechanism architectures were evaluated experimentally with the setup shown in 4.5a. To apply the desired displacement to the mechanism, a PI M-505 motion stage with an internal encoder for the displacement data is used. The force required for applying the displacement to the mechanism is measured by a FUTEK LRM200 force sensor. A rolling point contact between the mechanism and force sensor is established using a probe with a bearing ball, attached to the sensor, and a spherical magnet, attached to the mechanism, as shown in Figure 4.5b. The magnet ensures that contact remains in the unstable region. Data was recorded using an NI USB-6008 in 100 steps with a resolution of 750 μm.

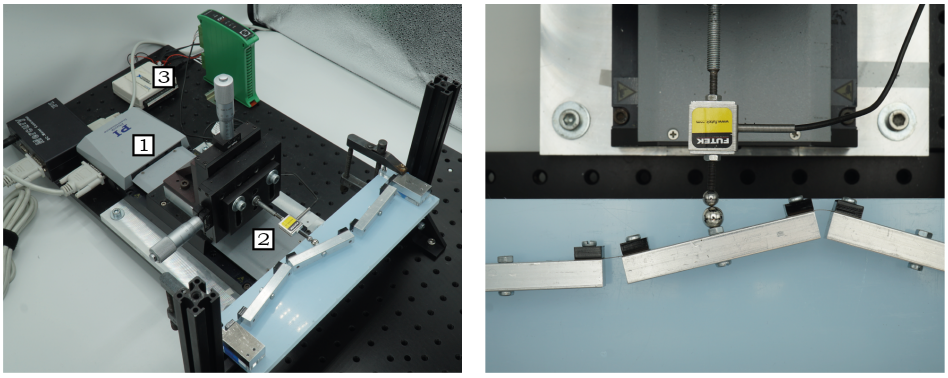

(a) **(b)**

Figure 4.5: Experimental setup for measuring force-deflection behavior. The used components (a) comprise a PI M-505 motion stage (1), a FUTEK LRM200 force sensor (2), and an NI USB-6008 data acquisition unit. A rolling contact (b) ensures that contact between the sensor and the mechanism remains in the unstable motion region

4.3 Results

The analytical buckling loads and the CLR values are tabulated in Table 4.2 for the five TSL architectures.

Table 4.2: Analytical buckling loads P_B and P_S and CLR values for analytical analysis

Architecture	P_B [N]	P_S [N]	CLR [-]
c-c-c-c	4.77	7.96	0.60
2c-c-c-2c	3.58	4.38	0.82
3c-c-c-3c	3.18	3.18	1.00
4c-c-c-4c	2.98	2.59	0.87
5c-c-c-5c	2.86	2.23	0.78

The FD characteristics of the TSL and CFBM architectures are depicted in Figures 4.6 and 4.7 for the symmetric and asymmetric actuation respectively. Analytical results are indicated with the dashed black line, finite element analysis (FEA) results with the red line, experimental results with the blue circles. The chronology of deflection is presented in Figures 4.8 and 4.9 for the symmetric and asymmetric actuation respectively. The numerals are indicated in the c-c-c-c Architecture FD characteristics at the corresponding locations.

Figure 4.10a depicts the relation between the mode participation of the B and S-modes and the vertical displacement of O_s under transversal deflection. The numerals correspond to the chronology of deflection in Figure 4.8. In Figures 4.10c, 4.10b and 4.10d, the dimensionless strain energy of the two separate modes is plotted together with their sum for the c-c-c-c, 3c-c-c-3c and 5c-c-c-5c Architectures for symmetric actuation.

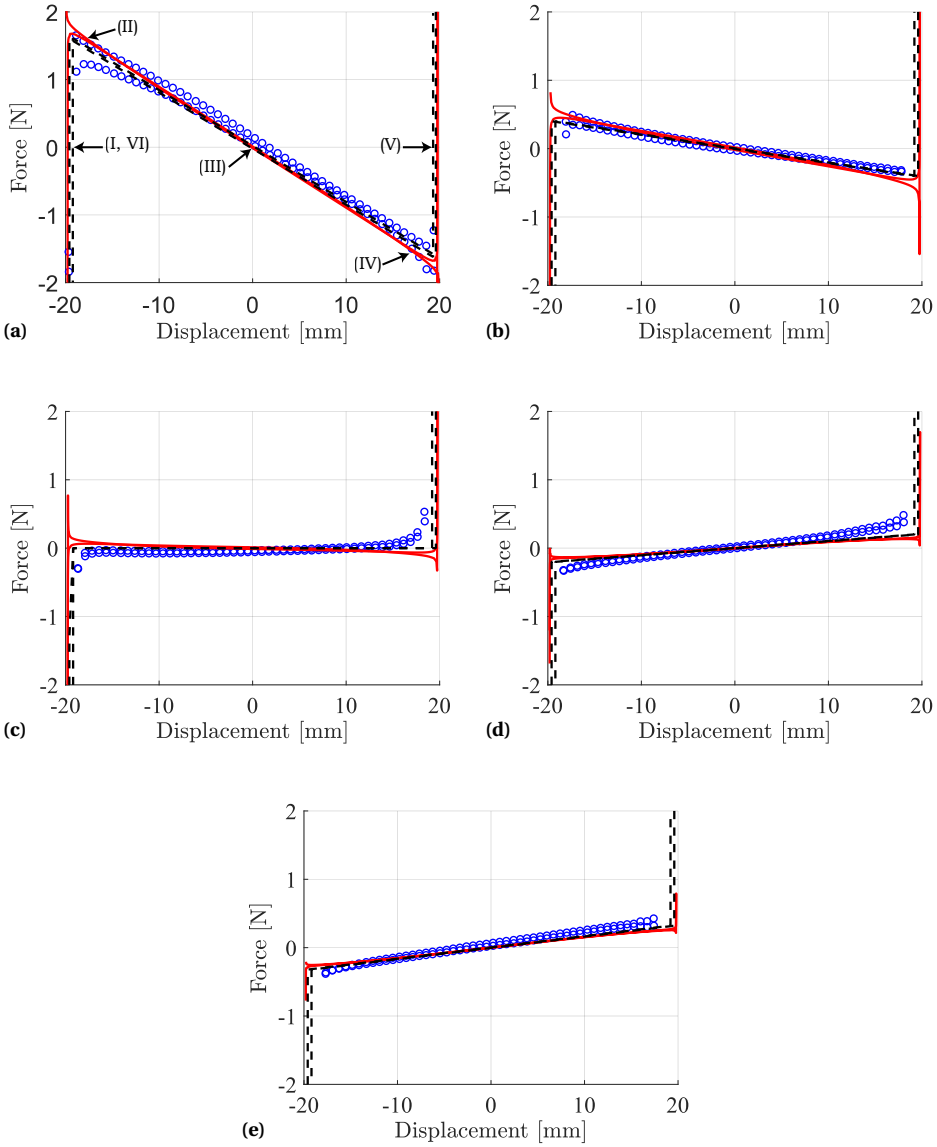

Figure 4.6: Comparison of analytical (●), FEA (●) and experimental (○) force-deflection behavior for symmetric actuation: (a) c-c-c-c, (b) 2c-c-c-2c, (c) 3c-c-c-3c, (d) 4c-c-c-4c, (e) 5c-c-c-5c

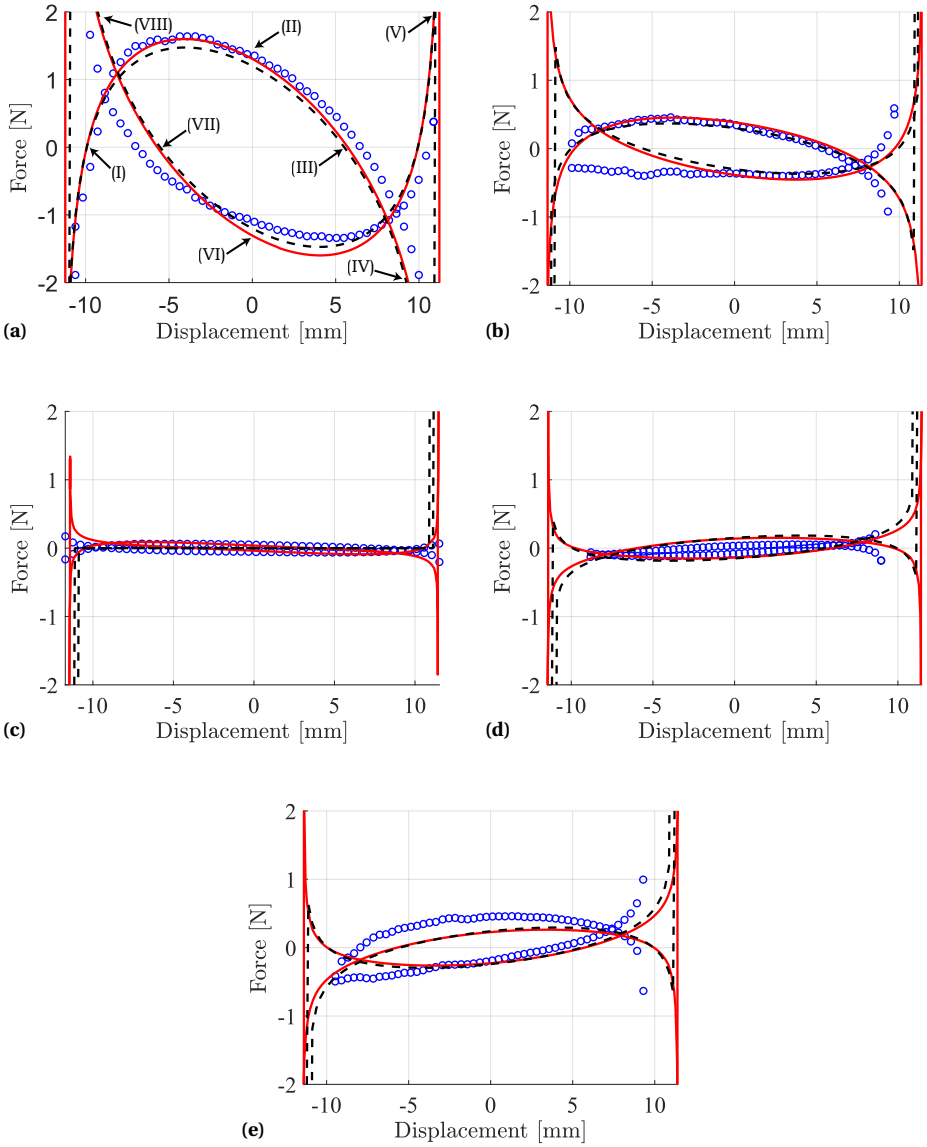

Figure 4.7: Comparison of analytical (●), FEA (●) and experimental (○) force-deflection behavior for asymmetric actuation: (a) c-c-c-c, (b) 2c-c-c-2c, (c) 3c-c-c-3c, (d) 4c-c-c-4c, (e) 5c-c-c-5c

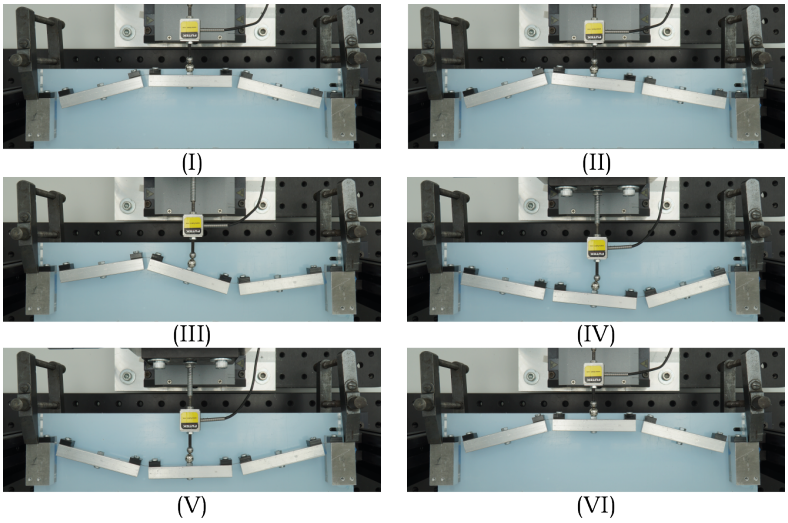

Figure 4.8: Chronology of mechanism deflection for symmetric load actuation (numerals refer to those in Figure 4.6)

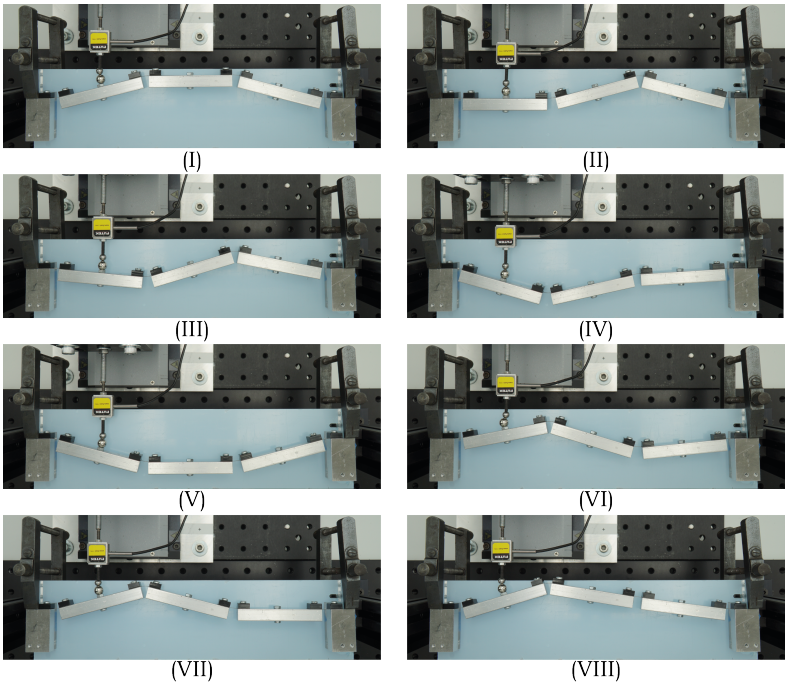

Figure 4.9: Chronology of mechanism deflection for asymmetric load actuation (numerals refer to those in Figure 4.7)

4.4 Discussion

4.4.1 Force-deflection characteristics of architectures

In both actuation cases, the same effect is observed due to a change in κ: there is a counter-clockwise rotation of the FD characteristic parts between the ends as κ, i.e. the torsion stiffness ratios, increases. As the κ increases from the c-c-c-c Architecture to the 3c-c-c-3c the stiffness gradually diminishes to zero. Looking into the CLR, it is observed that as the CLR approaches unity, the stiffness reduces. Static balancing is achieved in the mechanism as a result of matching the first two buckling loads in the 3c-c-c-3c Architecture. This strong reduction in stiffness matches the results found in [73, 74]. Therefore, it can be said that using the CLR is indeed a successful method for stiffness compensation of the mechanism applied to, and can return statically balanced behavior for a unity value. The same counter-clockwise rotation of the FD characteristics is found in [77] for a Von Mises truss with a spring attached to the middle joint. For an increase in spring stiffness, the slope of the FD transitions from negative, to perfectly flat, to positive. [78] obtained the same behavior for a Von Mises truss and denoted it as a zero-stiffness structure.

The change in sign of the FD slope for the 4c-c-c-4c and 5c-c-c-5c Architectures is ascribed to the buckling modes changing "order". Whereas the first buckling mode in the c-c-c-c Architecture is the B-mode, it becomes the S-mode for the 4c-c-c-4c and 5c-c-c-5c Architectures which is observed in Table 4.2. Architectures c-c-c-c to 3c-c-c-3c have the B-mode as two stable positions on either side of the motion range. The S-mode has a single stable position at the middle of the motion range. This results in the mechanism acting as a spring with positive stiffness.

The stiffness of the asymmetric FD characteristics may be approximated by taking the slope between the crossings of the loops, which is observed to follow the same trend as in the symmetric FD characteristics. It can also be observed that the area of the loops decreases as we approach the 3c-c-c-3c Architecture, matching the results in [74]. [79] quantified the area under this loop as the energy required for deformation; hence, the energy decreases as we approach the 3c-c-c-3c Architecture.

4.4.2 Decomposition of the strain energy

From Figure 4.10a, it can be observed that the configuration of the linkage in the equilibria is fully defined by a single mode. Hence, the strain energy in the equilibria is equivalent to that of the corresponding buckling mode, and determined by the pre-loading displacement and critical load, which corresponds to what was found in [74]. In the 3c-c-c-3c Architecture, the CLR is unity, and hence the three equilibria have equal strain energy. As a result, it is observed that two strain energy contributions sum to a constant value throughout the motion range. The obtained constant strain energy results in zero actuation force during transversal deflection of the 3c-c-c-3c Architecture. Hence, it can be said that by obtaining a unity CLR, the mechanism is statically balanced between its equilibrium positions.

The counter-clockwise rotation observed in the FD characteristics due to change in the mode order is depicted by the strain energy as well. Two equilibrium positions, both described by the B-mode, which are separated by a barrier that is defined by the S-mode

are found for the c-c-c-c Architecture (Figure 4.10c). The downward opening parabola indicates that the c-c-c-c Architecture exhibits bistable behavior, as is observed in Figure 4.6a. A single minimum of strain energy for $\chi_S = 1$ is observed for the 5c-c-c-5c Architecture, meaning that the stable equilibrium is fully described by S-mode (Figure 4.10d). The upward opening parabola indicates monostability, which is observed as the positive stiffness in Figure 4.7e.

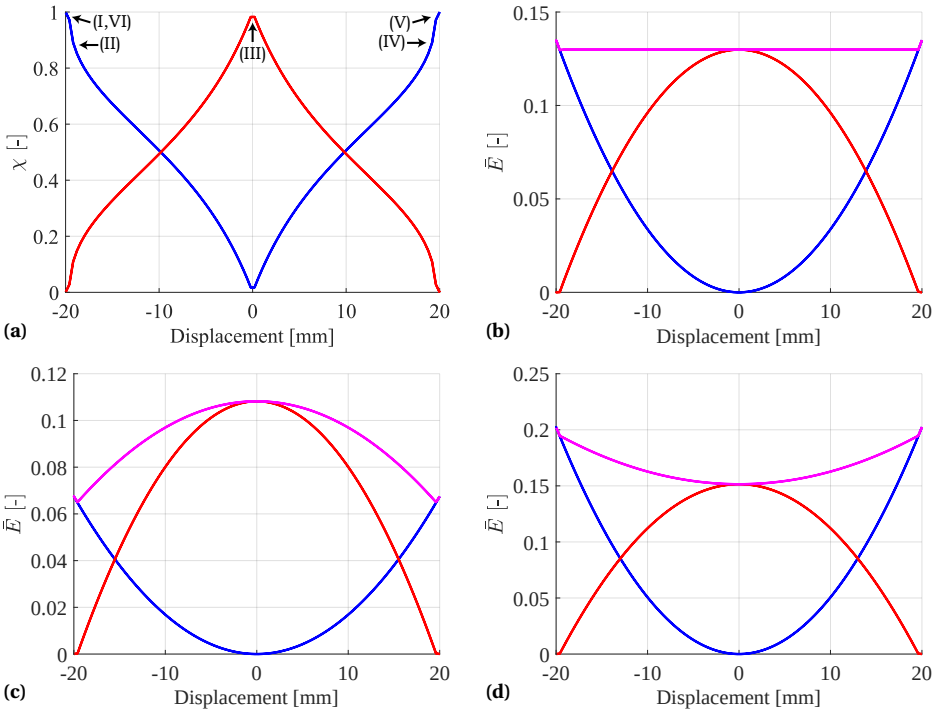

Figure 4.10: Relation between mode participation χ and displacement of O_s for modes B ● and S ● (a). The numerals correspond to the chronology of deflection in Figure 4.8, indicating the configuration of the linkage. The dimensionless strain energy $\bar{E}$ for each mode is plotted separately together with the sum of both contributions ● for the 3c-c-c-3c (b), c-c-c-c (b) and 5c-c-c-5c (d) Architectures

4.4.3 Accuracy of model

From Figures 4.6 and 4.7 it is observed that the analytical model and the experimental results comply well in terms of stiffness. The moderate rotations assumption introduces a slight error to the kinematics that remains within a 2% bound. From Figure 4.9 it can be observed that the asymmetric actuation results in two load paths occurring. The shapes of the FD characteristics of the c-c-c-c Architecture match those found for symmetric and asymmetric actuation of a bistable buckled prismatic beam [80]. Therefore, it can be said that the proposed analytical model predicts the behavior of such a beam well.

In symmetric actuation of the 3c-c-c-3c Architecture, a discrepancy between the stiffness in the experimental and the analytical results is observed. Due to imperfections in the assembly process, the pivot length is not exactly 7 mm, and the actual stiffness distribution is 3.01c-1.03c-1.07c-2.98c, given that the mechanism is perfectly in plane. The finite element FD characteristics are simulated with these pivot length imperfections. Nevertheless, a discrepancy between the FEA and experimental results is still observed. This indicates the difficulty of achieving static balancing in practice due to the sensitivity of the buckling loads to manufacturing and assembly.

4.5 Conclusion

In this paper, we have investigated the effect of matching the first two buckling loads on the force-deflection characteristics in a four-bar linkage. An analytical simply supported four-bar linkage model consisting of three rigid links, four torsion springs in the joints and a linear spring capturing the buckling behavior was proposed to achieve this. The buckling problem was solved and it was found that the ratio between the buckling loads changes as a function of the torsion stiffness ratios in the linkage. The first two buckling loads are exactly equal when the two outer springs are three times stiffer than the two inner springs. The force-deflection characteristics of five linkage architectures with the torsion spring stiffness ratio ranging from 1 to 5 were evaluated analytically, numerically using finite element analysis and experimentally. In the finite element and experimental models, the torsion springs were replaced by short flexures, creating a lumped-compliant four-bar mechanism. It was shown that by matching the first two buckling loads, the force required for deformation entirely diminishes and static balancing is achieved. Using modal analysis, it was shown that the sum of the decomposed strain energy per buckling mode is constant throughout the motion range due to the matching buckling loads. This indicates that matching the first two buckling loads is a useful method in stiffness compensation or static balancing of buckled lumped-compliant four-bar mechanisms.

Chapter 5
Effect of matching buckling loads on post-buckling behavior in compliant mechanisms

This chapter presents the research paper on the use of the stiffness compensation method described in Chapter 4. The method is applied to two compliant mechanism architectures and a parametric study of changes in the geometry is conducted. By changing the relative width and length of flexures in the architectures, the ratio between the first two buckling loads, called the critical load ratio, is adjusted. A finite element model is constructed and the force-deflection characteristics of different architecture designs are simulated to investigate the effect of the critical load ratio on the mechanical behavior. The results are subsequently experimentally validated.

Effect of matching buckling loads on post-buckling behavior in compliant mechanisms

A. Numić, T.W.A. Blad and F. van Keulen

Abstract
In this paper, a novel method for stiffness compensation in compliant mechanisms is investigated. This method involves tuning the ratio between the first two critical buckling loads. To this end, the relative length and width of flexures in two architectures, a parallel guidance and stepped beam, are adjusted. Using finite element analysis, it is shown that by maximizing this ratio, the actuation force for transversal deflection in post-buckling is reduced. These results were validated experimentally by identifying the optimal designs in a given space and capturing the force-deflection characteristics of these mechanisms.

Keywords
Static balancing, stiffness compensation, buckling, compliant mechanisms

5.1 Introduction

Compliant mechanisms (CMs) allow motion through the deflection of elastic members. These mechanisms are widely used due to their ease of manufacturing, increased precision and reliability, and wear resistance, as compared to non-compliant counterparts. Despite these advantages, a great disadvantage is the significant storing of input energy in the form of strain energy in the elastic members [81]. As a result, the available travel range and mechanical efficiency are reduced, and the natural frequency is significantly increased [64].

This strain energy is not dissipated and can be balanced out by adding new strain energy into the system, e.g. through pre-stress [64, 82]. A system in which the elastic potential energy is kept constant over a finite motion range is called statically balanced; hence, the system is in a neutrally stable equilibrium throughout this motion range [8]. This range is bounded by a steep increase in the potential energy due to the elastic elements being loaded in tension. In the force-deflection characteristic, this translates to a plateau that rapidly steepens at either end. Ideally, the actuation force and stiffness of a statically balanced mechanism approach zero [69].

Examples of statically balanced compliant mechanisms (SBCMs) can be found for use in micro mechanisms [68, 69], haptic interfaces [67, 83], surgical equipment[84, 85]. Additionally, SBCMs may find application in energy harvesting devices and linear bearings [70]. Statically balanced behavior in the given examples is obtained through intricate design, synthesis of pre-stressed and unstressed compliant elements, and optimization steps. These steps have been incorporated in building blocks to generalize the process of static balancing [71, 82, 86]. Kuppens e.a. [73] presented a novel notion in static balancing of CMs. In this work, the stiffness of a parallel guidance connected to a buckled flexure is minimized by matching the first two buckling loads. Blad e.a [74] proposed the critical load ratio (CLR), i.e. the ratio between the first two buckling loads, to identify the variation of potential energy between the equilibria of a buckled mechanism. This strategy was applied as a design method to statically balance several compliant orthoplanar mechanism architectures by maximizing the CLR. To date, this method has only been applied to these orthoplanar mechanism architectures.

The goal of this paper is to investigate the effect of the CLR on the force-deflection characteristics of two CM architectures, namely a stepped beam and the parallel guidance from [73].

In Section 5.2, the model of the two architectures is presented. Additionally, manufacturing, finite element modeling and the experimental setup are discussed. Section 5.3 presents the results obtained from the finite element analysis (FEA) and the experiments. The results are discussed in Section 5.4 and conclusions are drawn in Section 5.5.

5.2 Methods

5.2.1 Critical buckling load ratio

A minimal stiffness in a CM can be achieved by matching the first two critical buckling loads [73]. The first critical buckling load, $P_{cr,1}$, is the lowest axial load at which a mechanism loses its stability and bifurcates into a new equilibrium: the first buckling mode. This mode describes the stable equilibrium configuration of the mechanism, i.e. the minimum of potential energy. The second buckling load corresponds to the second buckling mode, and it holds that $P_{cr,2} > P_{cr,1}$ [52, 53]. Higher buckling modes describe equilibrium configurations as well, though unstable [87].

By adjusting the geometry of the mechanism, the values of these buckling loads change; more importantly, the ratio between the buckling loads, CLR = $P_{cr,1}/P_{cr,2}$, changes. The CLR describes the variation in potential (or strain) energy between the equilibrium configurations. The strain energy E_i of buckling mode i, is equivalent to the input energy required to obtain the deformation corresponding to the mode. This input energy is approximately the work done by the corresponding buckling load over the imposed pre-loading displacement d: $E_i \approx P_{cr,i}d$. For a unity CLR, it holds that $P_{cr,1} = P_{cr,2}$ and hence $E_1 = E_2$. Therefore, there is no variation in potential energy between the equilibrium configurations and static balancing is achieved [74].

A physical visualization of this effect can be achieved by means of the force-deflection (FD) characteristics. FD characteristics with a single load path and two load paths are displayed in Figures 5.1a and 5.1b respectively. For the single load path, a linear stiffness k between the ends of the FD characteristic can be evaluated. This stiffness ideally goes to zero when static balancing is achieved [69]. For the two load paths, the stiffness may be evaluated between the crossings of the load paths. Alternatively, Cazottes e.a. [79] proposed the snapping energy E_s, i.e. the energy required for deformation, as the area between each load path and the horizontal axis. The linear stiffness and snapping energy will be used to quantify the effect of the CLR on the FD characteristics.

In the current work, the FD characteristics in post-buckling of two architectures are investigated. The first architecture comprises a shuttle suspended by two flexures on either side creating a stepped beam; hence, it is named Buckled Stepped Beam (BSB). In the second architecture, a third flexure is added to constrain the rotation of the shuttle creating a parallel guidance; hence, it is named Buckled Parallel Guidance (BPG). The first and second buckling modes of the BSB and BPG are displayed in Figure 5.2. The geometry in both architectures is tuned by means of parameters β and σ, which denote the relative length and width of the flexures.

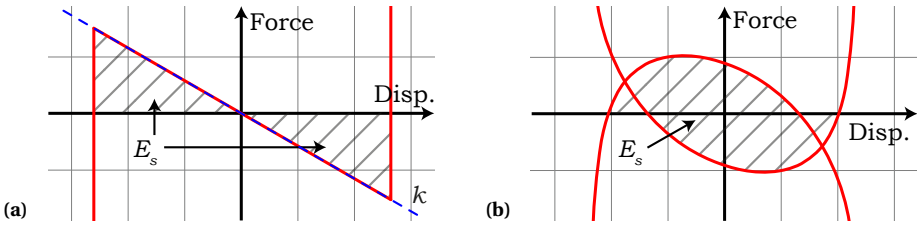

Figure 5.1: Force-deflection characteristics with a single load path (a) and two load paths (b). For the single load path, a linear stiffness k between the steep ends can be evaluated. For the two load paths (as well as for the single load path) the energy for deformation can be evaluated as the area between the load paths and the horizontal axis

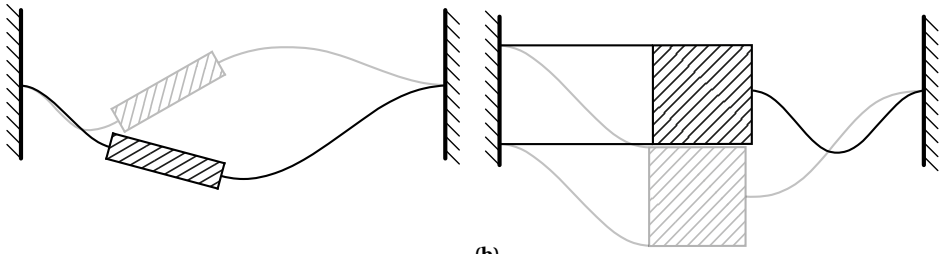

Figure 5.2: First two buckling modes of Buckled Stepped Beam (a) and Buckled Parallel Guidance (b) Architectures

5.2.2 Mechanical design

The two architectures are displayed in Figure 5.3. Both architectures consist of flexures (indicated in dark and light gray) and a shuttle connecting these (indicated in tan). The dimensions of the shuttle, length l, width h, thickness b, as well as the flexure thickness t, are kept constant throughout the analysis for both architectures. The length L and width w of the dark gray, henceforth called unchanging, flexures are kept constant. For the light gray, henceforth called variable, flexures, the length and width are defined relative to L and w using parameters β and σ respectively. Both architectures are brought into post-buckling by imposing an axial displacement d onto the side of the variable flexure.

5.2.3 Manufacturing

Both architectures are incorporated in the assembly in Figure 5.3. This consists of a frame milled from aluminum and 3D-printed shuttles on which the flexures are clamped using a bolt connection. The fixed dimensions are set to: $l = 25\,\text{mm}$, $h = 20\,\text{mm}$, $L = 50\,\text{mm}$, $w = 20\,\text{mm}$. The flexures are manufactured using a laser cutting process from $t = 0.20\text{mm}$ thick AISI 301 stainless steel. By tightening the bolt on the side of the variable flexure, the axial displacement of $d = 2\,\text{mm}$ is imposed and the mechanism is brought into post-buckling. The designs chosen for both architectures are tabulated in Table 5.1 in terms of β and σ.

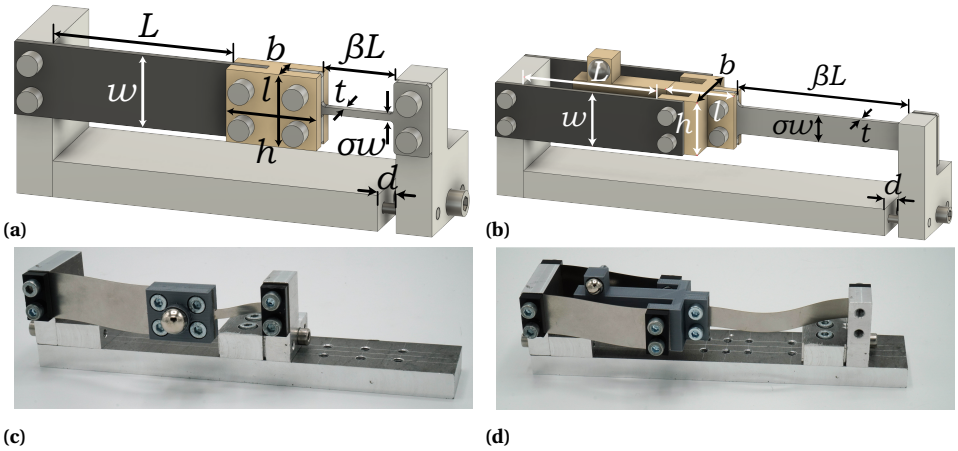

Figure 5.3: Buckled Stepped Beam (BSB) (a) and Buckled Parallel Guidance (BPG) (b) mechanism architectures. The unchanging flexures are indicated in dark gray; the shuttles are indicated in tan; the variable flexures are indicated in light gray. β and σ denote the relative length and width of the flexures respectively. Both assemblies are brought into post-buckling by imposing a displacement d giving the buckled manufactured architectures: (c) BSB and (d) BPG

Table 5.1: Chosen designs for both architectures in terms of β and σ

Design	I(β,σ)	II(β,σ)	III(β,σ)	IV(β,σ)	IV(β,σ)
BSB	(0.40, 0.20)	(0.40, 0.10)	(0.40, 0.30)	(0.60, 0.20)	-
BPG	(1.3, 0.50)	(1.3, 0.40)	(1.3, 0.60)	(1.6, 0.50)	(1.0, 0.50)

5.2.4 Experimental setup

The FD behavior of the manufactured mechanisms was experimentally evaluated with the setup shown in Figure 5.4a. The force is measured using a FUTEK LRM200 force sensor (1). The mechanism is deflected using a PI M-505 motion stage (2) with an internal encoder to capture the displacement. All data is recorded using an NI USB-6008 acquisition unit (3) in 100 steps with a resolution of 350 μm. Connection between the force sensor and the mechanism is established, and ensured in the unstable region, using a rolling contact and a ball magnet as seen in Figure 5.4b.

5.2.5 Finite element modeling

The CLR is obtained by developing a finite element model for both architectures and conducting a linear buckling analysis. The models are created in ANSYS Mechanical APDL using two-node Timoshenko beam elements (BEAM188) for the flexures. The flexure are modeled as linear elastic ($E = 190$ GPa, $\nu = 0.34$, $\rho = 7890\,\mathrm{kg}\cdot\mathrm{m}^{-3}$). The CLR is evaluated for β and σ in 50 steps each, resulting in a grid of 2500 designs. For the manufactured mechanisms, the FD behavior is simulated. The designs are brought into post-buckling by applying an axial displacement d. After obtaining the buckled geometry, a displacement in y-direction (see Figure 5.3) is applied to the shuttle. In the BPG, the displacement is applied in the center of compliance to ensure there is no rotation of the shuttle relative to the displacement [88]. In the BSB, this rotation is inherent to the de-

flection; therefore, the displacement is applied at the middle of the shuttle. The reaction force arising due to the imposed displacement is measured back and forth to obtain the force-deflection behavior for each design.

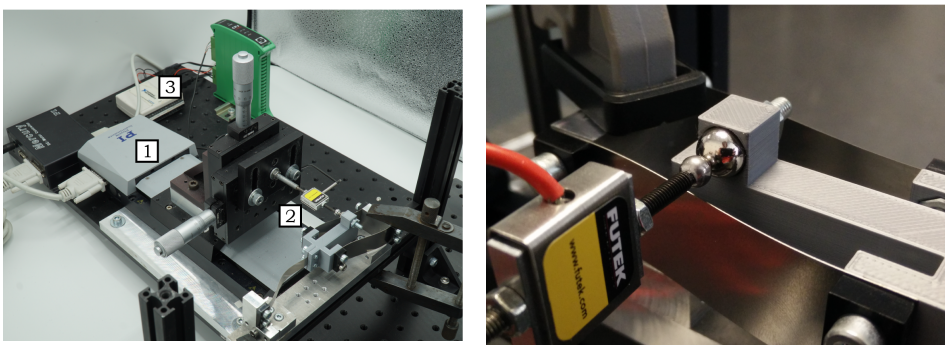

(a) (b)

Figure 5.4: Experimental setup used for measuring force-deflection behavior: (a) overview of components, (b) rolling contact used to ensure contact in unstable region

5.3 Results

The obtained CLR values for different variations of β and σ for both architectures are displayed in Figure 5.5. The designs from Table 5.1 are indicated in the surfaces with the colored dots.

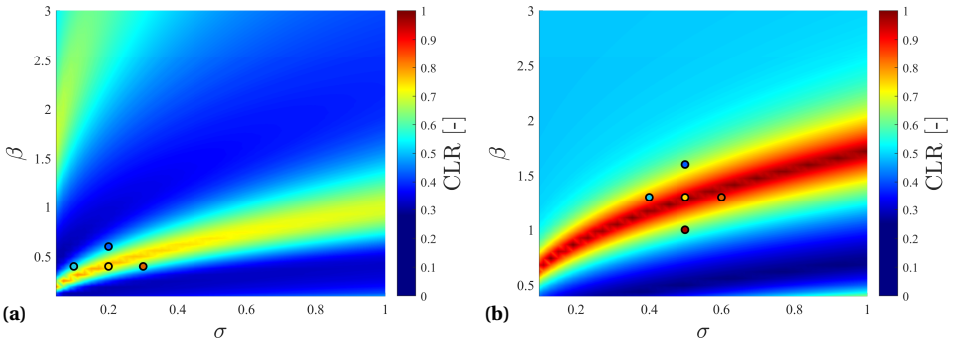

Figure 5.5: Critical load ratio (CLR) surface plot to β and σ for the Buckled Stepped Beam (a) and Buckled Parallel Guidance (b) Architectures. The surface plot displays the CLR for variations of β and σ and acts as a space from which mechanism designs can be chosen. The designs from Table 5.1 are indicated by the colored dots: I( ), II( ), III( ), IV( ), V( )

Figure 5.6 displays the FD behavior obtained from the FEA for the chosen designs of both architectures. It can be observed that Design I requires the least force for deformation. The energy required for the deflection E_s for the BSB, and the linear stiffness k for the BPG are tabulated in Table 5.2.

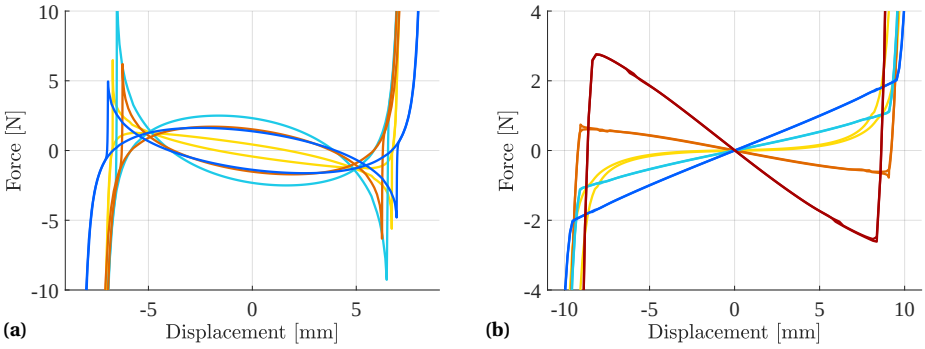

Figure 5.6: Force-deflection behavior of sample points in Buckled Stepped Beam (a) and Buckled Parallel Guidance (b) Architectures for Designs I( ), II( ), III( ), IV( ), V( )

Table 5.2: Quantification of force-deflection behavior for both architectures. The snapping energy E_s corresponds to the Buckled Stepped Beam; the linear stiffness k corresponds to the Buckled Parallel Guidance

Design		I	II	III	IV	V
BSB	E_s [mJ]	14	25	36	25	-
BPG	k [N mm^{-1}]	0.029	-0.064	0.12	0.21	-0.39

Figures 5.8 and 5.7 display a comparison of the FEA and experimental FD results. The experimental results comply with the simulation results, validating the finite element model.

5.4 Discussion

5.4.1 Critical load ratio surfaces

The CLR surfaces in Figure 5.5, act as a design space for the mechanisms of both architectures. It can be observed that for both architectures, there exist a narrow band in which the CLR is largest, of which on either side the CLR decreases. For the BSB, the largest CLR is confined to a domain $(0.3 \leq \beta \leq 0.7; 0.1 \leq \sigma \leq 0.5)$. On either side of this band, the CLR drops to $0.30-0.40$. For the BPG, this band stretches along the entire chosen design domain. By increasing β, the CLR settles around $0.50-0.60$; whereas it drops to $0.20-0.30$ for a decrease in β. In contrast to the BSB, a CLR near unity is observed throughout the entire band for the BPG.

5.4.2 Effect of critical load ratio on force-deflection behavior

From Figures 5.6a and 5.8, it can be observed that the least actuation force is obtained for Design I. This is evident from the FD characteristic becoming close to zero and nearly flat ($k = 0.029$ [N/mm]), approaching statically balanced behavior [86]. A CLR = 0.97 is found; hence it can be said that by matching the first two buckling loads, the mechanism is statically balanced. Increasing β from Design V to IV, passing I, results in a counter-clockwise rotation of the FD curves. Contrariwise, increasing σ from Design II to III results in a clockwise rotation of the FD curves. Hence, Designs III and V exhibit

bistable behavior due to the negative stiffness. Designs II and IV return a monostable mechanism with positive stiffness. Comparing the stiffness values between the steep ends of the FD curve ends in Figure 5.6a shows that an increase in CLR results in a decrease of the absolute stiffness. Hence, it can be said that the CLR is a suitable method for stiffness compensation, and achieving static balancing, in compliant parallel guidance mechanisms.

Buckled Stepped Beam Architecture

For the BSB, Figures 5.6b and 5.7 show two different load paths, indicating snap-through behavior [79, 80]. Evaluating the stiffness between the load path crossings does not return significant differences between the four designs. A more insightful result of the increase in CLR is observed for the snapping energy. In Table 5.2, this energy is found to be the lowest for Design I, which has the highest CLR. This can be observed from the FD characteristic of Design I as well, as the distance between its load paths is significantly smaller relative to the other three designs. Furthermore, it is observed that the maximum force of the load paths, the limit load, is the least for Design I. However, it cannot be concluded that any increase in CLR returns lower snapping energy and limit loads for the BSB. Upon comparison of Deign II to Designs III and IV, it can be observed that despite the higher CLR, the snapping energy is significantly greater. In the BSB, it is not possible to match the two buckling loads given the boundary conditions.

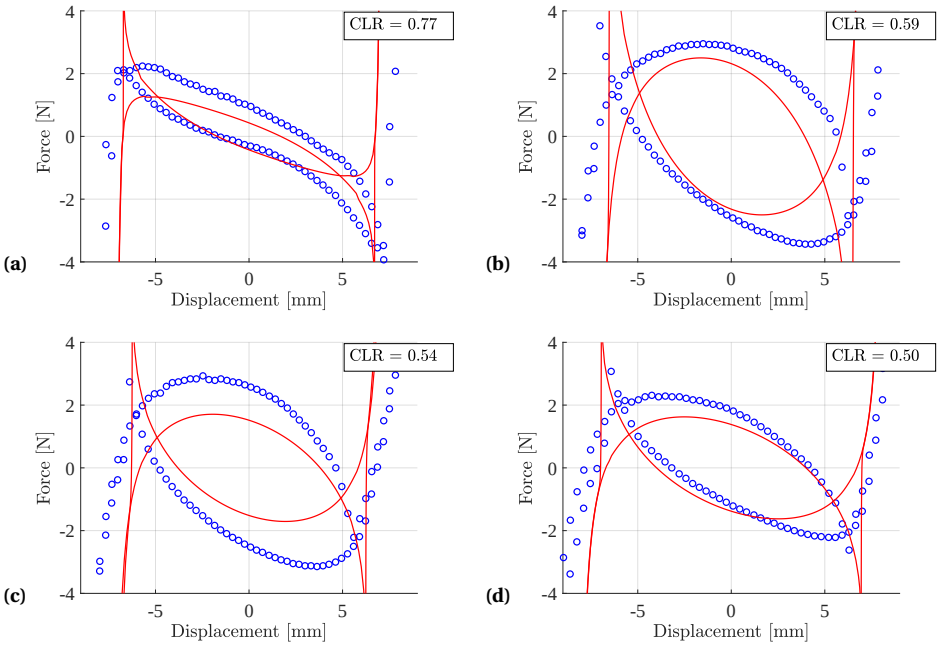

Figure 5.7: Comparison of FEA (●) and experimental (○) force-deflection behavior for the Buckled Stepped Beam: (a) I, (b) II, (c) III, (d) IV

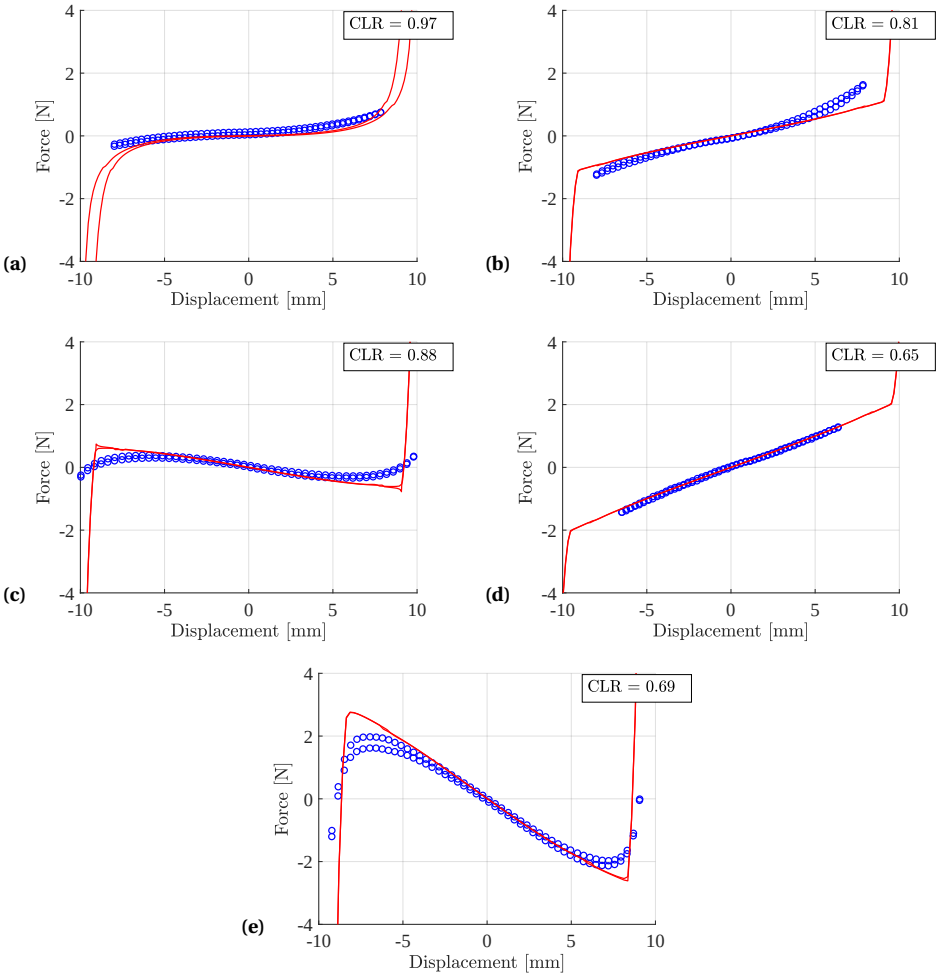

Figure 5.8: Comparison of FEA (●) and experimental (○) force-deflection behavior for the Buckled Parallel Guidance: (a) I, (b) II, (c) III, (d) IV, (e) V

5.5 Conclusion

In this work, the effect of matching the first two buckling loads on the mechanical behavior is investigated for two compliant mechanisms architectures. By changing the relative length and width of the flexures in said architectures, the ratio between the first two critical loads is tuned. Maximizing this ratio for a certain architecture returns a minimal actuation force in post-buckling, which is shown through finite element analysis and experiments. For a parallel guidance mechanism, an increase in this ratio results in a decrease of absolute stiffness between the steep ends of the force-deflection characteristic. The ratio may approach unity, resulting in a nearly zero and flat actuation force. In a stepped beam architecture, a unity ratio is not obtainable; however, maximizing it reduces the distance between load paths in the force-deflection characteristic and therewith the energy required for moving between equilibrium positions. These results indicate that the critical buckling load ratio is a useful method for stiffness compensation in compliant mechanism and may be used to achieve static balancing.

Chapter 6
Reflection, conclusions and recommendations

This chapter serves the purpose of concluding the graduation project. A schematic overview of the research activities is presented, together with a reflection on several attempts in this project, both successful and unsuccessful. Subsequently, the conclusions resulting from the research papers are listed and recommendations for further research regarding the topics in this thesis are given.

6.1 Overview of research activities

An overview of the research activities is given in Figure 6.1. In total, the graduation spanned a period of 15 months, starting from October 1st 2019 to January 22nd 2021. In this period, three research papers were written and three prototypes were designed and tested. Additionally, a novel concept in the field of stiffness compensation, or static balancing, was thoroughly tested and investigated, resulting in a foundation for this concept to stand on.

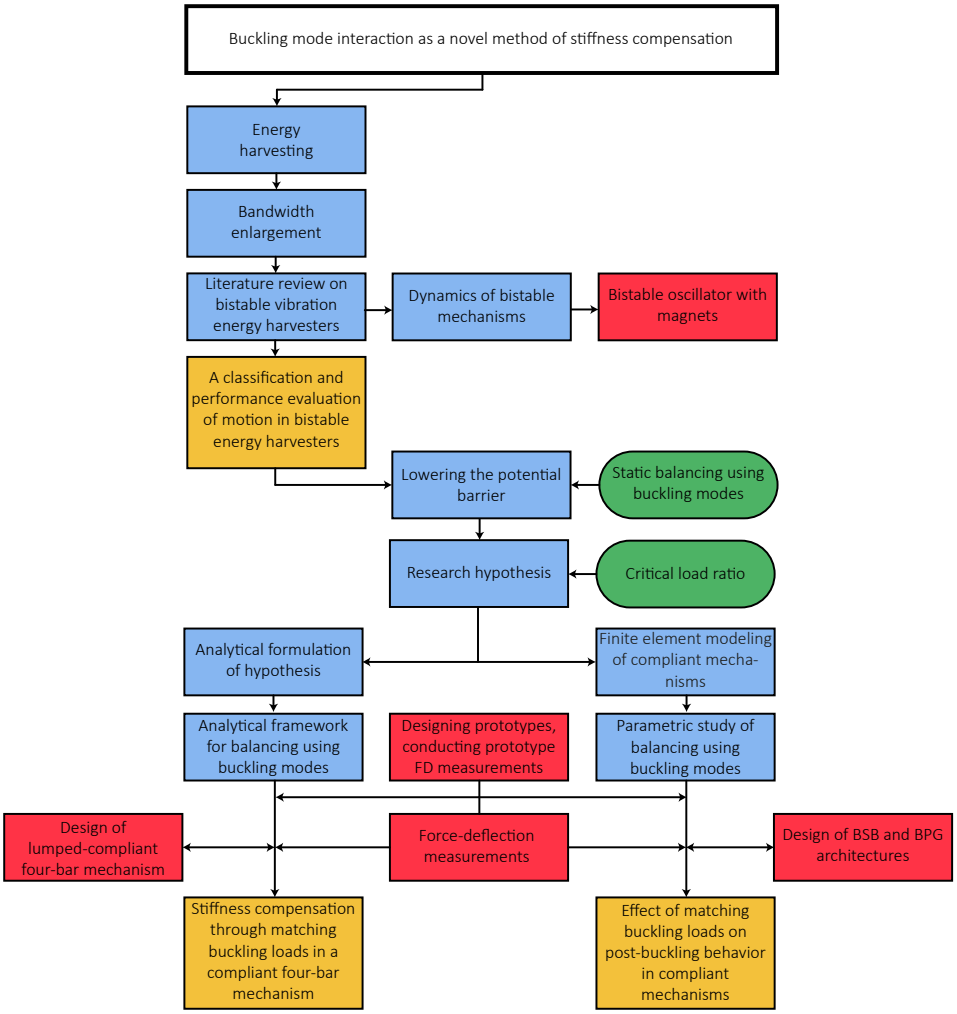

Figure 6.1: Schematic overview of research activities. Blue blocks indicate a main part of the research from which a research paper or experiments have followed. The practical work, i.e. designing/manufacturing and experiments, are indicated by the red blocks. Yellow blocks indicate the resulting research papers, and green indicates new concepts published during the course of this thesis that contributed to the current work

6.2 Reflection

6.2.1 Dynamics of bistable mechanisms

Following the line of the literature review, dynamics of bistable mechanisms were investigated with the use of several works on simulation of these mechanisms and the prototyping of a bistable oscillator using magnets. A seeming shift in the equilibrium positions under harmonic excitation was erroneously related to a finding in literature describing the influence of harmonic oscillations on the potential energy function [89]. This was experimentally evaluated and found to be an error in the simulation. It was chosen not to continue with this topic; however, despite the failure, this served as a good opportunity to get acquainted with the test setups in the lab. Additionally, attempts in finite element simulation of bistable mechanisms for dynamic analysis were made. Due to the complexity of simulation, and frankly the lack of knowledge on this topic, it was chosen not to continue with these simulations.

A vast amount of time and effort went into the classification of bistable mechanism dynamics in the literature review. In search for a parameter discerning all types of motion clearly, which was proposed as the 'motion rate of change' in Chapter 2, it was concluded that the literature review was likely to become a research. In view of time, it was decided to conclude the literature review and focus on defining the further research.

6.2.2 Finite element modeling

During the course of this thesis, finite element modeling was used extensively to gain insight in the mechanical behavior, or to test an interesting idea quickly. However, a great deal of effort went into comprehending ANSYS Mechanical APDL, until it was possible to quickly harvest useful results. Of course, this effort greatly repaid itself in later stages of the project with the accurate representation of the mechanical behavior for the constructed prototypes. Frequent discussion with my supervisor Thijs Blad resulted in an ongoing generation of knowledge on the use of ANSYS and development of more robust scripts.

6.2.3 Analytical framework

The strength of this work lies in the analytical framework used to describe the problem and test the hypothesis in Chapter 3. Compared to a finite element simulation, it was experienced that it is easier to continue with complex methods than it is to find a simple model that does the same. Several iterations of modeling were required to establish the torsion spring linkage model in Chapter 4. Eventually, this model resulted in a verification of the hypothesis and even lent itself as a good approximation of a continuous form of a bistable buckled beam. Along with these modeling iterations, different steps in search of an explanation of the observed behavior, which can be found in Appendix B, were conducted. Unfortunately, some steps were less useful than others; however, they are still included to give an overview of the different possibilities in this analysis.

6.2.4 Practical work

The statement *"If my measurements go well today, I will be done in no time"*, has probably been said far more often than this actually occurring. During the project, a number of prototype experiments (Appendices A and C) were conducted as a practical verification of the hypothesis, prior to the final experiments (Chapters 4 and 5). These prototype experiments eventually resulted in trying to single out all factors that negatively influenced the measurements. The experiments were repeated to identify problems in the equipment, different methods were used for comparison of results, and prototypes were improved. Finally, three prototypes were manufactured from aluminum and steel, as to have designs that can be used by others in future research. Considering the little experience in manufacturing, consisting of first-year instructions on milling and lathing, this was a challenge, but nonetheless a satisfying one.

6.3 Conclusions

Bistable energy harvesters are widely studied due to the increased performance and robustness as compared to linear systems. These traits require bistable harvesters to exhibit continuous interwell motion, which coexists with several other types of motion. A general classification of the possible types of motion, based on displacement time-series, is presented. This creates a uniform terminology that is applicable to the field of bistable energy harvesting systems, enabling performance comparison of certain motion types, or harvesting systems exhibiting the same motion. The performance of different motions is evaluated and it was found that continuous interwell motion returns the best performance, followed by chaotic crosswell motion. Furthermore, the share of interwell motion does not contribute to the power output as much as the overall amplitude does. Based on this, it was concluded that in order to have a bistable energy harvester excel at performance, it is necessary to have continuous interwell motion. This is possible by lowering the potential energy barrier using stiffness compensation methods.

During this project, [73] published their work on stiffness compensation in a compliant mechanism. In this work, it was mentioned that the stiffness of the mechanism is minimized by making the loads of the first two buckling modes equal to each other. This phenomenon was related to a simply supported bistable buckled beam to have a clear understanding of these buckling modes and formulated as the hypothesis *"Buckling mode interaction can be used as a method for stiffness compensation"*. The simply supported beam was discretized to obtain a simple, yet effective model to investigate this concept. This discretized model is a four-bar linkage consisting of three links, four torsion springs in the joints and a linear spring capturing the buckling behavior. It was found that the values of the buckling loads are governed by the ratios between the stiffness of the torsion springs. The first two buckling loads were found to be exactly equal for the outer springs being three times stiffer than the inner springs. The stiffness of this linkage was evaluated by making the linkage buckle; imposing a transversal displacement in the middle of the middle and one outer link respectively; and recording the reaction force for this deflection. By changing the torsion stiffness ratios, the overall stiffness of the linkage changes, ranging from initially negative to positive. Upon the two buckling loads being equal, the overall stiffness of the linkage diminishes to zero,

resulting in a flat force-deflection characteristic. By projecting the analytical description onto a basis spanned by the two buckling modes, the potential energy of the linkage was decomposed in contribution of each mode. It was found that by matching the buckling loads, the potential energy becomes constant over the range of motion. Hence, it was concluded that interaction of the buckling modes can indeed be used for stiffness compensation, and static balancing is achieved for matching the two buckling loads. The analytical four-bar linkage was converted into a lumped-compliant four-bar mechanism with flexures for the torsion springs and the behavior found analytically was verified experimentally.

The ratio between the first two buckling loads, named the critical load ratio, was proposed in [74] as a quantification to this method during the development of the analytical model. This ratio was used as a design tool to obtain several designs of two compliant mechanisms architectures. It was shown that by adjusting the critical load ratio, the overall stiffness, or the energy required for deformation, of the mechanisms changes. Obtaining a unity critical load ratio, i.e. matching the two buckling loads, results in static balancing; hence, verifying the hypothesis a second time. Such significant stiffness compensation was not obtainable in both architectures though, indicating the limitations of this method as well.

All in all, it is concluded that buckling mode interaction is indeed a suitable method for stiffness compensation in mechanisms. By adjusting the ratio between the first two buckling modes, the stiffness can be adjusted and static balancing may be achieved, depending on the mechanism in question. This work is an addition to the existing methods in this field of work and paves the way for further development and design of new stiffness compensated mechanisms.

6.4 Recommendations

The term 'stiffness compensation' was purposefully used in this work instead of static balancing. It has not only been shown that matching the buckling loads results in static balancing, but rather that the measure of matching decides the resulting stiffness of the mechanism. However, the only goal was to match the two buckling loads, or in terms of the critical load ratio, maximize the ratio. In order to effectively use this as a design method, i.e. obtain the desired stiffness (negative, positive or zero), a metric could be designed. This metric would relate the amount of stiffness compensation to the critical load ratio, and provide a stiffness directed design method. It was experienced that buckling modes tend to change their order upon changes in the geometry. Therefore, a good starting point would be to vary only a single parameter and provide a metric for the mechanism in question.

This thesis started from the field of energy harvesting, with an interest in the dynamics of bistable mechanisms for energy harvesting. Along the way, this interest shifted to statics and overcoming the problems encountered in bistable mechanisms. However, an interest in dynamics has never been lost, but rather fueled by the new findings in this thesis. The torsion spring linkage is a convenient and insightful model for dynamical analysis. Due to its simplicity of having only two modes, it is a good starting point for those with interest in dynamic modal analysis of pre-stressed mechanisms. It would be interesting to excite the physical model using a frequency sweep and identifying the vibration modes of the simple pre-stressed mechanism. Attempts in finite element modeling of this problem were made, but ceased. The analytical and physical models however, should provide much insight in the dynamics.

Finally, with the method for stiffness compensation established, the initial subject of this thesis remains untouched apart from a literature review. While energy harvesting has not recurred from Chapter 2 on, it has been an ongoing goal in the research group this project was a part of. With the motivation for stiffness compensation in mind, it would be interesting to conduct experiments on the dynamics of statically balanced mechanisms. The low, or even lack of, stiffness results in little resistance to vibrations and therefore an interesting energy harvesting mechanism for a broadband and low-frequency region. Other members of the research group facilitated the experimental equipment such as shaker setup with vibration control, a large stroke linear stage with vibration control, and piezo-film for quick assessment of energy harvesting performance. It is recommended to simply build a mechanism, or even use one of the designs from this project, and test it, rather than trying to simulate and predict every outcome. Experience showed that prototyping and testing, while they may seem more intricate and strenuous, are a quicker way of getting to know something than simulations.

Acknowledgements

Firstly, I want to thank my supervisors for their ongoing support, not only regarding the project but also on an emotional level during this year and especially the final few months. Thijs, your supervision with frequent meetings, endless input and new ideas, late nights of texting about ANSYS, practical tips, and also just asking if everything is going well were of huge help during this period. I think it is safe to say that we started this project as student and supervisor, but concluded it as good friends. Fred, thank you for taking me under your wing. You have been an example for me ever since I had my first lecture from you. I cannot express how grateful I was when I read your enthusiastic response to my project proposal. The many meetings I had with you have resulted in numerous new ideas, analyses and great results. Without the two of you, I could not have managed to bring this project to this level.

Secondly, thanks to Thijs, I was all but on my own during this project. The research group, informally known as "de stroomgraaiers", made this period a lot more manageable. At least one of you guys would always be in the lab to have a chat or grab some lunch with. Stefan, Johan, Joeri, Kylian, Erik, Robin, Rutger, Max, thank you all, but I have to pick out two of you in particular. Joeri, thank you for responding to my texts about some programming trick late at night (read 1:30 AM), even if you were in a bar with friends. You were there to help with the little things in measuring, defining my findings clearly and making my see my work from a new perspective many times. Stefan, you have been with me since day one. We have finished these five years together, and I could not have wished for someone better to do this with. You would always find a way to calm me down and see things differently in stressful moments, I could always count on you during courses, and you were always there as an amazing friend.

I would like to thank the excellent lab support. Gideon, Bradley and Patrick, your extensive help during the practical work is much appreciated and made it possible for me to conclude my work with good measurement results and three prototypes. Patrick, thank you for teaching me so many things and stopping by every time I was busy with my measurements to check whether it was going well, not only with the measurements but in general as well.

To my friends, thank you for putting up with me spending more time on my work than with you. I do not have any excuse anymore, so from now on there is no reason for me to decline your invitations to parties and other activities. To the friends I have made along the way in these past years, thank you for adding more to studying than just education.

Last but not least, Eveline, you deserve a special place in this chapter. Thank you for being there for me in these past two years. I will never forget the many hours I spent at your office talking about whatever, the amazing help you offered, and you trying to persuade me to continue with a PhD. I think I speak for many students when I say this master program would not be the same without you.

Appendix A
Lumped-compliant four-bar mechanism: modeling and prototyping

This chapter serves as a first iteration of the lumped-compliant four-bar mechanism experiments. The mathematical steps in the model are elaborated; finite element modeling of the linkage is discussed as well as prototyping of the physical model. As in Chapter 4, the influence of buckling mode interaction is evaluated in simulations and experiments. The experiments are conducted iteratively, i.e. the measurement method is changed according to encountered problems along the way.

A.1 Analytical linkage model

Recall the Torsion Spring Linkage (TSL) in Figure A.1. The model comprises four rigid links of length L; four joints labelled A, B, C and D; four torsion springs with stiffness k_a, k_b, k_c and k_d; a linear spring with stiffness k. The torsion springs act as the deformable elements storing the elastic potential energy during deformation. The linear spring acts as the pre-loading element: by moving the wall to which spring is attached a distance d past point D, the beam is loaded axially and buckles into the first mode.

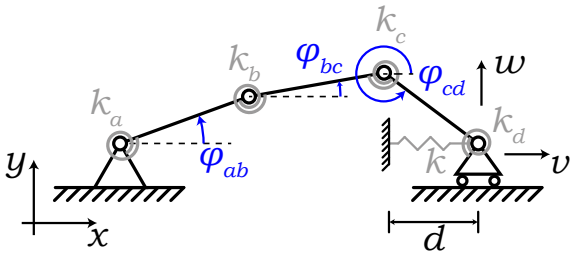

Figure A.1: Linkage model used for mode interaction hypothesis with rigid links and torsion springs. By applying a pre-loading displacement d to the rigid connection of the linear spring k, the beam is brought into a buckled state

A

A.1.1 Kinematics

In Figure A.1, three degrees of freedom (DoF) φ_{ij} are displayed; however, the Chebyshev-Grübler-Kutzbach criterion (A.1) states there are two DoFs, with the number of rigid bodies $N = 4$, number of joints $j = 4$, number of DoFs $\sum_{i=1}^{j} f_i = 5$. The DoFs are then chosen to be φ_{ab} and φ_{cd}.

$$M = 3(N-1-j) + \sum_{i=1}^{j} f_i \tag{A.1}$$

Using these two DoFs, the kinematics of the model can be described. Figure A.2 displays the kinematics of a single link, consisting of a horizontal displacement (v), vertical displacement (w) and a rotation φ. Following the chosen DoFs, the vertical and horizontal displacements are expressed in terms of φ as:

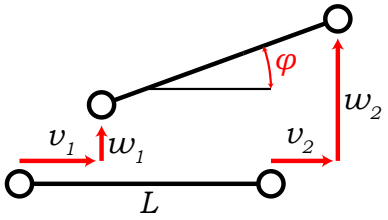

Figure A.2: Kinematics of a single link, consisting of a horizontal displacement v, vertical displacement w and a rotation φ

$$\Delta v = v_2 - v_1 = L\left(\cos\varphi - 1\right) \tag{A.2}$$
$$\Delta w = w_2 - w_1 = L\sin\varphi \tag{A.3}$$

Summing these displacements along the entire beam returns the horizontal and vertical displacements of point D

$$v = \Delta v_{AB} + \Delta v_{BC} + \Delta v_{CD} = L\left(\cos\varphi_{ab} - 1\right) + L\left(\cos\varphi_{bc} - 1\right) + L\left(\cos\varphi_{cd} - 1\right) \tag{A.4}$$
$$w = \Delta w_{AB} + \Delta w_{BC} + \Delta w_{CD} = L\sin\varphi_{ab} + L\sin\varphi_{bc} + L\sin\varphi_{cd} \tag{A.5}$$

We take a Taylor expansion of the trigonometric expressions around 0 in Expressions (A.2) and (A.3)

$$\begin{aligned}
\sin\varphi &= \sin(0) + \frac{\cos(0)}{1!}\varphi + \frac{-\sin(0)}{2!}(\varphi-0)^2 + \frac{-\cos(0)}{3!}(\varphi-0)^3 + \cdots \\
&= 0 + \varphi + 0 - \frac{1}{6}\varphi^3 + \cdots \\
\cos\varphi - 1 &= \cos(0) + \frac{-\sin(0)}{1!}\varphi + \frac{-\cos(0)}{2!}(\varphi-0)^2 + \frac{\sin(0)}{3!}(\varphi-0)^3 + \cdots - 1 \\
&= 1 + 0 - \frac{1}{2}\varphi^2 + 0 + \cdots - 1
\end{aligned}$$

By assuming moderate rotations ($\varphi^2 \ll 1$), we get

$$\sin\varphi = \varphi$$
$$\cos\varphi - 1 = -\frac{1}{2}\varphi^2$$

Therewith, Expressions (A.4) and (A.5) simplify to:

$$v = -\frac{1}{2}L\left(\varphi_{ab}^2 + \varphi_{bc}^2 + \varphi_{cd}^2\right) \tag{A.6}$$
$$w = L\left(\varphi_{ab} + \varphi_{bc} + \varphi_{cd}\right) \tag{A.7}$$

The slider joint in point D prevents a vertical displacement; therefore, by setting setting $w = 0$, the rotation of link BC (φ_{bc}) can be expressed in terms of the DoFs. Substituting Expression (A.8) into Expression (A.6) returns the horizontal displacement in point D is expressed in terms of the DoFs.

$$\varphi_{bc} = -\varphi_{ab} - \varphi_{cd} \tag{A.8}$$
$$\begin{aligned} v &= -\frac{1}{2}L\left(\varphi_{ab}^2 + \left(-\varphi_{ab} - \varphi_{cd}\right)^2 + \varphi_{cd}^2\right) \\ &= -\frac{1}{2}L\left(\varphi_{ab}^2 + \left(\varphi_{ab}^2 + 2\varphi_{ab}\varphi_{cd} + \varphi_{cd}^2\right) + \varphi_{cd}^2\right) \\ &= -\frac{1}{2}L\left(2\varphi_{ab}^2 + 2\varphi_{ab}\varphi_{cd} + 2\varphi_{cd}^2\right) \\ &= -L\left(\varphi_{ab}^2 + \varphi_{ab}\varphi_{cd} + \varphi_{cd}^2\right) \end{aligned} \tag{A.9}$$

A.1.2 Buckling problem

With the kinematics established, the buckling problem can now be tackled to gain insight into the first two buckling loads and the conditions at which the modes are able to interact. The buckling problem starts with establishing the potential energy of the beam, which consists of an elastic potential $\mathscr{E}$ and a load potential $\mathscr{B}$. The elastic potential is the work done by the torsion springs and the pre-loading spring, i.e. the elastic energy stored in the springs due to the deformation. The load potential is the work done by the displacement of the applied external loads; however, pre-loading is done using a spring and hence it follows that $\mathscr{B} = 0$. Summing the two potentials returns the total potential energy of the system Φ.

$$\Phi = \mathscr{E} + \mathscr{B} \tag{A.10}$$
$$\mathscr{E} = \frac{1}{2}k_a\varphi_{ab}^2 + \frac{1}{2}k_b\left(\varphi_{bc} - \varphi_{ab}\right)^2 + \frac{1}{2}k_c\left(\varphi_{cd} - \varphi_{bc}\right)^2 + \frac{1}{2}k_d\varphi_{cd}^2 + \frac{1}{2}k\left(d - v\right)^2 \tag{A.11}$$
$$\mathscr{B} = 0 \tag{A.12}$$

For the sake of neatness, let us take $[\varphi_{ab};\varphi_{cd}]^T = [\varphi_1;\varphi_2]^T$. Using Expressions (A.8) and (A.9), the total potential expressed in the DoFs is given as

$$\begin{aligned}\Phi =& \frac{1}{2}k_a\varphi_1^2 + \frac{1}{2}k_b\left(-\varphi_1-\varphi_2-\varphi_1\right)^2 + \frac{1}{2}k_c\left(\varphi_2-\left(-\varphi_1-\varphi_2\right)\right)^2 + \frac{1}{2}k_d\varphi_2^2 \\ &+ \frac{1}{2}k\left[d+L\left(\varphi_1^2+\varphi_1\varphi_2+\varphi_2^2\right)\right]^2 \\ =& \frac{1}{2}k_a\varphi_1^2 + \frac{1}{2}k_b\left(-2\varphi_1-\varphi_2\right)^2 + \frac{1}{2}k_c\left(\varphi_1+2\varphi_2\right)^2 + \frac{1}{2}k_d\varphi_2^2 \\ &+ \frac{1}{2}k\left[d+L\left(\varphi_1^2+\varphi_1\varphi_2+\varphi_2^2\right)\right]^2 \\ =& \frac{1}{2}k_a\varphi_1^2 + \frac{1}{2}k_b\left(2\varphi_1+\varphi_2\right)^2 + \frac{1}{2}k_c\left(\varphi_1+2\varphi_2\right)^2 + \frac{1}{2}k_d\varphi_2^2 \\ &+ \frac{1}{2}k\left[d+L\left(\varphi_1^2+\varphi_1\varphi_2+\varphi_2^2\right)\right]^2 \end{aligned} \tag{A.13}$$

Equilibrium equations

The solution of the buckling problem continues with establishing the equilibrium equations. Following the energy method described by Budiansky (Section 3.4.2), the first step is to find a stationary value of the systems' potential energy with respect to the DoFs:

$$\delta\Phi\left[\mathbf{u};d\right] = \Phi'\left[\mathbf{u};d\right]\,\delta\mathbf{u} = 0 \tag{A.14}$$

with $\delta\mathbf{u}$ denoting an arbitrary kinematically admissible perturbation of the DoFs. Translated to the discrete beam model this becomes

$$\delta\Phi = \Phi'\delta\mathbf{u} = \frac{\partial\Phi}{\partial\varphi_1}\delta\varphi_1 + \frac{\partial\Phi}{\partial\varphi_2}\delta\varphi_2 = 0 \tag{A.15}$$

For the principle of virtual work to hold, it must hold that $\delta\mathbf{u} \neq 0$ and kinematically admissible, meaning that the equilibrium equations are given as

$$\begin{aligned}\frac{\partial\Phi}{\partial\varphi_1} &= k_a\varphi_1 + k_b\left(4\varphi_1+2\varphi_2\right) + k_c\left(\varphi_1+2\varphi_2\right) \\ &+ \frac{1}{2}k\left[2dL\left\{2\varphi_1+\varphi_2\right\} + L^2\left\{4\varphi_1^3+6\varphi_1^2\varphi_2+6\varphi_1\varphi_2^2+2\varphi_2^3\right\}\right] = 0\end{aligned} \tag{A.16}$$

$$\begin{aligned}\frac{\partial\Phi}{\partial\varphi_2} &= k_b\left(2\varphi_1+\varphi_2\right) + k_c\left(2\varphi_1+4\varphi_2\right) + k_d\varphi_2 \\ &+ \frac{1}{2}k\left[2dL\left\{\varphi_1+2\varphi_2\right\} + L^2\left\{2\varphi_1^3+6\varphi_1^2\varphi_2+6\varphi_1\varphi_2^2+4\varphi_2^3\right\}\right] = 0\end{aligned} \tag{A.17}$$

By solving the equilibrium equations in (A.16) and (A.17), the pre-buckling solution $\mathbf{u}_0$ is obtained. This pre-buckling solution describes the state of the beam before buckling occurs. In this case, there is only axial deformation of the beam, i.e. $\varphi_1 = \varphi_2 = 0$, due to the axial loading $d \neq 0$.

$$\mathbf{u}_0 = \begin{cases}\varphi_{1,0} = 0 \\ \varphi_{2,0} = 0 \\ d_0 \neq 0\end{cases} \tag{A.18}$$

Stability

The pre-buckling solution follows from a stationary value of the potential energy. Since buckling has not yet occurred, the pre-buckling solution has to be a stable solution, i.e. it has to return a local minimum of potential energy. The stability of the solution is evaluated by perturbing the pre-buckling solution and searching for a solution nearby, which is described as the buckling condition:

$$\delta\Phi''\left[\mathbf{u}_0(d_c);d_c\right]\boldsymbol{\theta}\,\delta\mathbf{u}=\Phi_c''\boldsymbol{\theta}\,\delta\mathbf{u}=0 \tag{A.19}$$

with $\boldsymbol{\theta}$ denoting the buckling modes. As stated in Section 3.2, this requires us to evaluate the second derivative of the potential energy with respect to the DoFs in the buckling solution. Translating (A.19) to the beam problem gives

$$\begin{bmatrix}\delta\varphi_1 & \delta\varphi_2\end{bmatrix}\begin{bmatrix}\frac{\partial^2\Phi}{\partial\varphi_1^2} & \frac{\partial^2\Phi}{\partial\varphi_1\partial\varphi_2}\\ \frac{\partial^2\Phi}{\partial\varphi_2\partial\varphi_1} & \frac{\partial^2\Phi}{\partial\varphi_2^2}\end{bmatrix}_{\mathbf{u}_0}\begin{bmatrix}\theta_1\\ \theta_2\end{bmatrix}=\mathbf{0} \qquad \text{, with} \tag{A.20}$$

$$\begin{aligned}\frac{\partial^2\Phi}{\partial\varphi_1^2}&=k_a+4k_b+k_c+\frac{1}{2}k\left[2dL\{2\}+L^2\left\{12\varphi_1^2+12\varphi_1\varphi_2+6\varphi_2^2\right\}\right]\\ \frac{\partial^2\Phi}{\partial\varphi_1\partial\varphi_2}&=\frac{\partial^2\Phi}{\partial\varphi_2\partial\varphi_1}=2k_b+2k_c+\frac{1}{2}k\left[2dL+L^2\left\{6\varphi_1^2+12\varphi_1\varphi_2+6\varphi_2^2\right\}\right]\\ \frac{\partial^2\Phi}{\partial\varphi_2^2}&=k_b+4k_c+k_d+\frac{1}{2}k\left[2dL\{2\}+L^2\left\{6\varphi_1^2+12\varphi_1\varphi_2+12\varphi_2^2\right\}\right]\end{aligned}$$

As the principle of virtual work must hold, $\delta\mathbf{u}\neq 0$ is a requirement. A trivial solution would then be that $\theta_1=0$ and $\theta_2=0$. However, this trivial solution means that no buckling is occurring. Therefore, a non-trivial solution can only be found for $\det\left(\Phi''|_{\mathbf{u}_0}\right)=0$, which returns the eigenvalue problem as

$$\begin{bmatrix}\frac{\partial^2\Phi}{\partial\varphi_1^2} & \frac{\partial^2\Phi}{\partial\varphi_1\partial\varphi_2}\\ \frac{\partial^2\Phi}{\partial\varphi_2\partial\varphi_1} & \frac{\partial^2\Phi}{\partial\varphi_2^2}\end{bmatrix}_{\mathbf{u}_0}\begin{bmatrix}\theta_1\\ \theta_2\end{bmatrix}=\left\{\begin{bmatrix}k_a+4k_b+k_c & 2\left(k_b+k_c\right)\\ 2\left(k_b+k_c\right) & k_b+4k_c+k_d\end{bmatrix}+2dL\begin{bmatrix}2k & k\\ k & 2k\end{bmatrix}\right\}\begin{bmatrix}\theta_1\\ \theta_2\end{bmatrix}=\mathbf{0} \tag{A.21}$$

The eigenvalue problem is composed of a first term with torsional stiffness and axial stiffness, with units $k_i=[\mathrm{N\,m}]$ and $k=\left[\frac{\mathrm{N}}{\mathrm{m}}\right]$ respectively. The eigenvalues are represented by the second term, with units $dLk=\left[\mathrm{m}^2\frac{\mathrm{N}}{\mathrm{m}}\right]=[\mathrm{N\,m}]$. This eigenvalue problem can now be made dimensionless by introducing the three dimensionless groups in (A.22). The resulting non-dimensional eigenvalue problem with dimensionless eigenvalue μ is given in (A.23).

$$\alpha=\frac{k_a+3k_b}{k_b+k_c}\qquad\beta=\frac{k_d+3k_c}{k_b+k_c}\qquad\mu=\frac{kdL}{k_b+k_c} \tag{A.22}$$

$$\left\{\begin{bmatrix}\alpha+1 & 2\\ 2 & \beta+1\end{bmatrix}+\mu\begin{bmatrix}2 & 1\\ 1 & 2\end{bmatrix}\right\}\begin{bmatrix}\theta_1\\ \theta_2\end{bmatrix}=\mathbf{0} \tag{A.23}$$

A

A.1.3 Matching eigenvalues

Expression (A.23) is in the form of a generalized eigenvalue problem, which is given in Expression (A.24). As B is invertible, the generalized form is multiplied with B^{-1} to obtain matrix $C = B^{-1}A$. The resulting form can be solved as a standard eigenvalue problem. To look into the effect of mode interaction on the potential energy curve, the first two dimensionless eigenvalues (dimensionless buckling loads) are obtained from (A.24), and their ratio is inspected for a collection of α and β. The ratio, or critical load ratio (CLR), in (A.25), is determined for a 500×500-sized grid with $\alpha = \beta = \{1, \ldots, 5\}$. It is chosen to set the grid boundary to 5, as the optimal result is within the boundaries. The CLR is displayed in Figure A.3.

$$(A - \lambda B)\boldsymbol{\theta} = \mathbf{0} \rightarrow \left(C + \mu I\right)\boldsymbol{\theta} = \mathbf{0}$$

$$A = \begin{bmatrix} \alpha+1 & 2 \\ 2 & \beta+1 \end{bmatrix} \wedge B = \begin{bmatrix} 2 & 1 \\ 1 & 2 \end{bmatrix} \wedge C = B^{-1}A \tag{A.24}$$

$$\frac{\mu_1}{\mu_2} = \frac{\alpha+\beta-\sqrt{\alpha^2-\alpha\beta+\beta^2-3\left(\alpha+\beta\right)+9}}{\alpha+\beta+\sqrt{\alpha^2-\alpha\beta+\beta^2-3\left(\alpha+\beta\right)+9}} \tag{A.25}$$

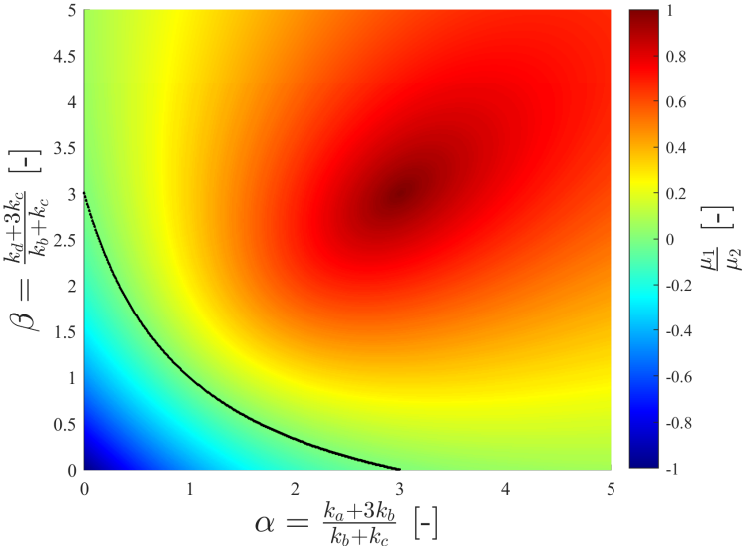

Figure A.3: Critical load ratio (CLR) surface plot to α and β. At $\alpha = \beta = 3$, the CLR is exactly equal to 1, meaning that the first two critical buckling loads are equal to one another and the buckling modes are fully interacting

From Figure A.3, it follows that for $\alpha = \beta = 3$ the CLR = 1 and thus both buckling loads are equal. For a physical interpretation, symmetry has to be assumed as follows: $k_a = k_d = c^*$ and $k_b = k_c = c$. Given that $\alpha = \beta = 3$ it follows that $k_a = k_d = 3c$; hence, for the

two first buckling loads to match, the two outermost springs need to have three times the stiffness of the inner torsion springs. In Figure A.3, the black line separates the feasible and infeasible region in the CLR. In the infeasible region, the CLR is negative. We can sample a point in the infeasible region to assess what causes this negative CLR. For instance, let us take $\alpha = 1$ and $\beta = 1$. Following the symmetry assumption $k_a = k_b = c^*$ and $k_b = k_c = c$, this gives

$$\alpha = \frac{k_a + 3k_b}{k_b + k_c} = 1 \wedge \beta = \frac{k_d + 3k_c}{k_b + k_c} = 1$$
$$\frac{c^* + 3c}{2c} = 1$$
$$c^* = -c$$

The result is a negative stiffness in the torsion springs. While this may be obtainable through certain methods, it is not seen as an available property. Therefore, the negative CLR values are defined as an infeasible region.

A.1.4 Potential energy curves

To analyze the implications on the potential energy curve of the beam, the potential energy during deflection has to be recorded. The deflection is defined by φ_1 as an array ranging from $\pi/10$ to $-\pi/10$ and back in $n = 200$ steps. For every choice of φ_1, there exists a choice of φ_2 that results in a kinematically admissible configuration of the beam; this choice of φ_2 is governed by the potential energy and is found by minimizing Φ. The process is summarized follows:

1. Initialization step: set $\varphi_{1,i=1} = \pi/10$ and determine the global minimum to find the corresponding $\varphi_{2,i=1}$.
2. Introduce a prescribed perturbation so that $\varphi_{1,i} = \varphi_{1,i-1} + \Delta\varphi_1$.
3. Establish function $\Phi|_{\varphi_{1,i}}[\varphi_2]$.
4. Evaluate gradient $\partial(\Phi|_{\varphi_{1,i}})/\partial\varphi_2$ in point $(\varphi_{1,i}, \varphi_{2,i-1})$.
   If $\partial(\Phi|_{\varphi_{1,i}})/\partial\varphi_2 \leq 0$ search for the minima of $\Phi|_{\varphi_{1,i}}$ for $\varphi_2 \geq \varphi_{2,i-1}$.
   If $\partial(\Phi|_{\varphi_{1,i}})/\partial\varphi_2 > 0$ search for the minima of $\Phi|_{\varphi_{1,i}}$ for $\varphi_2 \leq \varphi_{2,i-1}$.
5. The correct choice of $\varphi_2 = \varphi_{2,i}$ lies at the first encountered local minimum.
6. Repeat steps 2 to 5 until $i = n$

Step 3 is depicted in Figure A.4. Any system seeks to maintain a state of stable equilibrium, even when momentarily or continuously perturbed. As discussed in Chapter 3, an equilibrium is found at a stationary value of potential energy; this equilibrium is stable if the stationary value is at a (local) minimum. In Figure A.4a, the perturbation of φ_1 is depicted with two kinematically admissible configurations enclosing a blue area. In theory, φ_2 could be any value between the boundaries of this area; however, the potential energy governs the correct choice. The potential energy function $\Phi|_{\varphi_{1,i}}[\varphi_2]$ is depicted

together with the solution of the previous simulation step, $\varphi_{2,i-1}$ (Figure A.4b). Evaluating the gradient in this previous solution returns $\partial(\Phi|_{\varphi_{1,i}})/\partial\varphi_2 > 0$. As can be seen, there lie two minima of potential energy left of this previous solution. As the deformation of the mechanism is done quasi-statically, there is not sufficient energy input to carry the mechanism over the potential barrier to the second minimum; hence, the correct choice of $\varphi_{2,i}$ lies at the first encountered minimum of potential energy.

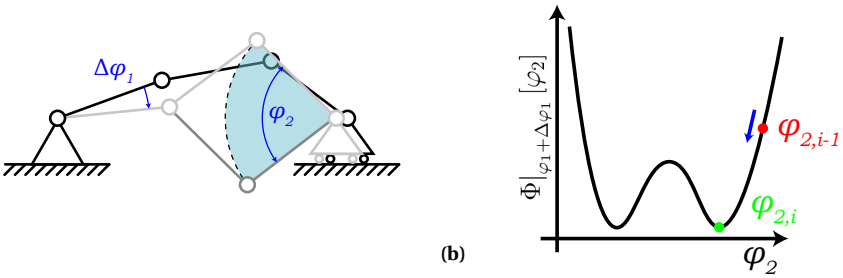

Figure A.4: Initial and perturbed configuration of beam (a) and corresponding potential energy (b) $\Phi|_{\varphi_{1,i}}[\varphi_2]$ with previous solution $\varphi_{2,i-1}$ and next solution $\varphi_{2,i}$. φ_2 could for instance be any value within the blue area; however, the correct choice is found at the first encountered minimum in opposite of direction of the gradient in the previous solution

With the complete set of DoFs established, the potential energy for the imposed deformation is evaluated and depicted in Figure A.5b. The continuous and dashed lines indicate two load paths respectively, which is a result of actuation on either of the links on the side. It can be observed that in the 3c-c-c-3c Architecture, the resulting potential energy curve is flat, indicating that this Architecture is in a state neutral equilibrium throughout the imposed range of motion; hence, statically balanced.

A.1.5 Force-deflection characteristics

The potential energy is an indication of the mechanism's behavior and shows the desired result for the 3c-c-c-3c Architecture. However, potential energy is not a physically measurable quantity; hence, to be able to compare the analytical model to experimental results, the force-deflection characteristics have to be obtained. To this end, two external loads are imposed on the beam, as displayed in Figure A.6. The external loads comprise an asymmetric load F_a and a symmetric load F_s imposed in the nodes O_a and O_s respectively. The presence of the external loads in the equilibrium equations is governed by the load potential $\mathscr{B}$. As said, $\mathscr{B}$ describes the work done due to displacement of the external loads. A method to determine correct sign of the load potential is by imagining load is applied through a combination of masses and pulleys; this is depicted in Figure A.7. By applying a perturbation of the DoF in positive direction, the direction of the mass can be observed. If the mass rises, its potential energy will increase and the load potential of the corresponding external load will be positive. Expressing the displacements of nodes O_a and O_s in terms of the DoF returns the load potential (A.26).

$$\mathscr{B} = \varphi_1\left(\frac{1}{2}F_aL + \frac{1}{2}F_sL\right) - \frac{1}{2}F_sL\varphi_2 \tag{A.26}$$

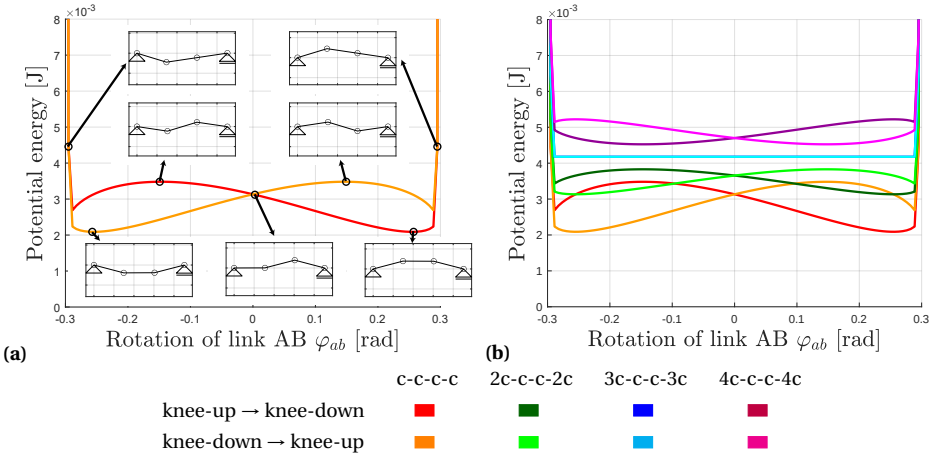

Figure A.5: Potential energy curve with linkage configurations indicated (a). Potential energy curves of c-c-c-c to 4c-c-c-4c Architectures (b) for deflection from knee-up to knee-down and back; it is observed that the potential energy is flat for a finite range of motion in the 3c-c-c-3c Architecture, indicating statically balanced behavior

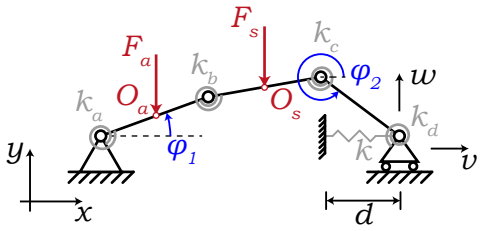

Figure A.6: TSL linkage with external asymmetric load F_a and symmetric load F_s applied in nodes O_a and O_s respectively

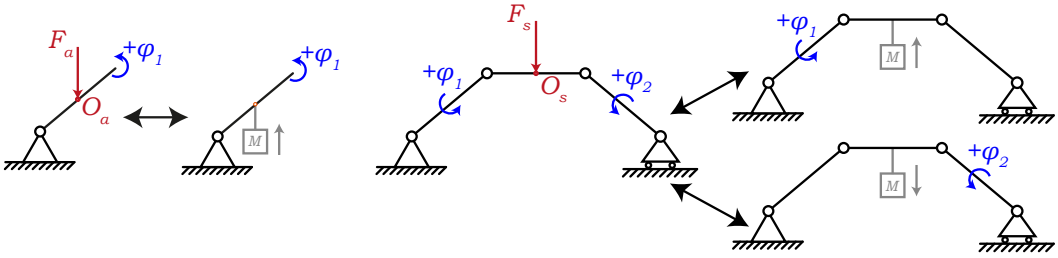

Figure A.7: Determining the sign of the load potential by imposing the external loads with masses. By applying a perturbation of the DOF in positive direction, it can be observed in which direction the mass will move, and hence whether its potential energy will in or decrease

Substituting (A.26) in (A.16) and (A.17), returns the new equilibrium equations which can be made dimensionless using α, β and μ.

$$\frac{\partial\bar{\Phi}}{\partial\varphi_1} = \varphi_1(1+\alpha) + 2\varphi_2 + \mu(2\varphi_1+\varphi_2) + \frac{kL^2}{k_b+k_c}\{\varphi_1^2+\varphi_1\varphi_2+\varphi_2^2\}(2\varphi_1+\varphi_2) + \frac{1}{2}\frac{F_aL}{k_b+k_c} + \frac{1}{2}\frac{F_sL}{k_b+k_c} = 0 \tag{A.27}$$

$$\frac{\partial\bar{\Phi}}{\partial\varphi_2} = 2\varphi_1 + \varphi_2(1+\beta) + \mu(\varphi_1+2\varphi_2) + \frac{kL^2}{k_b+k_c}\{\varphi_1^2+\varphi_1\varphi_2+\varphi_2^2\}(\varphi_1+2\varphi_2) - \frac{1}{2}\frac{F_sL}{k_b+k_c} = 0 \tag{A.28}$$

This is taken a step further with the introduction of:

$$\omega = \frac{kL^2}{k_b+k_c} \qquad \mu = \frac{dkL}{k_b+k_c} = \frac{d}{L}\omega = \lambda\omega \qquad f = \frac{F}{kL} \tag{A.29}$$

This finally gives the dimensionless equilibrium equations (A.30) and (A.31) from which the external loads can be solved by displacement of O_a and O_s. The force-deflection characteristics of the symmetric load is displayed in Figure A.8, since this is the measurement location used in the experiments. It can be observed that the actuation force diminishes to zero for the 3c-c-c-3c Architecture, as was observed with the flat potential energy curve in Figure A.5b. Another interesting observation is the positive stiffness occurring in the 4c-c-c-4c Architecture, which arises due to the switching of the buckling modes: the prior second mode (S) now becomes the first buckling mode due to the adjusted stiffness.

$$\frac{\partial\bar{\Phi}}{\partial\varphi_1} = \varphi_1(1+\alpha) + 2\varphi_2 + \omega\left[\lambda + \{\varphi_1^2+\varphi_1\varphi_2+\varphi_2^2\}\right](2\varphi_1+\varphi_2) + \frac{1}{2}f_a\omega + \frac{1}{2}f_s\omega = 0 \tag{A.30}$$

$$\frac{\partial\bar{\Phi}}{\partial\varphi_2} = 2\varphi_1 + \varphi_2(1+\beta) + \omega\left[\lambda + \{\varphi_1^2+\varphi_1\varphi_2+\varphi_2^2\}\right](\varphi_1+2\varphi_2) - \frac{1}{2}f_s\omega = 0 \tag{A.31}$$

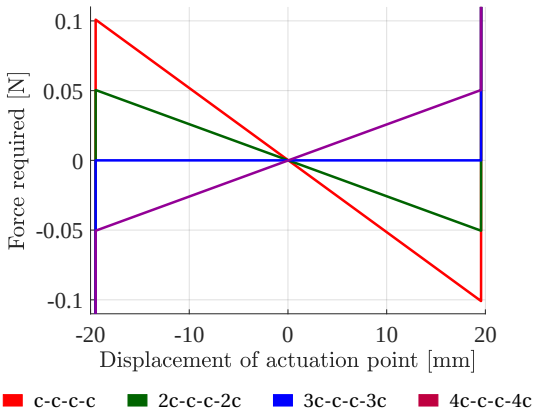

Figure A.8: Analytical force-deflection characteristics of symmetric load F_s for the four beam Architectures

A

A.2 Physical model

The TSL indicates that buckling mode interaction is indeed a method for static balancing. However, the question whether the desired results also occurs in reality still remains. In this section, the TSL is translated to a physical model and a force-deflection measurement is performed to analyze the behavior of the four linkage architectures.

A.2.1 Reverse PRB modelling

The TSL in Figure A.1 is used to describe a lumped-compliant four-bar mechanism. In Pseudo-Rigid Body modeling, torsion springs are used to represent flexural elements. In the TSL, the concentrated torsion springs are small in length compared to the rigid links. In this case, the torsion springs represent small-length flexural pivots, as presented in Figure A.9, for which holds that $l \ll L$ and $(EI)_l \ll (EI)_L$. For a rigid body with a small-length flexural pivot subjected to an end moment M, the stiffness of the flexural pivot is given by Expression (A.32) [76].

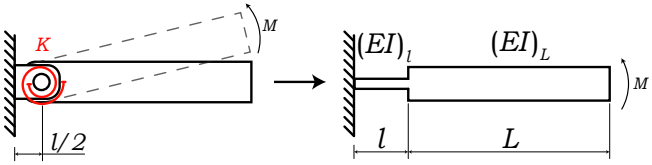

Figure A.9: Pseudo-Ridig Body representation of torsion springs: translated to a compliant model, the torsion springs in the torsion spring linkage can be interpreted as small-length flexural pivots of with stiffness K [76]

$$K = \frac{(EI)_l}{l} \tag{A.32}$$

A.2.2 Manufacturing

Using the small-length flexural pivots, the TSL is converted into a physical model. Four architectures are manufactured: c-c-c-c, 2c-c-c-2c, 3c-c-c-3c and 4c-c-c-4c. It is chosen to add the two other architectures besides the uniform and matching buckling loads ones, in order analyze the effect of stiffening the outermost torsion springs. The rigid links are laser cut from 5 mm thick PMMA to a length of $L = 70$ mm and width $w = 5$ mm. The links are provided with a 5 mm deep slit for the flexures to be embedded in. The flexures are manufactured from AISI 301 steel with a width $w_f = 5$mm and varying length and thickness using a guillotine shear. The flexures and PMMA links are assembled using a two-part epoxy adhesive. For $l \ll L$ to hold, the free length of the flexures is chosen to be $l = 7$ mm, creating a lumped compliant model. The thickness of the flexures in other architectures is reduced to roughly preserve the ratio of link to flexure length; the flexure dimensions are tabulated in Table A.1. The mechanisms are fastened to base plates using a nut and bolt connection with a clearance, introduced by spacers, of 5mm from the base plate to allow free motion. These base plates are provided with two slots on one side, allowing for a continuously variable pre-load displacement from $0-7$ mm. Drawings of a link and base plate for the c-c-c-c Architecture are displayed in Figure A.10. The resulting lumped-compliant four-bar mechanism in flat and buckled state is presented in Figure A.11.

A

Table A.1: Length and thickness of varying flexures in lumped-compliant four-bar mechanism model. All flexures have a width of $w_f = 5\,\text{mm}$

Flexure stiffness	Free length l [mm]	Thickness t_f [mm]
c	7.00	0.20
2c	11.81	0.15
3c	7.88	0.15
4c	5.91	0.15

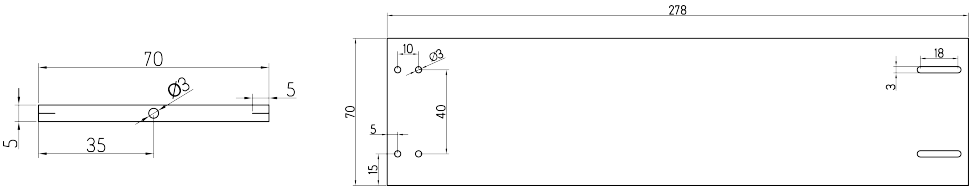

Figure A.10: Drawings of the links and base place for c-c-c-c Architecture with dimensions

(a)

(b)

Figure A.11: Lumped-compliant four bar mechanism in (a) flat and (b) buckled state after pre-loading with 7 mm pre-load distance

A.2.3 Force-deflection measurements

The force-deflection behavior of the PMMA models is evaluated using two different setups. This was done to investigate the problems encountered during the measurements. Both methods are discussed and the results are presented. Both methods use the same components, which are displayed in Figure 4.5a in Chapter 4. The PI-M 505 motion stage provides a linear motion, which is imposed onto the mechanisms. The force for the imposed displacement is recorded using a FUTEK LRM200 force sensor. This sensor allows for a maximum load of 250 g or 2.5 N. The displacement data is obtained from an internal encoder; all the data is recorded using an NI USB-6008 data acquisition unit. The mechanisms are set in their stable equilibrium position, deflected to their second stable position and back. This allows us to record any differences in load paths back and forth, and identify possibly present hysteresis.

Setup with magnet

In this method, a magnet is used to ensure a connection between the sensor and the mechanisms in the unstable region. A magnet is attached to the side of the middle PMMA link. The sensor is provided with a bearing ball attached to an M3 threaded stud. This bearing ball is placed onto to magnet, creating a point contact, as displayed in Figure A.12. The mechanism is now set into its stable position at A, and pulled back to capture the force away from the stable equilibrium position. Subsequently, the mechanism is pushed in direction of stable equilibrium B, beyond this equilibrium, and back to the starting position.

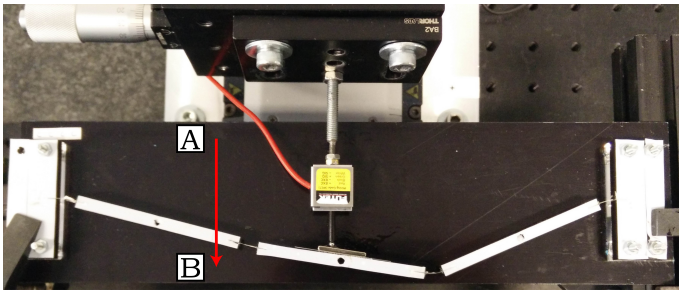

Figure A.12: Close-up of magnet connection between force sensor and mechanism. The initial position is beyond the stable equilibrium at A. The mechanism is pushed in direction of equilibrium B, beyond it and back to the initial position

The measured force-deflection characteristics for the four architectures are displayed in Figure A.13, together with the force-deflection characteristics obtained from the analytical analysis. From the analytical results, it can be seen that from an increase of the outermost spring stiffness, a counter-clockwise rotation of the force-deflection curves follows. Unfortunately, the measurement points do not match the analytical results well. Behavior reminiscent of snap-through is observed, as the force-deflection curve bulges out, then narrows down and shows a peak at the end. This may be ascribed to the fact that past the middle (0 mm displacement), the mechanism starts pulling on the sensor, which causes the measured force to decrease (increase negatively). The observed rotation from the analytical results can be slightly found in the measurements results as well. However, it is not as evident as in the analytical results. The main contributing factor to this is the presence of hysteresis, which is seen as the different load paths taken during back and forth displacement. This hysteresis may be ascribed to:

- **Manufacturing errors**: the flexures are manufactured using guillotine shears. This may result in flexures of non-uniform width, different lengths, burrs introduced by folding instead of cutting. The stiffness changes significantly due to these production errors. Non-uniform width of the flexures may result in the mechanism not being perfectly in plane. Additionally, assembly is conducted using epoxy, which results in layers of glue having their own stiffness.

- **Movement of the actuation point**: the middle point of the mechanism does not undergo a straight-line motion. As the stage, and therefore the bearing ball, is

constrained in all directions except in direction A → B, the rolling contact moves along the magnet. This definitely results in measuring a different load path.

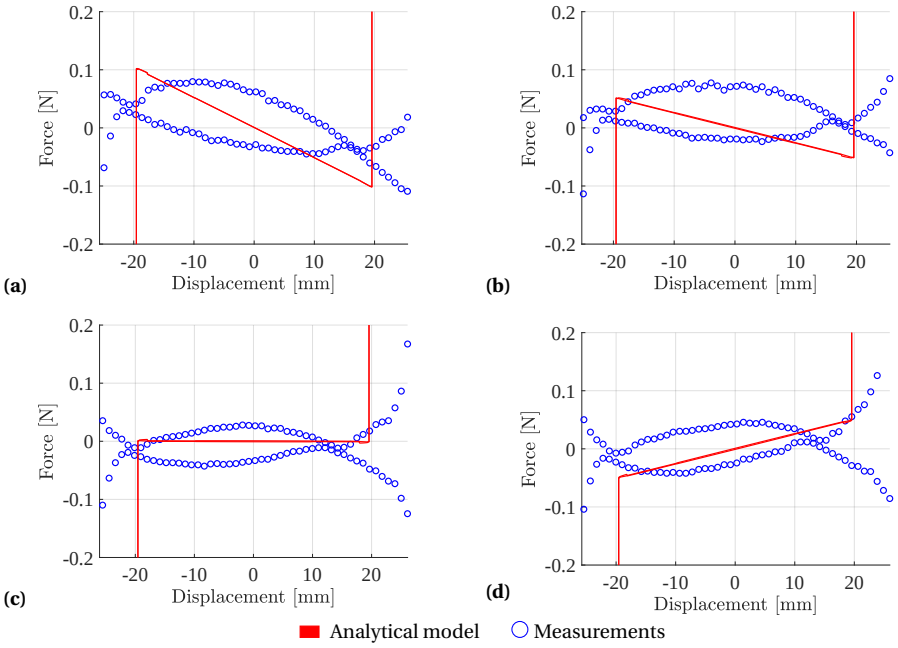

Figure A.13: Obtained force-deflection behavior from analytical analysis and measurements (magnet setup) for the four architectures: (a) c-c-c-c, (b) 2c-c-c-2c, (c) 3c-c-c-3c, (d) 4c-c-c-4c

Setup with pulley

To prevent movement of the rolling contact, the measurements are repeated with the setup in Figure A.14a. The mechanism is connected to the force sensor using fishing line; this allows the stage to pull the mechanism into the stable equilibrium at A. A 100 g mass is used to pull the mechanism back into the equilibrium at B. The pulley functions as a guidance for the fishing line, and to reduce friction in the process. As with the magnet connection, the force is measured in direction A → B and back. The results of the analytical model and measurements are displayed in Figure A.15. With the use of the mass and pulley, the "snap-through" behavior from Figure A.13a is not observed, as the mass pulls on the sensor throughout the measurement. The slope of the measured force matches that found in the analytical model better than the magnet setup measurements; hence, the counter-clockwise rotation is observed in the measurements as well. As with the magnet setup, a significant amount of hysteresis is observed. Differences between the analytical results and measurements may be ascribed to:

- **Manufacturing errors**
- **Movement of the actuation point**: the middle point of the mechanism does not undergo a straight-line motion. As a result, forces in transversal direction are exerted on the sensor; the fishing line will not pull on the sensor in a straight line throughout the measurement. This may result in a different load path.
- **Friction of the pulley**: the pulley itself introduces friction, as can be seen in Figure A.14b. This measurement presents the behavior of the mass and pulley, without the mechanism placed in between. As can be seen, two load paths are present in this reference measurement, which is ascribed to the friction in the pulley. This friction may also have caused stick slip behavior, resulting in measured values that are higher than expected.

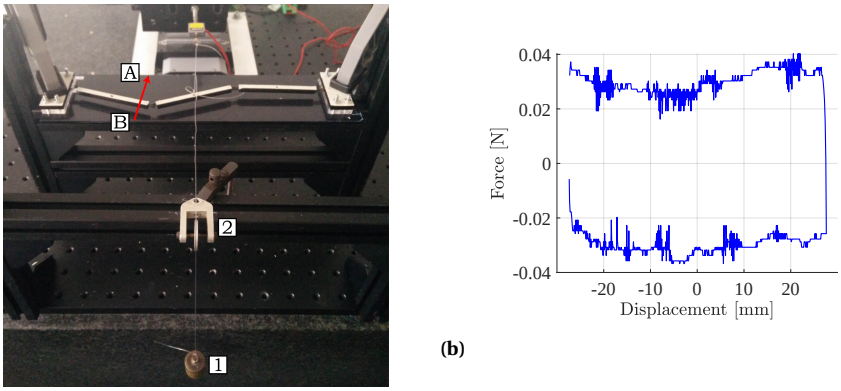

(a) **(b)**

Figure A.14: Overview of setup with mass and pulley (a). A mass (1) over a pulley (2) is connected to the mechanism and force sensor using fishing line. The mass pulls the mechanism into the stable equilibrium in B, after which the mechanism is pulled to the stable equilibrium in A. Reference measurement of pulley with mass, and mass offset deducted (b). The two different load paths indicate there is significant friction contribution by the pulley. Additionally, the sensor noise is also evident

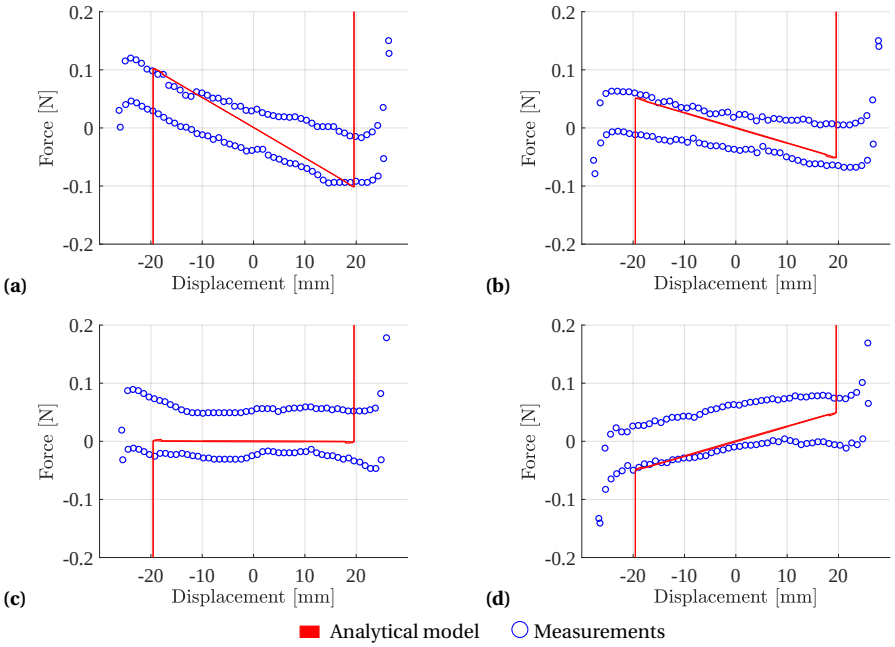

Figure A.15: Obtained force-deflection behavior from analytical analysis and measurements (pulley setup) for the four architectures: (a) c-c-c-c, (b) 2c-c-c-2c, (c) 3c-c-c-3c, (d) 4c-c-c-4c

Appendix B
Lumped-compliant four-bar mechanism: analysis steps

This chapter serves as an overview of the steps taken in the analysis of the torsion spring linkage model for the lumped-compliant four-bar mechanism. A number of analyses has been performed to investigate the effect of the matching buckling loads analytically and explain the mechanism behind the behavior. An answer has been sought in the buckling modes of the system. To this end, the buckling modes are used to express the displacement field and equilibrium equations. Introduction of these modes is discussed here as well.

B.1 General steps

B.1.1 Accuracy of model

The torsion spring linkage (TSL) is strongly simplified with the assumption of moderate rotations ($\varphi^2 \ll 1$). The error occurring due to the assumption is determined using (B.1) for $\sin(\varphi)$ and $\cos(\varphi)$. The measured angles in the physical model return an error within the 2% bound. Of course, not only the moderate rotation assumption influences the accuracy of the analytical model. In the TSL, the torsion springs are assumed as infinitely small torsion springs concentrated at the joints of the linkage. In practice however, the torsion springs are realized using flexures of finite length, with a flexural rigidity (i.e. the analytical torsion stiffness) distributed along this length. During deformation, the pivot of these flexures will shift; as a result, the rigid link length L is not constant.

$$\frac{\sin(\varphi)-\varphi}{\sin(\varphi)} \wedge \frac{\cos(\varphi)-(-\frac{1}{2}\varphi^2+1)}{\cos(\varphi)} \tag{B.1}$$

Sensitivity analysis

Figure B.1 displays the FD characteristics of the 3c-c-c-3c Architecture for slight changes in the flexure widths. The flexure widths are changed with ± 1% and ± 2% to assess the influence of imperfections in the stiffness ratios on the mechanical behavior. It is observed that a 1% error in flexure width already results in a strong increase in the stiffness. Manufacturing and assembly govern the discrepancies between the model (analytical and finite element analysis) and experimental results greatly. Improving on manufacturing may of course improve the match between these results; however, assembly has has a relatively larger influence. Clamping of the flexures is a crucial part of the assembly process. During clamping, the flexures may get caught between the thread of the

used screws or they may not be assembled exactly in plane, resulting in skewed flexures with a shorter or longer free length. As is observed from the sensitivity analysis, a slight change in the stiffness ratios influences the stiffness of the matching buckling loads configuration greatly. Hence, it cannot be expected that the experimental results of the manufactured and assembled mechanism match the analytical results perfectly.

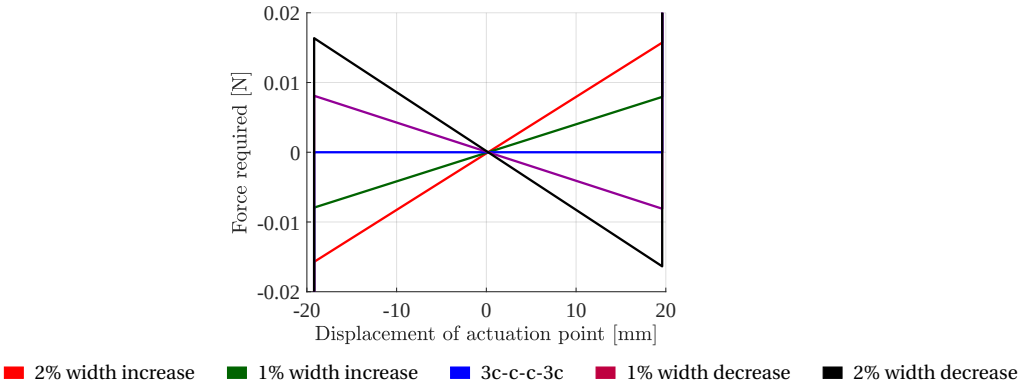

Figure B.1: Sensitivity analysis of 3c-c-c-3c Architecture. The width of the flexures is adjusted with ±1% and ±2% and the FD characteristic is evaluated

B.1.2 Potential energy surfaces

Inspired by the work in [79], the potential energy of each linkage architecture is evaluated for both DoFs. This returns the potential energy as a surface with respect to the DoF φ_1 and φ_2 on the xy-plane. Subsequently, it was chosen to map the potential energy of the beam during deflection onto this surface using the displacement field. Figure B.2 depicts the potential energy surfaces for the c-c-c-c and 3c-c-c-3c Architectures in symmetric and asymmetric actuation. There is no significant difference in paths between the beam architectures, nor a significant change in the 3c-c-c-3c Architecture potential energy surface with respect to the other Architectures. Therefore, it was concluded that this analysis did not add information to form a sound explanation of the observed FD behavior. However, it is an interesting representation of the motion of a bistable linkage in the space of its DoFs.

B.1.3 Axial reaction forces

In [79] it is mentioned that the FD characteristic of a bistable buckled beam in transverse deflection can be dissected into branches belonging to different buckling modes. Together, these branches form the FD characteristic of the beam as we have seen in this work. These branches are only obtainable if the axial load in the beam is equal to or greater than the buckling load of the corresponding mode. Based on this information, the axial reaction force for the Architectures in both actuation cases are displayed in Figure B.3. The axial reaction force curve shapes match those found in [79, 80]; however, there is no significant difference in the axial load for the 3c-c-c-3c Architecture with respect to the other Architectures. In symmetric actuation, the axial reaction in all beams is

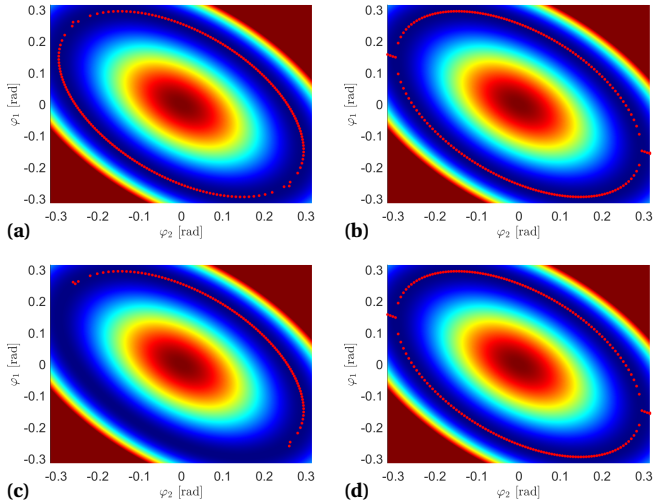

Figure B.2: Potential energy surfaces to DoF with the deflection path mapped onto the surface for the beam Architectures: c-c-c-c symmetric (a) and asymmetric (b), 3c-c-c-3c symmetric (c) and asymmetric (d)

equal to the second buckling mode, as found in literature. In the asymmetric actuation, the buckling load is reached in the middle of the deflection (0 mm).

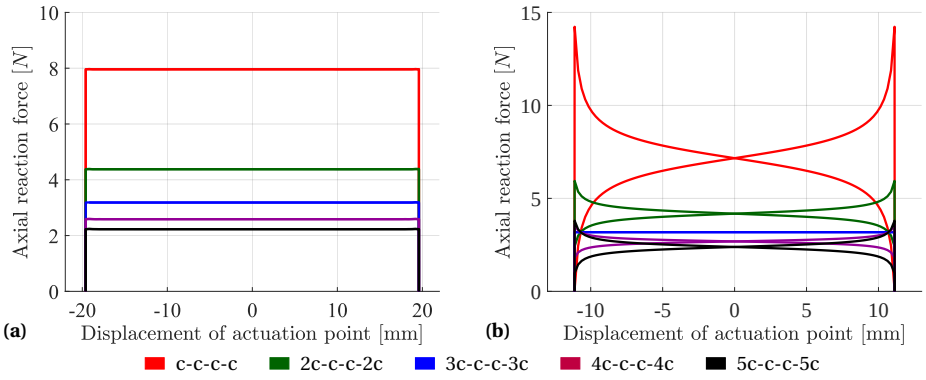

Figure B.3: Axial reaction forces for (a) symmetric and (b) asymmetric actuation

B

B.2 Modal analysis

As the hypothesis tells us to use the buckling modes by matching their loads, we refer to using the buckling modes in order to explain the effect of these buckling modes interacting. This is similar to modal analysis in dynamics, in which the vibration modes of a system are used to describe the system response to imposed vibrations. To this end, we firstly need to establish a definition of these buckling modes. Since the TSL is a discrete system, the buckling modes can easily be expressed in terms of the displacements of B and C defined by the DoFs, as in Figure B.4. In the B-mode, the points B and C are displaced an equal amount in the same direction. Following the definition of the DoFs in Chapter A, this mode is described as $\varphi_1 = -\varphi_2$. In the S-mode, they are displaced an equal amount in opposite direction, which is defined as $\varphi_1 = \varphi_2$. The two modes are stored in the mode matrix Q (B.2).

$$Q = \begin{bmatrix} 1 & 1 \\ -1 & 1 \end{bmatrix} \tag{B.2}$$

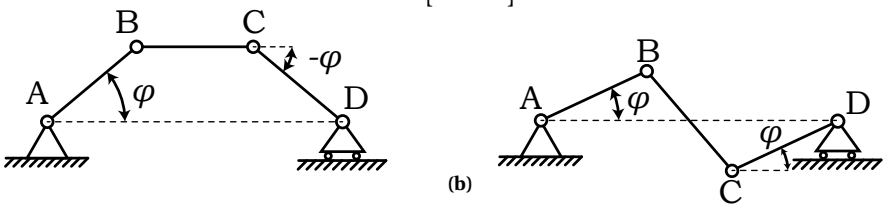

Figure B.4: Depiction of the two buckling modes B (a) and S (b) expressed in the degrees of freedom

B.2.1 Displacement field in terms of modes

The displacement field obtained can be expressed in terms of the buckling modes. As a result, the set of DoFs is now given in terms of two mode amplitudes. Separately, these mode amplitudes are difficult to interpret as actual DoFs. For instance, in the S-shape buckling mode, the location of center point (middle of link BC) is predefined to lie on the horizontal axis. By scaling the mode, we are essentially displacing nodes B and C, without affecting the vertical displacement of the center point. This is observed in the absence of contribution of symmetric load F_s when using the second mode amplitude as the actuation parameter. The displacement field is expressed in terms of the modes as:

$$\mathbf{u} = \begin{bmatrix} \varphi_1 \\ \varphi_2 \end{bmatrix} = Q\mathbf{m} = \begin{bmatrix} 1 & 1 \\ -1 & 1 \end{bmatrix} \begin{bmatrix} m_\mathrm{B} \\ m_\mathrm{S} \end{bmatrix} \tag{B.3}$$

This allows us to investigate the behavior of different linkage architectures in a space described by the buckling modes, and see whether there is a significant difference between them. To this end, the amplitude of each mode is determined using Q^{-1} and the participation factor χ_i of mode i is calculated as the ratio of the mode amplitude m_i to the sum of both amplitudes in every instance, as in (B.4). This participation factor tells us "how much" of the buckling mode is present in the current configuration ranging from 0 to 1.

$$\chi_i = \frac{|m_i|}{|m_\mathrm{B} + m_\mathrm{S}|} \tag{B.4}$$

In FEA however, this is not as straightforward as taking the inverse of the mode matrix and multiplying with the displacement field. The deflection is incrementally changed, giving a new displacement field for every sub-step S. The model consists of N nodes; hence, for every sub-step, an array of $N \times 1$ is returned for every DoF (three translations, three rotations). As we are interested in the y-displacement, the displacement field is an $N \times S$ array, where $N \neq S$. The buckling mode matrix describes the y-translation of the N nodes for M modes, giving an $N \times M$ matrix where $N \neq M$. As the mode matrix is non-square, we are not able to take the inverse of the matrix. In other words, there does not exist a unique solution to the modal amplitudes. A possible solution is by solving the least-squares problem in (B.5) following the work of [58]. The modal participation factors are determined using (B.4).

$$\mathbf{u}_{N\times 1}^{(S)} \overset{\text{least squares}}{=} Q_{N\times M}\mathbf{m}_{2\times 1}^{(S)} \tag{B.5}$$

Figure B.5 depicts the modal participation factors for the five Architectures under symmetric loading for the analytical analysis and FEA. Differences can be observed between the analytical analysis and FEA; however, these cannot be used to draw any conclusions on the differences in the FD characteristics. Unfortunately, no significant changes are identified for the analytical 3c-c-c-3c Architecture with respect to the other Architectures: the participation factors obtained do not change significantly due to the two buckling loads matching. Therefore, it was concluded that the modal participation alone did not add information to form a sound explanation of the observed FD behavior.

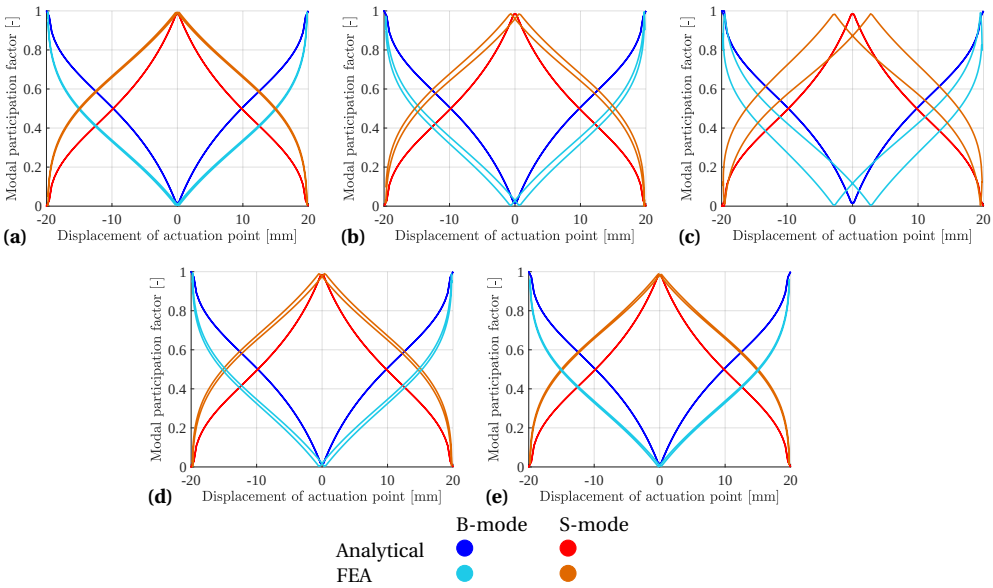

Figure B.5: Comparison of modal participation factors under symmetric actuation in FEA for the five beam Architectures: (a) c-c-c-c, (b) 2c-c-c-2c, (c) 3c-c-c-3c, (d) 4c-c-c-4c, (e) 5c-c-c-5c

B.2.2 Decomposition of strain energy in buckling modes

Despite the modal participation factors not adding any information to the explanation of the observed behavior, they strengthen the hypothesis posed in Chapter 3. Figure B.6 depicts de potential energy curve to the displacement of the actuation point for the c-c-c-c Architecture in symmetric actuation. When comparing the potential curve to the Figure B.5a, it is observed that the B-mode occurs in the stable equilibria on either end of the potential curve, while the S-mode occurs at the top of the potential barrier.

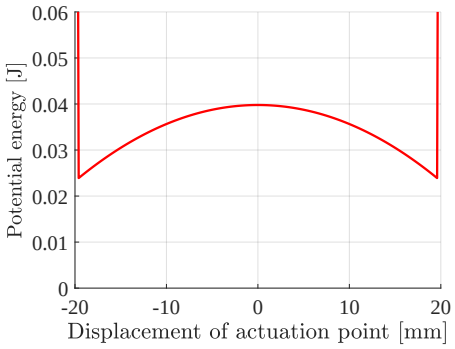

Figure B.6: Potential curve of c-c-c-c Architecture for symmetric actuation to the displacement of point O_s. Upon comparison with the modal participation factors, it is seen that the modes at the equilibria are the B and S-modes

Following [74], the potential energy, or strain energy in this case, needs to stem from some input. The input to the system to obtain these buckling modes is the pre-loading of the linkage. To obtain the B-mode during pre-loading, the axial load in the linkage needs to be equal to the critical buckling load P_B. This axial load is displaced by the pre-loading displacement d, and thus the energy input is equal to the work done by pre-loading $W_\mathrm{B} = P_\mathrm{B} d$. Hence, for the strain energy in the first buckling mode it holds that $E_\mathrm{B} = W_\mathrm{B}$. In the c-c-c-c Architecture, the B-mode is the first buckling mode. The second buckling mode (S-mode) is practically not obtainable; however, analogously, for the strain energy in the second buckling mode it holds that $E_\mathrm{S} = W_\mathrm{S}$. This can be checked by taking the buckling loads $P_\mathrm{B} = 4.77\,\mathrm{N}$ and $P_\mathrm{S} = 7.96\,\mathrm{N}$ and pre-loading displacement $d = 5\,\mathrm{mm}$, giving $E_\mathrm{B} = W_\mathrm{B} = 0.024\,\mathrm{J}$ and $E_\mathrm{S} = W_\mathrm{S} = 0.040\,\mathrm{J}$. In terms of the DoFs, the strain energy of the buckled linkage is found in (B.6). Note that this only holds for a mode participation $\chi_i = 1$ for mode i.

$$E\left[\varphi_1;\varphi_2\right] = \frac{1}{2}k_a\varphi_1^2 + \frac{1}{2}k_b\left(2\varphi_1+\varphi_2\right)^2 + \frac{1}{2}k_c\left(\varphi_1+2\varphi_2\right)^2 + \frac{1}{2}k_d\varphi_2^2 \tag{B.6}$$

As can be observed, the axial stiffness term of the beam is disregarded. This term governs the buckling conditions; however, as we are interested in the energy of the buckling mode itself, this term would give a huge increase in strain energy due to the extension of spring k. Using (B.3), the strain energy may be decomposed in terms of the buckling modes. This is not to be confused with actuation using the buckling modes. What we are essentially doing here is determining the part of the potential energy ascribed to either

buckling mode, i.e. determining $E[m_B; m_S = 0]$ and $E[m_B = 0; m_S]$ for (B.7). This analysis is performed for the symmetric actuation of the five linkage architectures and presented in Figure B.7.

$$E[m_B; m_S] = \frac{1}{2} m_B^2 (k_a + k_b + k_c + k_d) + \frac{1}{2} m_S^2 (k_a + 9k_b + 9k_c + k_d) + m_B m_S (k_a + 3k_b - 3k_c - 3k_d) \tag{B.7}$$

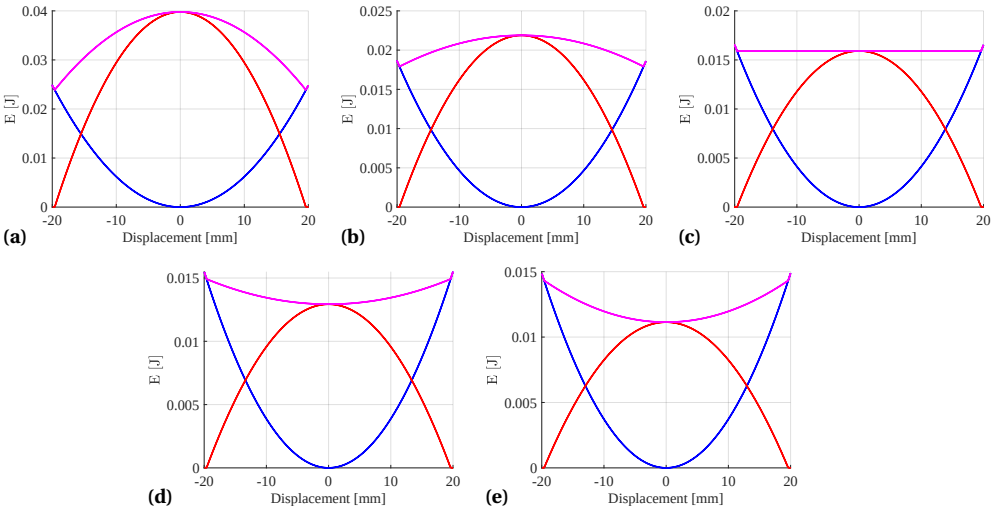

Figure B.7: Decomposition of strain energy E in buckling modes B ( ) and S ( ) contributions and their sum ( ) for symmetric actuation in linkage architectures: (a) c-c-c-c, (b) 2c-c-c-2c, (c) 3c-c-c-3c, (d) 4c-c-c-4c, (e) 5c-c-c-5c

Apart from the two separate mode contributions to the strain energy, their sum $E[m_B; m_S = 0] + E[m_B = 0; m_S]$ is also depicted. This sum is exactly equal to the total strain energy of the linkage during symmetric actuation. An interesting transition from a downward to an upward opening parabola is observed for the total strain energy from the c-c-c-c to the 5c-c-c-5c Architecture. This depicts the change in mode order as described in Chapter 4. Another interpretation is the shift of the equilibrium: whereas the stable equilibria in the c-c-c-c and 2c-c-c-2c Architectures are at either end of the motion range and fully described by the B-mode, the 4c-c-c-4c and 5c-c-c-5c Architectures have a single stable equilibrium at 0mm displacement, fully described by the S-mode. As a result, the linkage shifts from bistable behavior to monostable behavior as a result of changing the spring stiffness ratios.

Returning to the work done per buckling load, in the 3c-c-c-3c Architecture, the buckling loads are exactly equal. Hence, the strain energy in the B-mode and S-mode is equal and essentially no extra energy is required to transition from one mode to the other. As a result, the 3c-c-c-3c Architecture is statically balanced, and the FD characteristic becomes near zero as seen in Chapter 4.

B

B.2.3 Decomposition of force-deflection in buckling modes

The use of the buckling modes allows us to dissect the FD behavior in contributions per mode. This analysis is also seen in [79], in which branches of the FD characteristic are ascribed to different buckling modes. To this end, the equilibrium equations have to be projected onto the two buckling modes. Recall (4.2), which returns the equilibrium equations of the system. A constraint to this equation is that $\delta\mathbf{u}$ has to be kinematically admissible; hence, we have only looked at Φ'. For the transformation onto the modal basis however, we have to incorporate $\delta\mathbf{u}$ as well. The stationary potential energy (4.2) returns:

$$\delta\Phi\left[\mathbf{u}\right] = \Phi'\delta\mathbf{u} = \frac{\partial\Phi}{\partial\varphi_1}\delta\varphi_1 + \frac{\partial\Phi}{\partial\varphi_2}\delta\varphi_2 = 0$$

Which can also be written as:

$$\begin{bmatrix}\delta\varphi_1 & \delta\varphi_2\end{bmatrix}\begin{bmatrix}\frac{\partial\Phi}{\partial\varphi_1}\\ \frac{\partial\Phi}{\partial\varphi_2}\end{bmatrix} = 0$$

Using (B.3), we can write $\delta\mathbf{u} = Q\delta\mathbf{m}$, and hence $\delta\mathbf{u}^T = \delta\mathbf{m}^T Q^T$. Finally, the equilibrium equations on the modal basis are given by:

$$\delta\mathbf{m}^T Q^T\begin{bmatrix}\frac{\partial\Phi}{\partial\varphi_1}\\ \frac{\partial\Phi}{\partial\varphi_2}\end{bmatrix} = 0 \tag{B.8}$$

Modal basis equilibrium equations

Recall the dimensionless equilibrium equations in (B.9). Using (B.8), these equilibrium equations can be transformed to the modal basis, essentially leaving us with the modal amplitudes as DoFs. All the steps in the transformation are given below.

$$\begin{cases}\dfrac{\partial\bar{\Phi}}{\partial\varphi_1} = \varphi_1(1+\alpha) + 2\varphi_2 + \omega\left[\lambda + \left\{\varphi_1^2 + \varphi_1\varphi_2 + \varphi_2^2\right\}\right](2\varphi_1 + \varphi_2) + \dfrac{1}{2}f_a\omega + \dfrac{1}{2}f_s\omega = 0\\ \dfrac{\partial\bar{\Phi}}{\partial\varphi_2} = 2\varphi_1 + \varphi_2(1+\beta) + \omega\left[\lambda + \left\{\varphi_1^2 + \varphi_1\varphi_2 + \varphi_2^2\right\}\right](\varphi_1 + 2\varphi_2) - \dfrac{1}{2}f_s\omega = 0\end{cases} \tag{B.9}$$

First we rewrite the equilibrium equations in a matrix form:

$$\begin{bmatrix}\frac{\partial\Phi}{\partial\varphi_1}\\ \frac{\partial\Phi}{\partial\varphi_2}\end{bmatrix} = \begin{bmatrix}1+\alpha & 2\\ 2 & 1+\beta\end{bmatrix}\begin{bmatrix}\varphi_1\\ \varphi_2\end{bmatrix} + \omega\left[\lambda + \left\{\varphi_1^2 + \varphi_1\varphi_2 + \varphi_2^2\right\}\right]\begin{bmatrix}2 & 1\\ 1 & 2\end{bmatrix}\begin{bmatrix}\varphi_1\\ \varphi_2\end{bmatrix} = \begin{bmatrix}-\frac{1}{2}f_a\omega - \frac{1}{2}f_s\omega\\ \frac{1}{2}f_s\omega\end{bmatrix}$$

Next we use (B.8) to obtain the transformed matrices

$$Q^T\begin{bmatrix}1+\alpha & 2\\ 2 & 1+\beta\end{bmatrix}Q = \begin{bmatrix}1 & -1\\ 1 & 1\end{bmatrix}\begin{bmatrix}1+\alpha & 2\\ 2 & 1+\beta\end{bmatrix}\begin{bmatrix}1 & 1\\ -1 & 1\end{bmatrix} = \begin{bmatrix}-2+\alpha+\beta & \alpha-\beta\\ \alpha-\beta & 6+\alpha+\beta\end{bmatrix}$$

$$\left\{\varphi_1^2 + \varphi_1\varphi_2 + \varphi_2^2\right\} = \begin{bmatrix}\varphi_1 & \varphi_2\end{bmatrix}\begin{bmatrix}1 & \frac{1}{2}\\ \frac{1}{2} & 1\end{bmatrix}\begin{bmatrix}\varphi_1\\ \varphi_2\end{bmatrix} \rightarrow Q^T\begin{bmatrix}1 & \frac{1}{2}\\ \frac{1}{2} & 1\end{bmatrix}Q = \begin{bmatrix}1 & -1\\ 1 & 1\end{bmatrix}\begin{bmatrix}1 & \frac{1}{2}\\ \frac{1}{2} & 1\end{bmatrix}\begin{bmatrix}1 & 1\\ -1 & 1\end{bmatrix} = \begin{bmatrix}1 & 0\\ 0 & 3\end{bmatrix}$$

$$Q^T \begin{bmatrix} 2 & 1 \\ 1 & 2 \end{bmatrix} Q = \begin{bmatrix} 1 & -1 \\ 1 & 1 \end{bmatrix} \begin{bmatrix} 2 & 1 \\ 1 & 2 \end{bmatrix} \begin{bmatrix} 1 & 1 \\ -1 & 1 \end{bmatrix} = \begin{bmatrix} 2 & 0 \\ 0 & 6 \end{bmatrix}$$

$$Q^T \begin{bmatrix} -\frac{1}{2} f_a \omega - \frac{1}{2} f_s \omega \\ \frac{1}{2} f_s \omega \end{bmatrix} = \begin{bmatrix} 1 & -1 \\ 1 & 1 \end{bmatrix} \begin{bmatrix} -\frac{1}{2} f_a \omega - \frac{1}{2} f_s \omega \\ \frac{1}{2} f_s \omega \end{bmatrix} = \begin{bmatrix} -\frac{1}{2} f_a \omega - f_s \omega \\ -\frac{1}{2} f_a \omega \end{bmatrix}$$

Finally, we obtain the equilibrium solutions transformed in the modal basis:

$$\begin{bmatrix} -2+\alpha+\beta & \alpha-\beta \\ \alpha-\beta & 6+\alpha+\beta \end{bmatrix} \begin{bmatrix} m_B \\ m_S \end{bmatrix} + \omega \left\{ \lambda + m_B^2 + 3m_S^2 \right\} \begin{bmatrix} 2 & 0 \\ 0 & 6 \end{bmatrix} \begin{bmatrix} m_B \\ m_S \end{bmatrix} = \begin{bmatrix} -\frac{1}{2} f_a \omega - f_s \omega \\ -\frac{1}{2} f_a \omega \end{bmatrix} \quad \text{(B.10)}$$

The equilibrium equations in the modal basis have an interesting form, in that the non-linear part has reduced in complexity due to elimination of the cross term. However, this does not mean that the two equations are uncoupled; hence, the complexity has only been hidden in the new non-linear term $\lambda + m_B^2 + 3m_S^2$. Dissecting the FD characteristics has been attempted without success: it was not succeeded to obtain the same representation as in [79]. (B.10) can also be used to plot the FD characteristics with respect to the modal amplitudes. These FD characteristics are side views of the force in the modal amplitude space, similar to the mapped path in the potential energy surfaces in Figure B.2. No significant difference between the architectures that adds to an explanation was found in these results.

Appendix C
Buckled Stepped Beam and Parallel Guidance

This chapter serves as the first iteration to the experiments conducted in Chapter 5. Finite element analysis (FEA) as well as the prototyping of physical models is discussed. As in Chapter 5, the results obtained from finite element modeling and experiments are compared to establish the effect of matching buckling loads. Furthermore, matching of higher buckling loads is discussed.

C.1 Tuning the stiffness

C.1.1 Critical load ratio

The goal of this experiment is to investigate the effect of matching the first two buckling loads of a mechanism, as firstly introduced in the work of Kuppens e.a. [73]. In order to do this, recall the critical load ratio (CLR) [74]. The CLR describes the ratio between the first and second critical buckling loads. However, for further research, we can define this as the ratio between two chosen critical loads in general, which allows us to investigate the effect of matching other buckling loads. By increasing the CLR, the two corresponding buckling modes come closer together, as it were. Upon reaching unity (CLR = 1), the two buckling modes occur simultaneously. It is observed that by maximizing the CLR of the first two critical loads, the overall stiffness in the mechanism diminishes.

C.1.2 Mechanisms

To test the effect of the CLR on the stiffness in the mechanisms, two architectures are used. Here, both architectures and tuning of the FD characteristics is discussed.

Buckled Parallel Guidance

The Buckled Parallel Guidance (BPG) is used in [73], as it is "easy" to compensate the stiffness in this architecture. The ease of stiffness compensation is a result of the parallel guidance mechanism. The two parallel flexures prevent the rotation of the shuttle they suspend, and as a result, all the elastic elements connected to this shuttle are rendered connected in parallel. Elastic elements in parallel share the same applied displacement, which means that their FD characteristics can simply be added to one another with respect to the force. This advantageous property is exploited in static balancing, by adding positive and negative slopes in the FD characteristic to obtain a plateau [9], and hence a statically balanced mechanism. This is displayed in Figure C.1a, when adding the linear

FD curve (b) to a bistable FD curve (a), the resulting curve (a+b) contains a relatively flat section.

Buckled Stepped Beam

In the Buckled Stepped Beam (BSB), the flexures do not prevent the rotation of the shuttle, and as a result, it is not possible to simply add the FD characteristics to obtain a statically balanced mechanism. Alike behavior can be seen for elastic elements in series. In series, elastic elements share the same force, but the displacement is different. As a result, the FD characteristics have to be added with respect to the displacement. In Figure C.1b, it is seen that the resulting curve (a+b) shows entirely different behavior compared to the parent curves (a) and (b) and the resulting curve in parallel. This extreme example shows snap-back behavior that can be obtained in series architectures [9]. Strictly speaking, neither architecture is actually parallel nor series, but the parallel guidance exhibits the same behavior as elastic elements in parallel. In the interest of statically balancing orthoplanar mechanisms, the BSB is investigated, since this architecture is more straightforwardly applicable in orthoplanar mechanisms.

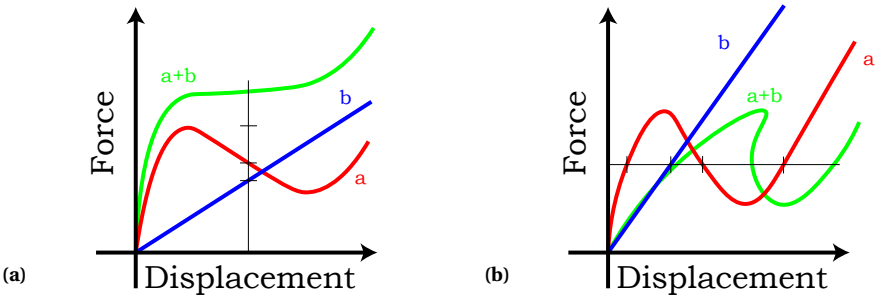

Figure C.1: Addition of force-deflection characteristics in (a) parallel and (b) series configurations. In parallel, elastic elements share the displacement and the FD characteristics are added with respect to displacement. In series, elastic elements share the force and the FD characteristics are added with respect to force, which in extreme cases may lead to snap-back

C.2 Designing

C.2.1 Mechanical design

The two used architectures consist of an unchanging flexure(s), a flexure variable in length and width, and a shuttle connecting both, as displayed in Figure C.2. In the BSB, a shuttle is suspended by an unchanging and variable flexure on either side. In the BPG, the unchanging part comprises a parallel guidance mechanism, consisting of a shuttle suspended by two flexures. The variable flexure is connected to the shuttle, creating a parallel connection. Both architectures are brought into post-buckling by applying an axial displacement d. The buckling loads are tuned by changing the geometry of the architecture. To this end, parameters β and σ are used, which represent the length and width of the variable flexure relative to the unchanging flexures respectively. Hence, by changing the values of β and σ, the ratio between the first two buckling loads is tuned. The parameters chosen for the models are given in Table C.1.

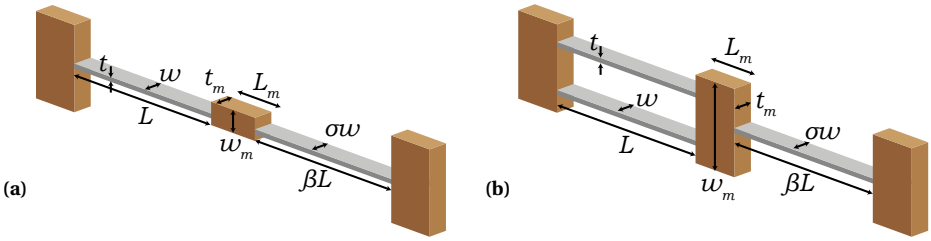

Figure C.2: Proposed mechanism BSB (a) and BPG (b) architectures. β and σ denote the relative length and width of the flexures respectively

C

Table C.1: Model parameters used for mechanical design of the BSB and BPG architectures

	BSB	BPG
Flexure length L [mm]	50	50
Flexure width w [mm]	5	5
Flexure thickness t [mm]	0.20	0.20
Shuttle length L_m [mm]	20	20
Shuttle width w_m [mm]	5	50
Shuttle thickness t_m [mm]	5	5
Pre-loading displacement d [mm]	5	5
β [-]	0.01 - 3	0.01 - 3
σ [-]	0.01 - 1	0.01 - 1

C.2.2 Forming the design space

To investigate the effect of the CLR on the FD characteristic, a design space containing different designs, i.e. different combinations of β and σ, is constructed. This design space is formed by performing a linear buckling analysis to obtain the buckling loads of both architectures for a set of β and σ. Both architectures are modeled in ANSYS Mechanical APDL to perform a linear buckling analysis and a simulation of the mechanical behavior, i.e. to obtain the force-deflection characteristic. The models are created using two-node Timoshenko beam elements (BEAM188) for both the flexures and the shuttle, which are modeled as linear elastic (flexures: $E = 190\,\text{GPa}$, $\nu = 0.34$, $\rho = 7890\,\text{kg}\cdot\text{m}^{-3}$; shuttle: $E = 3\,\text{GPa}$, $\nu = 0.35$, $\rho = 1180\,\text{kg}\cdot\text{m}^{-3}$). β and σ are both chosen to be sets of 40 ranging between the values in Table C.1. As a result, the buckling loads $P_{cr,i}$ for 1600 design iterations are obtained. The ratio between the first two buckling loads is determined for each design and displayed in Figures C.3b and C.3a, for the BSB and BPG respectively. Both design spaces are provided with five sample points which represent the chosen designs. These choices are based on the value of the CLR: the center Sample is the optimal design, i.e. that with the largest CLR. The surrounding points are chosen to investigate the influence of β and σ on the CLR, and ultimately the effect on the FD characteristics.

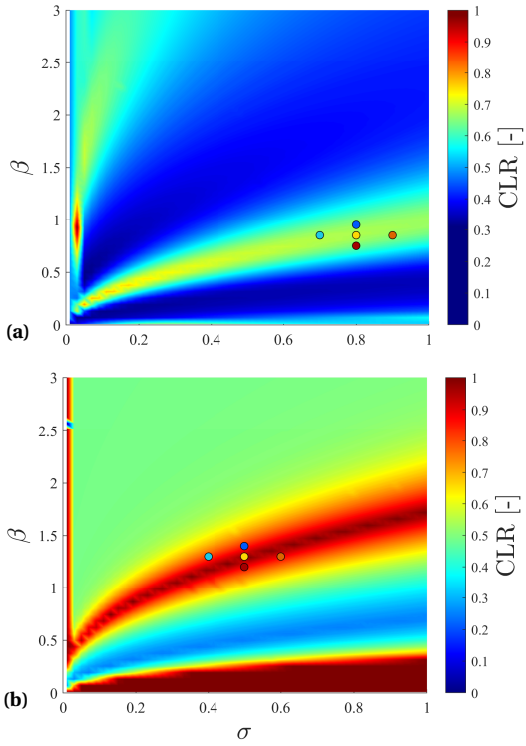

Sample point	β	σ	CLR
Center	0.85	0.8	0.6779
Right	0.85	0.9	0.6593
Left	0.85	0.7	0.6770
Above	0.95	0.8	0.6603
Below	0.75	0.8	0.6388

Sample point	β	σ	CLR
Center	1.3	0.5	0.9712
Right	1.3	0.6	0.8836
Left	1.3	0.4	0.8077
Above	1.4	0.5	0.8380
Below	1.2	0.5	0.8775

Figure C.3: Critical load ratio (CLR) surface plot to β and σ for the buckled stepped beam (a) and buckled parallel guidance (b) architectures. The sample points at the chosen optimum value for the CLR and the points around the Center are indicated. For the BSB, the surrounding points are offset with $\Delta\beta = 0.1$ and $\Delta\sigma = 0.1$. For the BPG architecture, the surrounding points are offset with $\Delta\beta = 0.1$ and $\Delta\sigma = 0.1$

C.2.3 Manufacturing

The sample points in Figure C.3 are manufactured in order to validate the mechanical behavior, by measuring the FD characteristics. The flexures, both the unchanging and variable, are manufactured from AISI301 stainless steel using a laser cutter. The flexures are given a 5 mm long and wide appendage on either side, for the clamping, as seen in Figure C.4. The shuttle, and auxiliary parts for the assemblies, are manufactured from PMMA using a laser cutter. Auxiliary parts comprise two boundary blocks, which act as the clamping for the flexures, and a base plate that is used to assemble the parts in a pre-loaded state. The shuttle and base blocks are provided with 5 mm deep slits, in which the flexures are embedded to create the clamped boundary. Additionally, the shuttle is provided with a hole in the middle, which is used for the connection between the FD measurement setup and the testing sample. The parameters from Table C.1 are used in the physical models as well. Figure C.5 displays the manufactured prototypes.

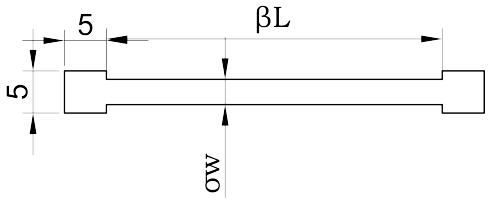

Figure C.4: Drawing of variable flexure. The square appendages at then ends are used for clamping of the flexures

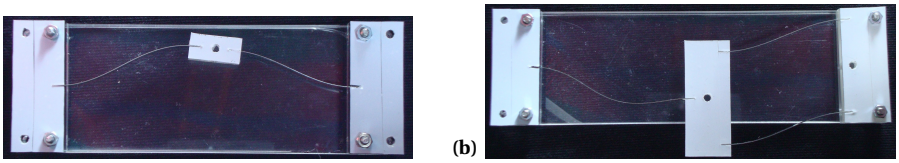

Figure C.5: Prototypes of BSB (a) and BPG (b) architectures. The base blocks and shuttle are indicated by the white faces. The shuttles are provided with hole in the middle that enables a connection to the FD measurement setup with a pulley and mass

Additional measurement point

An additional point for the BSB is chosen, namely at ($\beta = 0.9253; \sigma = 0.0302$). From Figure C.3a, it follows that a CLR ≈ 1 is obtained, possibly returning statically balanced behavior. This point is chosen to investigate whether it is possible to obtain the desired statically balanced behavior in the BSB Architecture. The width of the variable flexure reduces to 0.15 mm however, which is not manufacturable. Therefore, it is chosen to scale the width of the unchanging flexure up to $w = 67$ mm, giving a width of 2 mm for the variable flexure. A frame and shuttle are 3D printed from PLA and the flexures are cut from AISI301 stainless steel using guillotine shears. The resulting prototype is displayed in Figure C.6.

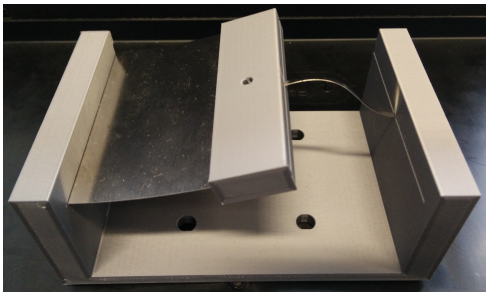

Figure C.6: Additional BSB measurement point ($\beta = 0.9253; \sigma = 0.0302$). Flexures are scaled up to make manufacturing possible

C.3 Force-deflection behavior

After the linear buckling analysis, the mechanical behavior is evaluated by performing an FD analysis of the finite element models; this is subsequently experimentally verified. The same setup as in Chapter 5 is used for the FD measurements. As in the previous measurements, a magnet is used to ensure the connection between the force sensor and the prototypes in the unstable region. The connection is displayed in Figure C.7.

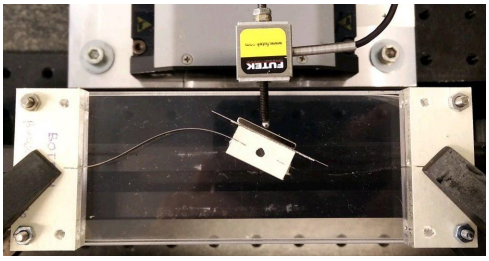

Figure C.7: Rolling contact magnet connection between force-sensor and prototypes. The magnet ensures contact in the unstable region

C.3.1 Sample point measurements

A comparison of the FEA and experimental FD results in the sample points are displayed in Figures C.9 and C.8 for the BSB and BPG Architectures respectively. It can be said that despite the discrepancies, the experimental results match the simulation results; therefore, the model is said to work correctly. In the BPG, the resulting FD characteristic of the Center sample shows a plateau close to zero force. This indicates that a CLR near unity results in a significantly low actuation force; hence, this ratio can be used to lower the actuation force in the BPG Architecture. As for the BSB Architecture, the chosen sample points show little difference in the CLR, which results in little difference between the obtained FD characteristics.

C.3.2 Additional point measurements

To check whether the effect of a unity CLR returns the same behavior in the BSB as in the BPG, the FD analysis is also performed on the additional sample point for the BSB Architecture. Due to the nearly square cross section of the variable flexure for an unchanging flexure width $w = 5\,\text{mm}$, the matched buckling loads are not the desired ones. In Figure C.10a, these two modes, which are in different planes, are displayed. Upon scaling the flexures up, the modes are the expected ones. The FD behavior is displayed in Figure C.10b; it clearly shows bistable behavior, which is not the expected effect for a unity CLR. The actual CLR for the upscaled flexures is 0.56, resulting in the bistable behavior.

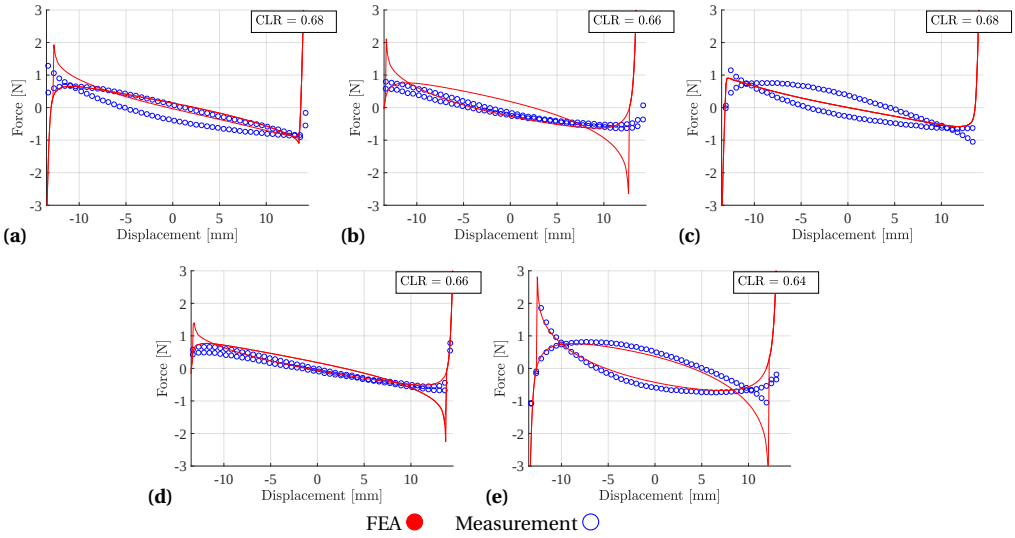

Figure C.8: Comparison of FEA and experimental FD behavior for BSB Architecture: (a) Center, (b) Left, (c) Right, (d) Above, (e) Below

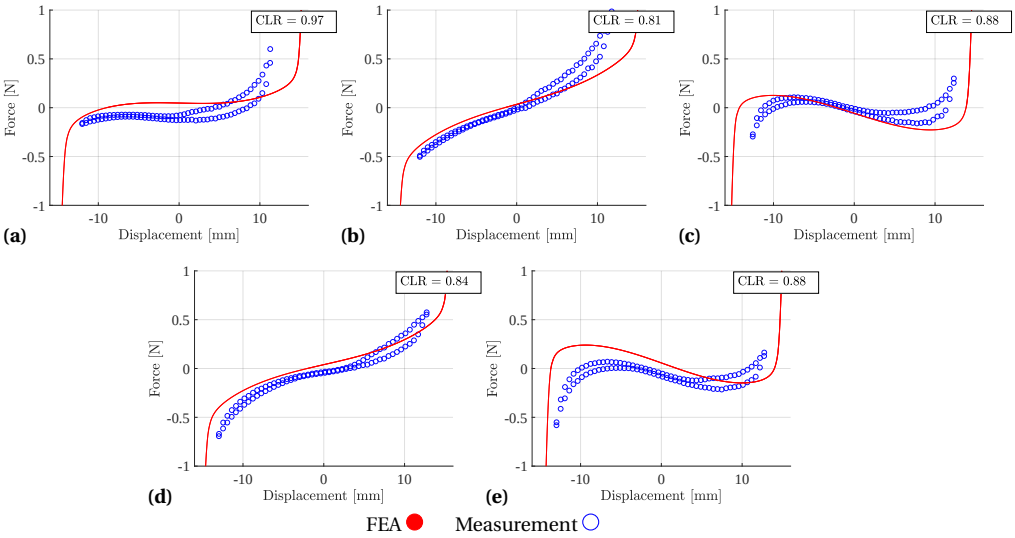

Figure C.9: Comparison of FEA and experimental FD behavior for BPG Architecture: (a) Center, (b) Left, (c) Right, (d) Above, (e) Below

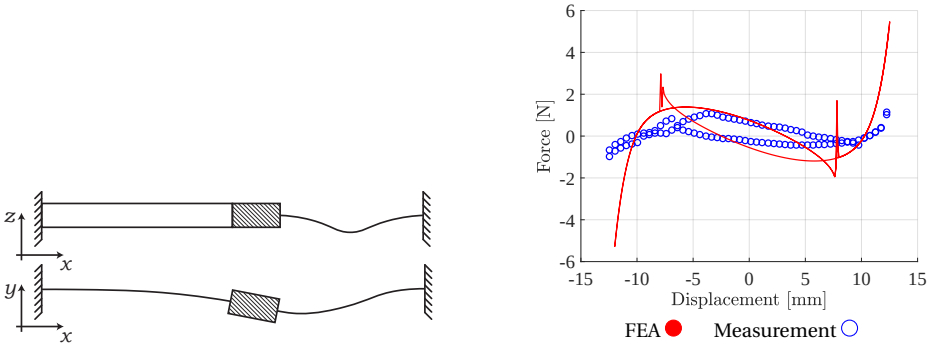

Figure C.10: Two modes in additional sample point (a): two modes in different planes. Due to the nearly square cross section, the two matching modes are in a different plane. Comparison of FEA and experimental FD behavior for additional sample in BSB Architecture (b)

C.4 Influence of other modes

Following the work of Kuppens e.a. [73], the two buckling loads of the displayed modes in Figure C.11 have been matched and having them equal shows a flat FD characteristic near zero. During transverse deflection in post-buckling, both architectures transition between the two buckling modes displayed. Thus, the reasoning follows: if it is easy to transition between the two buckling modes, the potential barrier will be low.

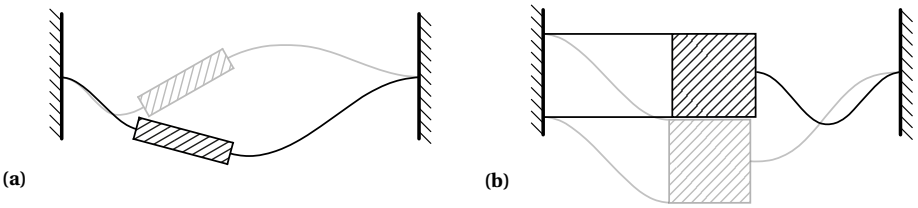

Figure C.11: The first two buckling modes of which the buckling loads are matched for BSB and BPG architectures

Hence arises the questions, why those two modes are chosen in particular, and what FD behavior might be expected when taking into account matching of different modes. The displacement field can be expressed in terms of the buckling modes as in Chapter B.2.1. This gives us an insight in the presence of the modes, and hence which modes contribute to the FD characteristic of the design. To this end, three designs of the BSB and BPG have been investigated, where the CLR between other modes than the first two was maximized. The FD characteristics of these three designs are displayed in Figure C.12; the CLR values between different modes are tabulated in Table C.2; and the first four buckling modes and their participation in the displacement field during deflection are depicted in Figures C.13 and C.14 for the BSB and BPG respectively. The modes are indicated by the different colors and linked to the corresponding participation curve.

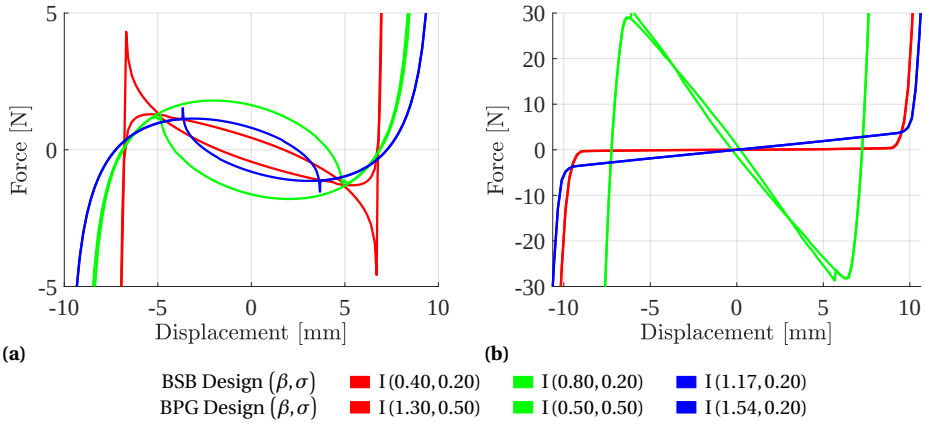

Figure C.12: Force-deflection characteristics of the three chosen BSB (a) and BPG (b) designs

Table C.2: Critical Load Ratio values between the four buckling modes in the three BSB and BPG designs

	BSB			BPG		
Design	I	II	III	I	II	III
$CLR_{1,2}$	0.77	0.35	0.36	0.97	0.25	0.50
$CLR_{1,3}$	0.26	0.27	0.17	0.45	0.24	0.26
$CLR_{1,4}$	0.22	0.13	0.15	0.24	0.24	0.24
$CLR_{2,3}$	0.34	0.76	0.49	0.46	0.95	0.51
$CLR_{2,4}$	0.28	0.38	0.41	0.25	0.95	0.47
$CLR_{3,4}$	0.82	0.50	0.83	0.53	1	0.93

C.4.1 Buckled Stepped Beam

As can be observed, BSB Design I, which is identical to BSB Design I in Chapter 5, returns the smallest distance between the two load paths. In this design, the $CLR_{1,2}$ is maximized to reduce the distance between the load paths. When looking into the mode participation for Design I, it is observed that the displacement field is fully described by the first and second mode. Despite $CLR_{3,4} > CLR_{1,2}$, the third and fourth mode do not occur. As a result, energy is only used for deformation between modes 1 and 2, reducing the distance between the load paths.

For Design II, the $CLR_{2,3}$ is maximized which can be observed through the modal participation. While the displacement field is mainly described by modes 1 and 2, mode 3 significantly contributes. The presence of mode 3 in the displacement field causes energy to be used for the corresponding deformation; hence, the distance between the load paths increases significantly. However, despite the increase distance between the load paths (and therefore also the limit load of snap-through) the sharp peaks at the ends of the FD characteristic disappear. The mode participation indicates a sharp rise in contribution of mode 3 at this part of the FD characteristic. Hence, it is thought that the contribution of higher modes results in a more gradual transition between the equilibria.

For Design III, the $CLR_{3,4}$ is maximized; however, mode 4 does not contribute to the displacement field. As the $CLR_{1,2}$ is low, it would be expected to observe a large distance between the load paths. Interestingly, this distance is quite comparable to that of Design

I. A slight increase is caused by the presence of the third mode. The same sharp increase in the contribution of mode 3 as in Design II is observed, which decreases the peaks in the FD characteristic.

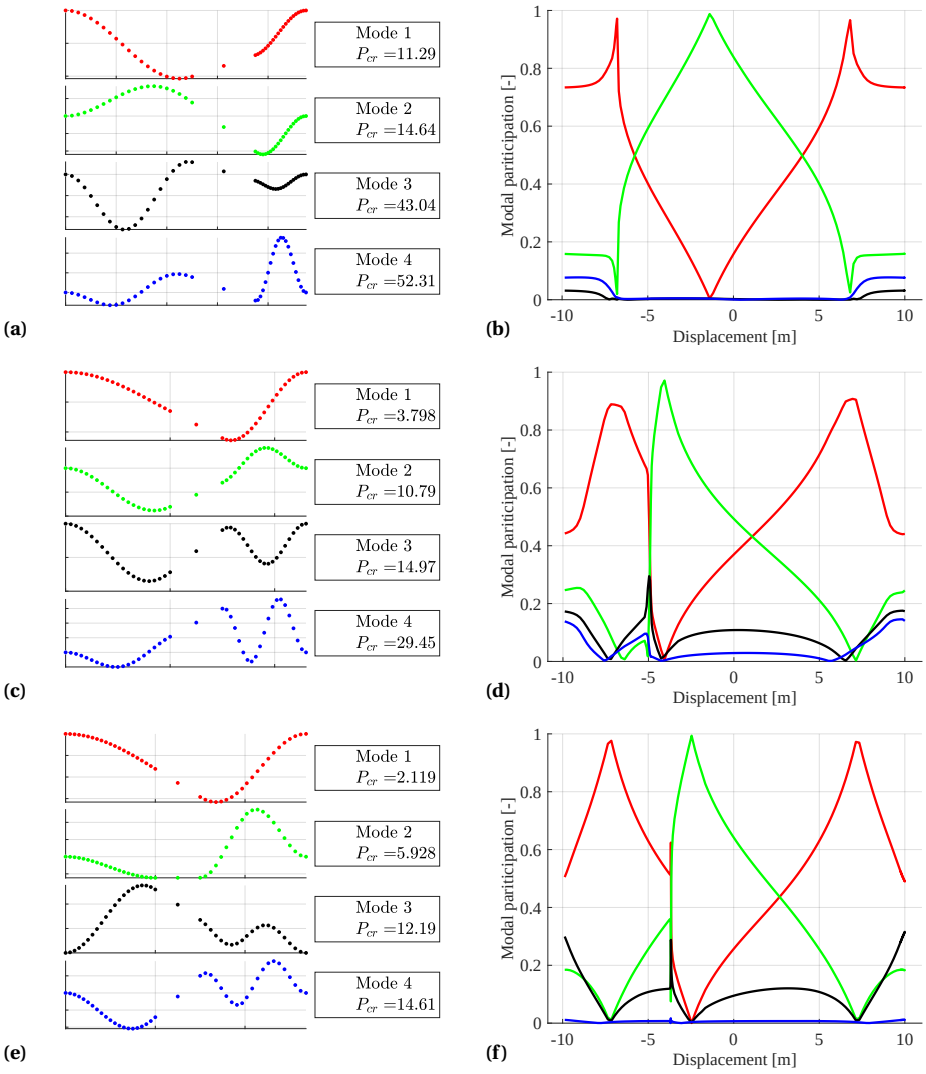

Figure C.13: Depiction of first four buckling modes (a, c, e) and mode participations (b, d, f) for BSB for three designs: Design I (a,b), Design II (c,d), Design III (e,f)

C.4.2 Buckled Parallel Guidance

BPG Design I is identical to BPG Design I in Chapter 5. It is observed that the $CLR_{1,2}$ is near unity, which, given the two corresponding modes, returns a low linear stiffness or near static balancing. Due to the scale of the vertical axis, this FD characteristic looks entirely flat; however, the behavior returns slight positive stiffness. The CLR values for any other combination of modes is low; this is also observable in the modal participation (Figure C.14b), since the displacement field can fully be described by the first two modes. Other modes have no participation, which can be interpreted as no energy going into deformation corresponding to those modes.

For Design II, the FD characteristic drastically changes, giving a steep negative stiffness between the nonlinear ends. Compared to Design I, the $CLR_{1,2}$ is significantly lower, while a $CLR_{2,3}$ and $CLR_{2,4}$ near unity are obtained. The effect of these two CLR values is seen in the modal participation in C.14d: modes 3 and 4 both show a significant contribution in the the displacement. Looking into the corresponding modes, it is observed that these two modes do not aid the transverse deflection of the BPG. Hence, it can be said significant effort is put into deflection of the two parallel flexures, resulting in an increase in actuation force during deflection. This deflection of the parallel flexures is enabled by the unity CLRs for between mode 2 and modes 3 and 4.

Finally for Design III, an FD similar to that of Design I is obtained, though with a significant increase in stiffness. In this design a $CLR_{1,2} = 0.50$ is obtained, while a near unity $CLR_{3,4}$ is obtained; however, mode 4 does interestingly not contribute to the displacement field. The FD behavior is similar to that found in Chapter 5 for designs where $CLR_{1,2}$ declines.

A final observation is the presence of the modes in the equilibrium positions. For Designs I and III, it is observed that at 0mm displacement, the displacement field is entirely described by the first mode. In Design II, which has two stable equilibrium positions at either side of the motion range, the displacement field is entire described by the first mode as well. Hence, at a stable equilibrium it is expected to have a mechanism configuration in purely the first mode. This is of course an obvious thought when related to pre-loading. Upon pre-loading, we are putting energy into the system and essentially pushing it away from its stable equilibrium (or minimum of potential energy). Once buckling occurs, a new minimum of potential energy is formed, which corresponds to the first buckling mode.

C.4.3 Recommendation

Based on these findings, a recommendation for stiffness compensation can be formed. It is required to match the buckling loads that correspond to the stable equilibrium, i.e. the first buckling mode, and a mode that describes the displacement field of interest. "Of interest" should not be confused with the modes that describe the displacement field in terms of modal participation. From BPG Design II, it is observed that even though modes 3 and 4 describe the displacement field, they do not aid in the desired displacement; hence, the energy required for deformation is large and the FD characteristic returns a steep negative stiffness. When comparing BPG Designs I and III, it would seem that matching modes 1 and 3 for Design III would return a flat FD characteristic. However, by matching the first and third mode, the second mode must per definition also match the

first and third mode. Moreover, a slight change in geometry already returns a significant difference in the order (and also shape) of the modes. As a result, what was formerly known as mode 3 may change in this process of matching the loads.

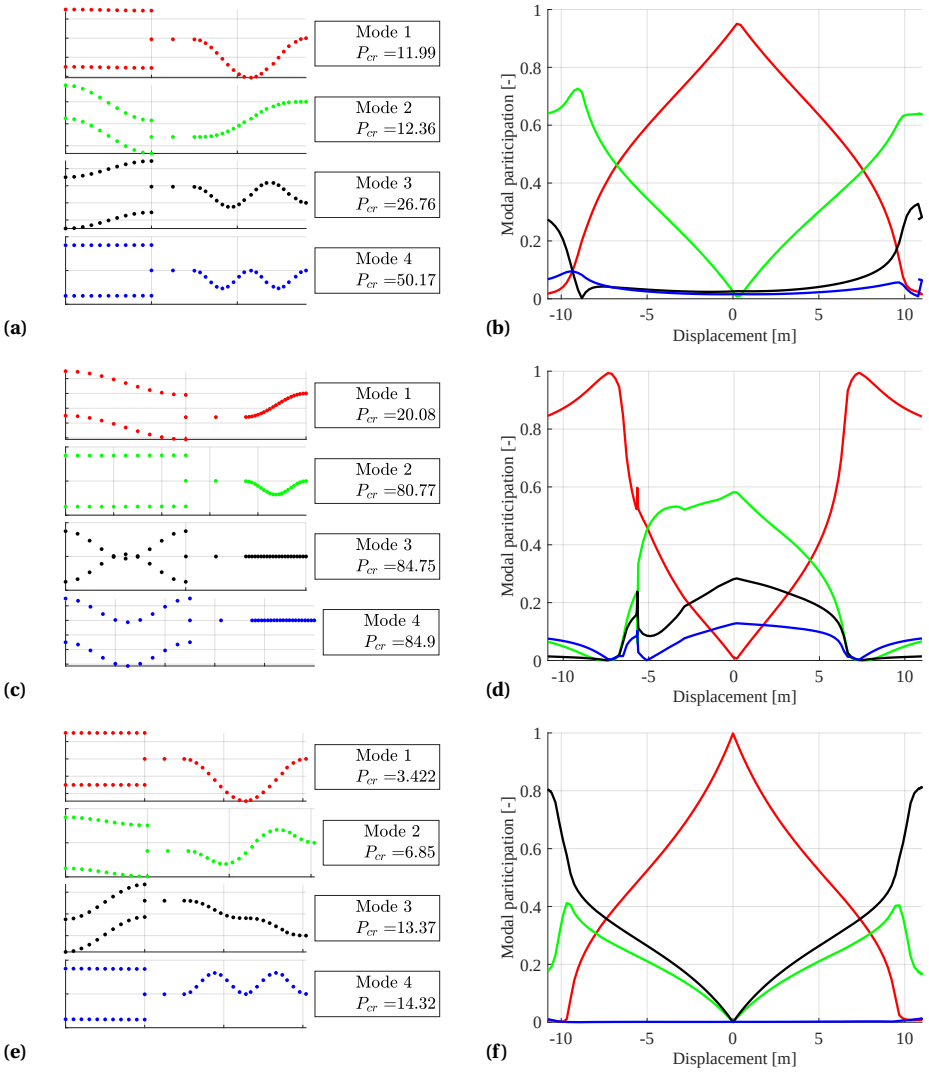

Figure C.14: Depiction of first four buckling modes (a, c, e) and mode participations (b, d, f) for BPG for three designs: Design I (a,b), Design II (c,d), Design III (e,f)

Appendix D
Technical drawings of the lumped-compliant four-bar mechanism

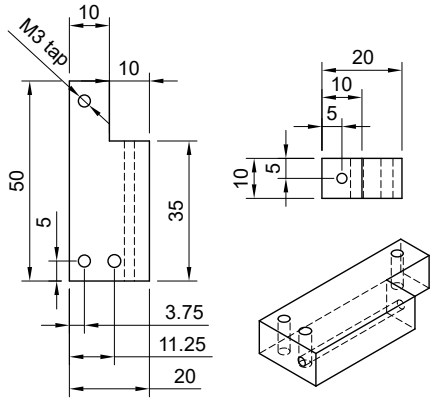

Figure D.1: Technical drawing and dimensions of clamping block for outer flexures

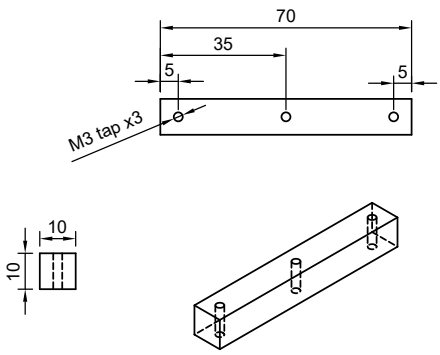

Figure D.2: Technical drawing and dimensions of rigid links

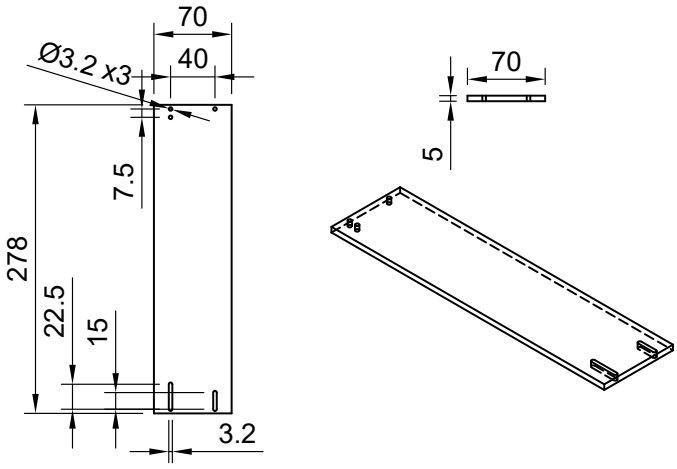

Figure D.3: Technical drawing and dimensions of baseplate on which the mechanism is mounted

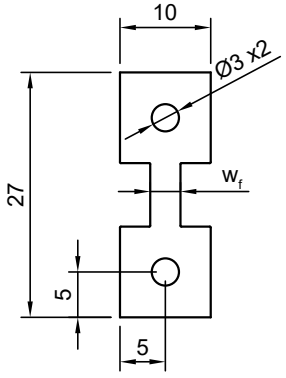

Figure D.4: Technical drawing and dimensions of flexure with variable width w_f to change the flexural rigidity

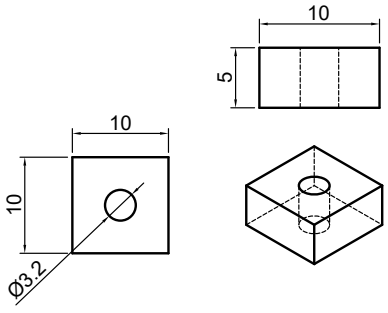

Figure D.5: Technical drawing and dimensions of clamping PMMA cap

Appendix E
Technical drawings of buckled stepped beam and parallel guidance frame

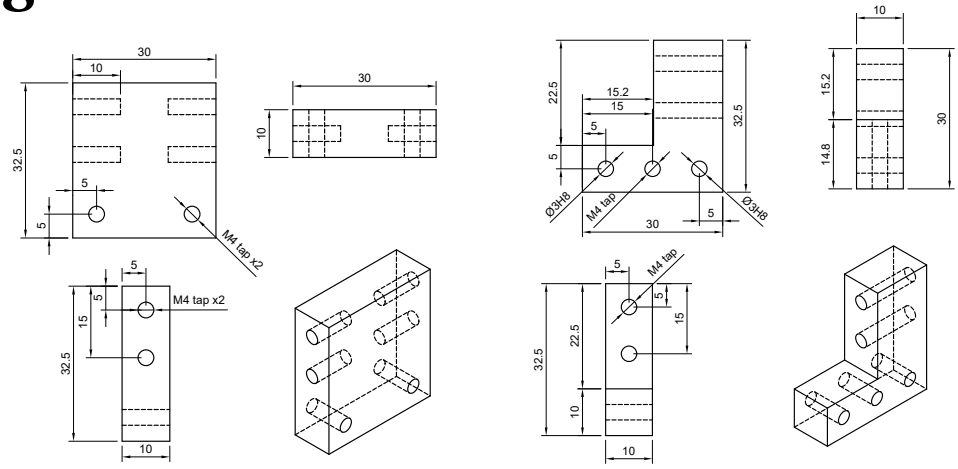

(a) **(b)**

Figure E.1: Technical drawings and dimensions of sides for constant (a) and variable (b) flexure clampings

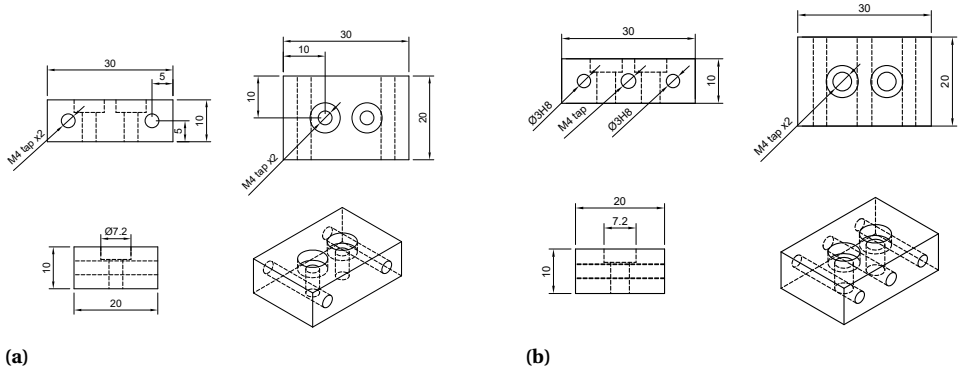

(a) **(b)**

Figure E.2: Technical drawings and dimensions of bottom blocks for attachment to base plate for constant (a) and variable (b) flexure sides

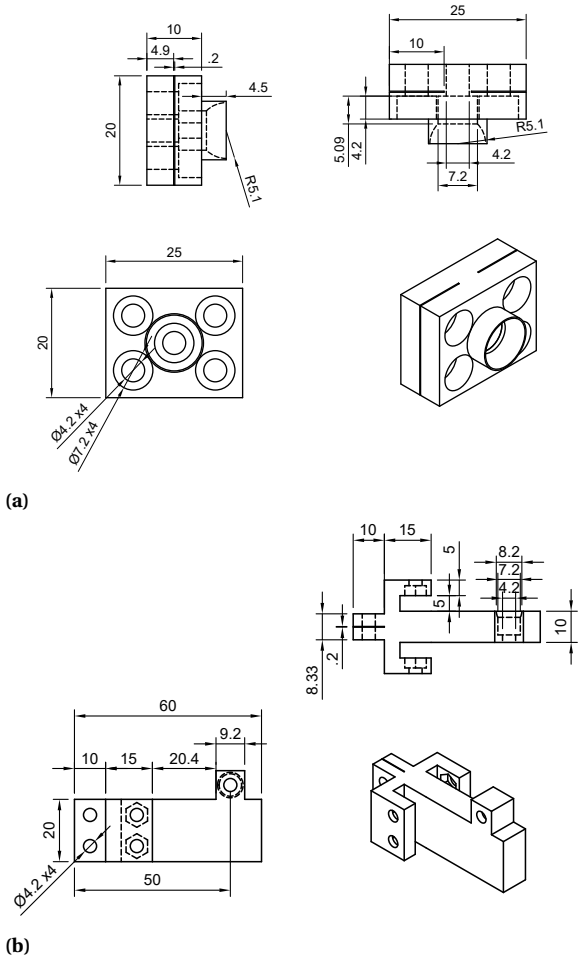

Figure E.3: Technical drawings and dimensions of shuttles for buckled stepped beam (a) and buckled parallel guidance (b)

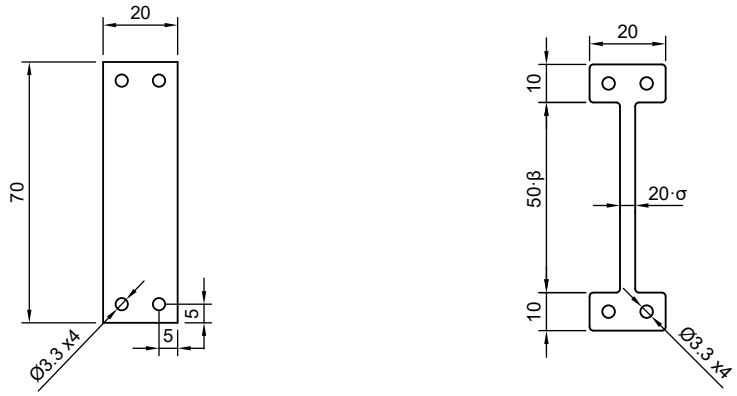

(a) **(b)**

Figure E.4: Technical drawings and dimensions of constant (a) and variable (b) flexures

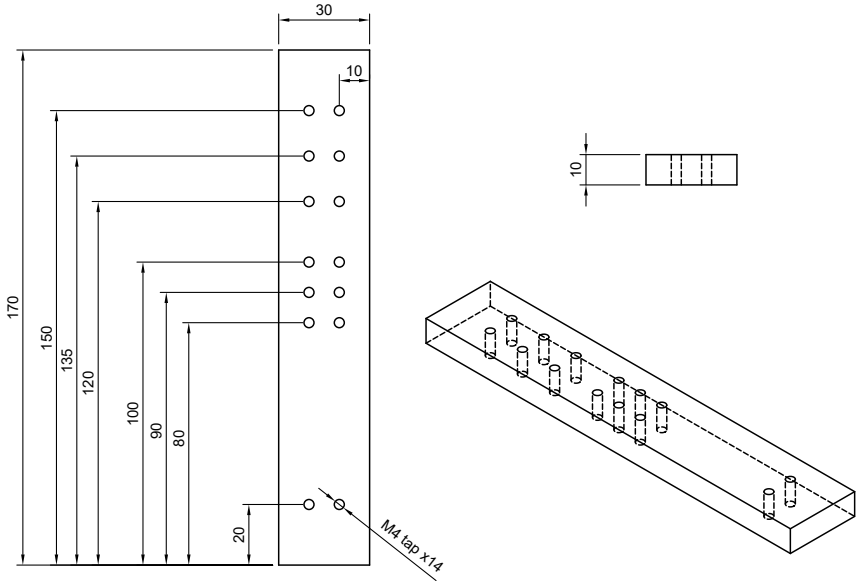

Figure E.5: Technical drawings and dimensions of base plate used to clamp all parts and enable transitioning between measurement designs

Bibliography

[1] *Wireless automation as an enabler for the next industrial revolution,* .

[2] eurostat, *Waste statistics -recycling of batteries andaccumulators,* .

[3] K. Singh and S. Moh, *A comparative survey of energy harvesting techniques for wireless sensor networks,* pp. 28–33.

[4] S. Roundy, D. Steingart, L. Frechette, P. Wright, and J. Rabaey, *Power sources for wireless sensor networks,* , 17 ().

[5] S. Roundy, P. K. Wright, and J. M. Rabaey, *Energy Scavenging for Wireless Sensor Networks: with Special Focus on Vibrations* (Springer US).

[6] S. Roundy, P. K. Wright, and J. Rabaey, *A study of low level vibrations as a power source for wireless sensor nodes,* **26**, 1131 ().

[7] Y. Jia, *Review of nonlinear vibration energy harvesting: Duffing, bistability, parametric, stochastic and others,* , 1045389X2090598.

[8] J. L. Herder, *Energy-free systems; theory, conception and design of statically balanced spring mechanisms,* (), publisher: Unpublished.

[9] G. Radaelli, *Synthesis of mechanisms with prescribed elastic load-displacement characteristics*, OCLC: 7792822149.

[10] Y.-Y. Chen, D. Vasic, Y.-P. Liu, and F. Costa, *Comparison of bistable magnetic nonlinear piezoelectric energy harvester with traditional linear technique,* in *IECON 2012 - 38th Annual Conference on IEEE Industrial Electronics Society*, pp. 949–954.

[11] M. F. Daqaq, R. Masana, A. Erturk, and D. Dane Quinn, *On the role of nonlinearities in vibratory energy harvesting: A critical review and discussion,* **66**, 040801.

[12] R. L. Harne and K.-W. Wang, *Harnessing Bistable Structural Dynamics: For Vibration Control, Energy Harvesting and Sensing*, 1st ed. (Wiley & Sons).

[13] S. P. Pellegrini, N. Tolou, M. Schenk, and J. L. Herder, *Bistable vibration energy harvesters: A review,* **24**, 1303.

[14] N. Tran, M. H. Ghayesh, and M. Arjomandi, *Ambient vibration energy harvesters: A review on nonlinear techniques for performance enhancement,* **127**, 162.

[15] S. P. Beeby, L. Wang, D. Zhu, A. S. Weddell, G. V. Merrett, B. Stark, G. Szarka, and B. M. Al-Hashimi, *A comparison of power output from linear and nonlinear kinetic energy harvesters using real vibration data,* **22**, 075022.

[16] R. Masana and M. F. Daqaq, *Comparing the performance of a nonlinear energy harvester in mono- and bi-stable potentials*, in *Volume 1: 23rd Biennial Conference on Mechanical Vibration and Noise, Parts A and B* (ASMEDC) pp. 255–264.

[17] R. L. Harne and K. W. Wang, *A review of the recent research on vibration energy harvesting via bistable systems*, **22**, 023001 ().

[18] P. Holmes, *A nonlinear oscillator with a strange attractor*, **292**, 419.

[19] W. Szemplińska-Stupnicka, *The analytical predictive criteria for chaos and escape in nonlinear oscillators: A survey*, **7**, 129.

[20] A. F. Arrieta, P. Hagedorn, A. Erturk, and D. J. Inman, *A piezoelectric bistable plate for nonlinear broadband energy harvesting*, **97**, 104102.

[21] D. Pan, W. Jiang, and F. Dai, *Dynamic analysis of bi-stable hybrid symmetric laminate*, **225**, 111158.

[22] A. Syta, C. R. Bowen, H. A. Kim, A. Rysak, and G. Litak, *Responses of bistable piezoelectric-composite energy harvester by means of recurrences*, **76-77**, 823 ().

[23] D. N. Betts, C. R. Bowen, H. A. Kim, N. Gathercole, C. T. Clarke, and D. J. Inman, *Investigation of bistable piezo-composite plates for broadband energy harvesting*, p. 86881N.

[24] I. Kovacic and M. J. Brennan, *The Duffing Equation: Nonlinear Oscillators and Their Behaviour* (John Wiley & Sons Ltd).

[25] K. Guo, S. Cao, and S. Wang, *Numerical and experimental studies on nonlinear dynamics and performance of a bistable piezoelectric cantilever generator*, **2015**, 1.

[26] M. Heymanns and P. Hagedorn, *Analytical and numerical investigations on a bistable system for energy harvesting application*, in *Volume 6: 10th International Conference on Multibody Systems, Nonlinear Dynamics, and Control* (American Society of Mechanical Engineers) p. V006T10A063.

[27] M. Heymanns, P. Hagedorn, and B. Schweizer, *Multistable structures for broad brandwidth vibration-based energy harvesters: An analytical design investigation*, Forschungsbericht / Mechanik, Technische Universität Darmstadt No. Band 39 (Studienbereich Mechanik, Technische Universität Darmstadt).

[28] D. Briand, E. Yeatman, and S. Roundy, *Micro Energy Harvesting*, 1st ed., Advanced MIcro & Nanosystems (Wiley-VCH).

[29] M. Panyam, M. F. Daqaq, and S. A. Emam, *Exploiting the subharmonic parametric resonances of a buckled beam for vibratory energy harvesting*, **53**, 3545.

[30] K. Yang, F. Fei, and H. An, *Investigation of coupled lever-bistable nonlinear energy harvesters for enhancement of inter-well dynamic response*, **96**, 2369.

[31] A. J. Lee and D. J. Inman, *Broadband energy harvesting performance of a piezoelectrically generated bistable laminate,* in *Sensors and Instrumentation, Aircraft/Aerospace and Energy Harvesting , Volume 8*, edited by E. Wee Sit, C. Walber, P. Walter, A. Wicks, and S. Seidlitz (Springer International Publishing) pp. 1–14.

[32] P. Harris, C. R. Bowen, H. A. Kim, and G. Litak, *Dynamics of a vibrational energy harvester with a bistable beam: voltage response identification by multiscale entropy and "0-1" test,* **131**, 109 ().

[33] P. Grassberger, T. Schreiber, and C. Schaffrath, *Nonlinear time sequence analysis,* **1**, 521.

[34] H. D. I. Abarbanel, R. Brown, J. J. Sidorowich, and L. S. Tsimring, *The analysis of observed chaotic data in physical systems,* **65**, 1331.

[35] H. D. I. Abarbanel, *Analysis of observed chaotic data*, Springer study edition (Springer).

[36] A. Wolf, J. B. Swift, H. L. Swinney, and J. A. Vastano, *Determining lyapunov exponents from a time series,* **16**, 285.

[37] M. T. Rosenstein, J. J. Collins, and C. J. De Luca, *A practical method for calculating largest lyapunov exponents from small data sets,* **65**, 117.

[38] J. Awrejcewicz, A. Krysko, N. Erofeev, V. Dobriyan, M. Barulina, and V. Krysko, *Quantifying chaos by various computational methods. part 1: Simple systems,* **20**, 175.

[39] G. A. Gottwald and I. Melbourne, *The 0-1 test for chaos: A review,* in *Chaos Detection and Predictability*, Vol. 915, edited by C. Skokos, G. A. Gottwald, and J. Laskar (Springer Berlin Heidelberg) pp. 221–247.

[40] A. Syta, C. R. Bowen, H. A. Kim, A. Rysak, and G. Litak, *Experimental analysis of the dynamical response of energy harvesting devices based on bistable laminated plates,* **50**, 1961 ().

[41] D. Toker, F. T. Sommer, and M. D'Esposito, *A simple method for detecting chaos in nature,* **3**, 11.

[42] A. M. Fraser and H. L. Swinney, *Independent coordinates for strange attractors from mutual information,* **33**, 1134.

[43] S. Wallot and D. Mønster, *Calculation of average mutual information (AMI) and false-nearest neighbors (FNN) for the estimation of embedding parameters of multidimensional time series in matlab,* **9**, 1679.

[44] P. D. Mitcheson, E. M. Yeatman, G. K. Rao, A. S. Holmes, and T. C. Green, *Energy harvesting from human and machine motion for wireless electronic devices,* **96**, 1457, conference Name: Proceedings of the IEEE.

[45] G. Litak, M. I. Friswell, and S. Adhikari, *Regular and chaotic vibration in a piezoelectric energy harvester,* **51**, 1017.

[46] K. Nakano, M. P. Cartmell, H. Hu, and R. Zheng, *Feasibility of energy harvesting using stochastic resonance caused by axial periodic force,* **60**, 314.

[47] J. J. Radice, P. J. Ellsworth, M. A. Romano, N. Lazarus, and S. S. Bedair, *On the use of discontinuous nonlinear bistable dynamics to increase the responsiveness of energy harvesting devices,* **84**, 49.

[48] P. Harris, M. Arafa, G. Litak, C. R. Bowen, and J. Iwaniec, *Output response identification in a multistable system for piezoelectric energy harvesting,* **90**, 20 ().

[49] P. Harris, G. Litak, J. Iwaniec, and C. R. Bowen, *Recurrence plot and recurrence quantification of the dynamic properties of cross-shaped laminated energy harvester,* **849**, 95 ().

[50] A. Syta, G. Litak, M. I. Friswell, and S. Adhikari, *Multiple solutions and corresponding power output of a nonlinear bistable piezoelectric energy harvester,* **89**, 99 ().

[51] Z. Wu, R. L. Harne, and K. W. Wang, *Excitation-induced stability in a bistable duffing oscillator: Analysis and experiments,* **10**, 011016.

[52] N. A. Alfutov, *Stability of Elastic Structures*, Foundations of Engineering Mechanics (Springer Berlin Heidelberg).

[53] M. L. Gambhir, *Stability Analysis and Design of Structures* (Springer Berlin Heidelberg).

[54] S. P. Timoshenko, J. M. Gere, and W. Prager, *Theory of elastic stability, second edition,* **29**, 220.

[55] C. M. Wang, C. Y. Wang, and J. Reddy, *Exact Solutions for Buckling of Structural Members*, COMPUTATIONAL MECHANICS and APPLIED ANALYSIS (CRC Press).

[56] B. Budiansky, *Theory of buckling and post-buckling behavior of elastic structures,* (Elsevier) pp. 1 – 65, ISSN: 0065-2156.

[57] J. He and Z.-F. Fu, *Overview of modal analysis,* in *Modal analysis* (Butterworth-Heinemann) pp. 1–11.

[58] J. Cai and C. D. Moen, *Automated buckling mode identification of thin-walled structures from 3d finite element mode shapes or point clouds,* p. 18.

[59] G. Chen and S. Zhang, *Fully-compliant statically-balanced mechanisms without prestressing assembly: concepts and case studies,* , 6.

[60] J. L. Herder, *Design of spring force compensation systems,* **33**, 151 ().

[61] S. R. Deepak and G. K. Ananthasuresh, *Static balancing of a four-bar linkage and its cognates,* , 19 ().

[62] S. R. Deepak and G. K. Ananthasuresh, *Perfect static balance of linkages by addition of springs but not auxiliary bodies,* **4**, 021014 ().

[63] B. Soethoudt and J. L. Herder, *Synthesis of perfect spring balancers with higher-order zero-free-length springs,* in *Volume 8: 31st Mechanisms and Robotics Conference, Parts A and B* (ASMEDC) pp. 751–762.

[64] J. A. Gallego and J. L. Herder, *Criteria for the static balancing of compliant mechanisms,* in *Volume 2: 34th Annual Mechanisms and Robotics Conference, Parts A and B* (ASMEDC) pp. 465–473.

[65] N. Tolou and J. L. Herder, *Concept and modeling of a statically balanced compliant laparoscopic grasper,* in *Volume 7: 33rd Mechanisms and Robotics Conference, Parts A and B* (ASMEDC) pp. 163–170.

[66] A. Lamers, J. A. Gallego Sánchez, and J. L. Herder, *Design of a statically balanced fully compliant grasper,* **92**, 230.

[67] E. G. Merriam, M. Colton, S. Magleby, and L. L. Howell, *The design of a fully compliant statically balanced mechanism,* in *Volume 6A: 37th Mechanisms and Robotics Conference* (American Society of Mechanical Engineers) p. V06AT07A035.

[68] N. Tolou, V. A. Henneken, and J. L. Herder, *Statically balanced compliant micro mechanisms (SB-MEMS): Concepts and simulation,* in *Volume 2: 34th Annual Mechanisms and Robotics Conference, Parts A and B* (ASMEDC) pp. 447–454.

[69] N. Tolou, P. Estevez, and J. L. Herder, *Collinear-type statically balanced compliant micro mechanism (SB-CMM): Experimental comparison between pre-curved and straight beams,* in *Volume 6: 35th Mechanisms and Robotics Conference, Parts A and B* (ASMEDC) pp. 113–117.

[70] K. A. Tolman, E. G. Merriam, and L. L. Howell, *Compliant constant-force linear-motion mechanism,* **106**, 68.

[71] J. A. Gallego Sánchez, *Buckling as a new perspective on static balancing of mechanisms,* , 8.

[72] F. M. Morsch and J. L. Herder, *Design of a generic zero stiffness compliant joint,* in *Volume 2: 34th Annual Mechanisms and Robotics Conference, Parts A and B* (ASMEDC) pp. 427–435.

[73] P. R. Kuppens, J. L. Herder, and N. Tolou, *Permanent stiffness reduction by thermal oxidation of silicon,* **28**, 900.

[74] T. Blad, R. Van Ostayen, and N. Tolou, *A method for tuning the stiffness of building blocks for statically balanced compliant ortho-planar mechanisms,* , 11.

[75] E. J. Barbero, E. K. Dede, and S. Jones, *Experimental verifcation of buckling-mode interaction in intermediate-length composite columns,* , 16.

[76] C. Lusk, *Using pseudo-rigid body models,* in *Handbook of compliant mechanisms*, Vol. 5, edited by L. L. Howell, S. P. Magleby, and B. M. Olsen (John Wiley & Sons, Inc) pp. 55–76.

[77] C. Schranz, B. Krenn, and H. A. Mang, *Conversion from imperfection-sensitive into imperfection-insensitive elastic structures. II: Numerical investigation,* **195**, 1458.

[78] T. Tarnai, *Zero stiffness elastic structures,* **45**, 425.

[79] P. Cazottes, A. Fernandes, J. Pouget, and M. Hafez, *Bistable buckled beam: Modeling of actuating force and experimental validations,* **131**, 101001.

[80] B. Camescasse, A. Fernandes, and J. Pouget, *Bistable buckled beam and force actuation: Experimental validations,* **51**, 1750.

[81] L. L. Howell, *Introduction to compliant mechanisms,* in *Handbook of compliant mechanisms*, Vol. 1, edited by L. L. Howell, S. P. Magleby, and B. M. Olsen (John Wiley & Sons, Inc) pp. 1–13.

[82] L. Berntsen, D. H. Gosenshuis, and J. L. Herder, *Design of a compliant monolithic internally statically balanced four-bar mechanism,* in *Volume 5A: 38th Mechanisms and Robotics Conference* (American Society of Mechanical Engineers) p. V05AT08A040.

[83] L. C. Leishman, D. J. Ricks, and M. B. Colton, *Design and evaluation of statically balanced compliant mechanisms for haptic interfaces,* in *ASME 2010 Dynamic Systems and Control Conference, Volume 1* (ASMEDC) pp. 859–866.

[84] P. J. Pluimers, N. Tolou, B. D. Jensen, L. L. Howell, and J. L. Herder, *A compliant on/off connection mechanism for preloading statically balanced compliant mechanisms,* in *Volume 4: 36th Mechanisms and Robotics Conference, Parts A and B* (American Society of Mechanical Engineers) pp. 373–377.

[85] J. Lassooij, N. Tolou, G. Tortora, S. Caccavaro, A. Menciassi, and J. L. Herder, *A statically balanced and bi-stable compliant end effector combined with a laparoscopic 2dof robotic arm,* **3**, 85.

[86] K. Hoetmer, J. L. Herder, and C. J. Kim, *A building block approach for the design of statically balanced compliant mechanisms,* in *Volume 7: 33rd Mechanisms and Robotics Conference, Parts A and B* (ASMEDC) pp. 313–323.

[87] A. H. Nayfeh and S. A. Emam, *Exact solution and stability of postbuckling configurations of beams,* **54**, 395.

[88] D. Brouwer, J. Meijaard, and J. Jonker, *Large deflection stiffness analysis of parallel prismatic leaf-spring flexures,* **37**, 505.

[89] R. Zheng, K. Nakano, H. Hu, D. Su, and M. P. Cartmell, *An application of stochastic resonance for energy harvesting in a bistable vibrating system,* **333**, 2568, read.